学位申請論文

Investigation of an enigmatic hump around 30 keV in Suzaku spectra of Aquila X-1 in the Hard State

(Aquila X-1「すざく」スペクトルのハード状態における
30 keV 付近の未解明なハンプ構造の調査)

2019年3月

窪田 恵

Abstract

To study nucleosynthesis, we performed a spectral analysis on a typical Neutron Star Low Mass X-ray Binary (NS-LMXB), Aquila X-1 (Aql X-1). In this system, the accreting matters from a companion mainly consist of hydrogen; thus, the surface of the neutron star is expected to be a proton-rich environment. Therefore, the neutron star's surface can be considered as a promising location of the rapid proton capture process (rp-process). This process is triggered by an unstable thermonuclear flash on the neutron star (Type-I burst) and involves a nucleosynthesis beyond the iron group.

Aquila X-1 was observed with *Suzaku* several times in the decay phase of an outburst in 2007 September-October. Among them, the second to fourth observations were performed 10 to 20 days after the burst peak, when the source was in the hard state with a luminosity of 2×10^{36} erg cm^{-2} s^{-1}. In general, the hard state spectrum can be represented by a hard X-ray continuum up to $\sim$100 keV arising when blackbody photons from the neutron star surface, plus an optically thick disk emission appering below a few keV. However, these spectra of 2nd to 4th observations have excess feature around 30 keV above the Comptonized continuum. We attempt to interpret this feature in the contest of the K-shell feature of heavy elements created via the rp-process.

We fitted the individual spectra with the canonical emission model of NS-LMXBs and found the these spectra exhibit a mutually consistent hump structure around 30 keV. Then we merged these three data to reduce the statistical uncertainty. The spectrum cannot be explained by any other modified continuum models. We also found that the feature is statistically and systematically significant, and the feature can be represented by adding a Gaussian component centered at $\sim$ 32 keV, with a width of $\sim$6 keV. Althernatively, this feature can be explained by a recombination edge emission component with K-edge energy and electron temperature of $\sim$27 keV and $\sim$11 keV, respectively.

Considering that the feature is K-shell structures of highly-ionized heavy elements

produced via the rp-process, and taking into account the gravitational redshift on the NS surface of 0.23, the Gaussian centroid energy indicates the atomic number of Z =59 - 63, or Pr to Eu. Whereas the K-edge energy indicate Z = 48 and 49, namely, Cd and In. In the latter interpretation, these elements are consistent with theoretical studies (e.g., Schatz et al. 2001 and Elomaa et al. 2009).

The interpretation of the recombination edge emission suggests that these heavy elements are synthesized in Type-I bursts. There, the elements are highly photoionized, under illumination by the hard X-rays from the hot coronal flow, to produce a recombination-edge feature at $\gtrsim$ 27 keV in the observer frame. To explain the observed flux ($\sim 5 \times 10^{36}$ ph $s^{-1}cm^{-2}$), the required amount of relevant elements is approximately seven orders of magnitude higher than the solar abundance value. This value is in good agreement with the simulation study by Schatz et al. (2001). From our study, the 30 keV feature has been identified with the recombination emission from highly ionized Cd or In, which are synthesized via the rp-process during the Type-I burst.

Contents

List of Figures

List of Tables

Chapter 1

INTRODUCTION

A low-mass X-ray binary (NS-LMXB) is composed of a Roche-lobe-filling low-mass star and a mass accreting, weakly magnetized neutron star. The matter, which is continuously accreted on the neutron star's surface, is compressed and heated, and occasionally undergoes unstable thermonuclear flashes called Type-I X-ray bursts. These X-ray bursts involve nucleosynthesis, a process in which hydrogen undergoes unstable nuclear fusion and successively transforms into elements from helium to carbon over time scales of ~ 1 min. The fusion may proceed further to iron and beyond, mainly via the rapid proton-capture process (rp-process; Wallace & Woosley 1981); the surface of an accreting neutron star could provide a unique laboratory where a series of heavy elements beyond iron are synthesized within short time periods in a hydrogen-dominated environment created by the accreting matter. Although studied theoretically (Schatz et al., 2001), the rp-process on accreting neutron stars lacks direct evidence. This study searches for the spectral features of heavy elements in the NS-LMXB spectra, in energies above 10 keV where the K-shell energy levels fall.

NS-LMXBs have two spectral states called soft state and hard state, which are realized when the mass accession rate from the donor star is higher and lower, respectively. In the soft state, an optically thick accretion disk is formed in close proximity to the surface of a neutron star, and its emission makes the system appear bright in soft X-rays. In the hard state, however, the accretion disk is truncated at a radius far from the neutron star's surface, and turns into an optically thin, hot flow called corona. As this corona strongly Comptonizes blackbody photons from the heated neutron-star surface, the spectra extend to ~ 100 keV (Sakurai et al. 2012, 2014). Evidently, data in the hard state are better suited to searching for heavy-element spectral features because the emission in the range

> 10 keV would be feeble compared to that in < 10 keV, when a source is in the soft state.

Aquila X-1 (hereinafter referred to as Aql X-1) is one of the most studied NS-LMXBs characterized by recurrent X-ray outbursts. Observed seven times by the Japanese X-ray satellite *Suzaku* from September 28 to October 30, 2007, this binary is most suitable for studying nucleosynthesis processes as it produces Type-I bursts. Moreover, it is nearer and usually undergoes the hard state in the rise and decay phases of its outbursts, which recur at typical intervals of several months to a few years.

Sakurai et al. (2012) analyzed the spectra of Aql X-1 in these *Suzaku* observations and successfully constructed a spectral model that could describe both soft-state and hard-state spectra of Aql X-1. In addition, they noted a hump structure around 30 keV, above their successful continuum modeling, in the spectra captured when the object was in a bright hard state. However, they did not investigate these features any further. In the present thesis, we study this hump structure through a more detailed re-analysis o f the same archived *Suzaku* datasets as those used by Sakurai et al. (2012, 2014). After confirming the statistical and systematical significance of the feature, we attempt to interpret the feature as K-shell structures of heavy elements with atomic numbers $Z \sim 50$ that are produced on the surface of the neutron-star via the rp-process. The results are expected to provide the world's first observational confirmation of this process in astrophysics.

In Chapter 2, we review neutron stars and nuclear flashes in the NS-LMXB systems. Chapter 3 presents a description of Aql X-1 and a summary of previous studies of this binary. Instrumentations of *Suzaku* and observations of Aql X-1 are given in Chapter 4 and Chapter 5, respectively. Chapter 6 presents the results of spectral analysis and examination of the feature's significance. Chapter 7 details the results of the analysis and an interpretation of the excess feature. Finally, conclusions are stated in Chapter 8.

Chapter 2

REVIEW

2.1 Neutron Star

The concept of a neutron star was proposed by Lev Landau shortly after the discovery of neutrons by James Chadwick in 1932. On November 28, 1967, Bell Burnell and Antony Hewish discovered a radio pulsation with a period of 1.337 s from a radio source (radio pulsar) later named PSR 1919+21; pulsars are fast-spinning neutron stars. Such pulsations as short as $\sim$ 1.3 s cannot be achieved by normal stars. Hewish came to the conclusion that the object was a white dwarf or a neutron star. The first detection of electromagnetic signals from a neutron star, however, had been achieved in 1962, when Giacconi et al. (1962) using a sounding rocket detected strong X-rays from Scorpius X-1, the brightest celestial X-ray source later conceptualized as a mass-accreting neutron star. This was the first official discovery of the neutron star. Hewish and Sir Martin Ryle jointly received the Nobel prize in physics for their role in the discovery of pulsars.

As suggested by Baade & Zwicky (1934), a neutron star is born from the remnants of a core-collapse supernova. Because a neutron star is sustained by neutron degeneracy, its radius and mass are calculated to be $\sim$ 10 km and $\sim$ 1.4 $M_{\odot}$, respectively. The density of a neutron star is approximately three times the nuclear saturation density ($\sim 2.8 \times 10^{14}$ g/cm^3). Such high-density conditions often force the emergence of exotic particles such as kaon condensates and lambda hyperons. Many theoretical studies suggest that a neutron star's interior contains these strangeness particles, but the prediction of the same is inconclusive because different studies indicate different equations of states (EoSs) of the nuclear matter, as shown in Figure 2.1 (e.g., Glendenning & Schaffner-Bielich 1998, Lattimer & Prakash 2001). Neutron stars provide a powerful tool to reveal the physics of

cold dense matter. The EoSs can be constrained directly by measuring a neutron star's mass and radius. However, neutron star parameters, especially the radius, are difficult to determine. Extensive observations are being conducted to simplify determination of the parameters. For instance, in a recent study, a neutron star of ~ 2 $M_\odot$ was discovered (Demorest et al., 2010), and some EoSs were ruled out by this discovery.

Some neutron stars form binaries with normal stars. In this case, mass accretion occurs when binary separation distance is small enough. These mass-accreting binaries are classified as high-mass X-ray binaries (HMXBs) and low-mass X-ray binaries (LMXBs), depending on their companion's mass. Table 2.1 lists major properties of these two classes of neutrons. The most important difference between these classes is the magnetic field strength of their respective neutron stars. The effect of the magnetic field strength is determined by a quantity called Alfven radius, which is defined as the radius where the ram pressure of the accreting matter is counter-balanced by the magnetic pressure of the neutron star. The ram pressure is given by

$$p_{\rm ram} = \frac{1}{2}\rho v^2, \tag{2.1}$$

where ρ and v are the density and velocity of the accreting matters, respectively. The magnetic pressure is given by

$$p_{\rm mag} = \frac{B^2}{8\pi} \tag{2.2}$$

where B is the magnetic field strength. Assuming a dipole magnetic field of $B = \mu/r^3$ with μ as the magnetic dipole moment, and assuming that the matter moves in spherical radial free fall, the velocity is written as $v = v_{\rm ff} = \sqrt{2GM/r}$, where G is the gravitational constant and M is the mass of the neutron star. By continuity, $\rho = \dot{M}/(4\pi v_{\rm ff} r^2)$, where $\dot{M}$ is the mass accretion rate onto the neutron star, is required. From these equations, we finally obtain

$$r_{\rm A} = \left(\frac{\mu^4}{2\pi GM\dot{M}}\right)^{1/7}. \tag{2.3}$$

In NS-HMXBs, the neutron stars have a $B \sim 10^{12}$ G; we hence obtain $r_{\rm A} \sim 10^8$ cm, which is much larger than the radius of the neutron star (~ 10 km). At a radius near $r_{\rm A}$, the matter is captured by the magnetic field lines and falls on the magnetic poles of the neutron star's surface. As a result, this type of neutron star emits pulses synchronized with its rotation, and hence is observed as an accretion-powered pulsar. In contrast, the neutron stars in NS-LMXBs are only weakly magnetized by $B \sim 10^{7-9}$ G; the calculated $r_{\rm A}$ is less than 10 km. Thus, matter can freely accrete onto the neutron star's surface,

especially along the equatorial regions, without being hindered by the star's magnetic field. The accreted matter is compressed, heated, and subjected to thermonuclear flashes. The phenomenon is known as a Type-I burst and may contribute to the nucleosyntheses across the universe. This interesting aspect of NS-LMXB is the subject of our study.

Most of these accreting neutron stars were discovered by the Uhuru satellite (Giacconi et al. 1971; Forman et al. 1978, for catalogue). More than 150 binary neutron stars have been catalogued thus far (Lui et al. 2007), and their X-ray emission mechanisms have been studied since the 1980s by the *Tenma* (Tanaka et al., 1984), *EXOSAT* (White & Peacock, 1988), *Ginga* (Makino & ASTRO-C Team, 1987), and succeeding satellites. In the next section, we summarize the properties of the NS-LMXBs, which are our targets for observation.

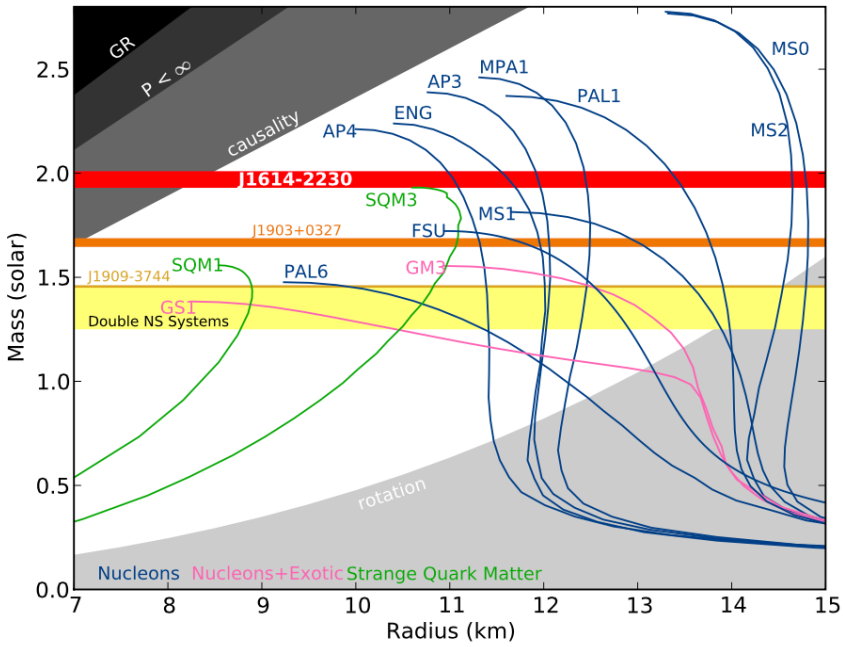

Figure 2.1: Mass vs. radius relations in neutron stars. Solid curves show the EoSs calculated under several conditions. Dark blue lines assume nucleons that make up the constituents of the neutron star's interior. Magenta curves consider nucleons and exotic particles, and green lines consider strange quark matters. Red and orange bands are the measured masses of the neutron stars based on observations. This figure was taken from Demorest et al. (2010).

Table 2.1: Basic properties of HMXB and LMXB (Tauris & van den Heuvel, 2006)

	HMXB	LMXB
X-ray spectra	$kT > 15$ keV (hard)	$kT < 10$ keV (soft)
Type of time variability	regular X-ray pulsations	irregular variations
	no X-ray bursts	often X-ray bursts
Accretion mode	wind capture	Roche-lobe overflow
Timescale of accretion	10^5 yr	10^{7-9} yr
Accreting compact star	high B-field neutron star	low B-field neutron star
Spatial distribution	Galactic plane	Galactic bulge
Stellar population	young, age $< 10^7$ yr	old, age $> 10^9$ yr
Companion star	luminous, $L_{\rm optical}/L_{\rm X} > 1$	dim

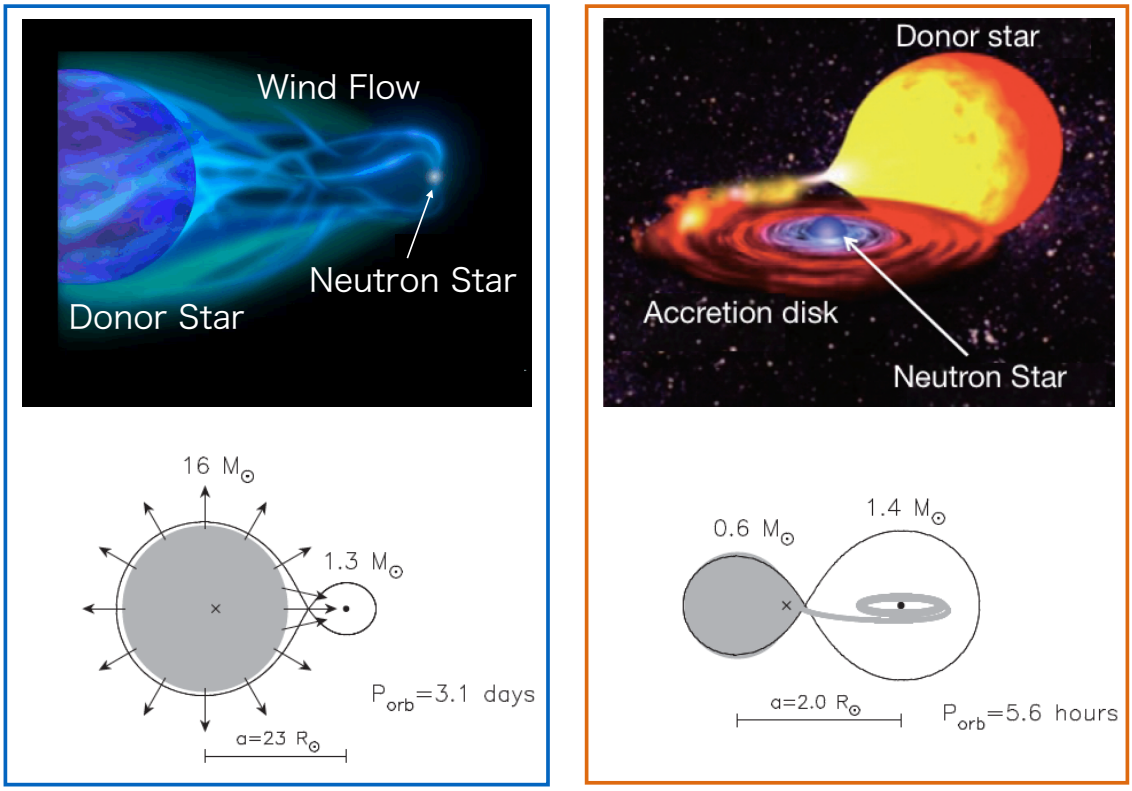

Figure 2.2: Comparison of accretion mechanisms of HMXBs (left) and LMXBs (right). Top panels show an artist's rendition and bottom panels show schematic of the accretion mechanisms (taken from Tauris & van den Heuvel 2006). In an HMXB, wherein the optical companion causes massive stellar winds, mass accretion begins as the neutron star through its gravitational pull captures a segment of the stellar winds. In an LMXB with feeble stellar winds, the accretion occurs when the companion fills its Roche lobe and the matter overflows through the inner Lagrangian point.

2.2 Low-mass X-ray Binaries

2.2.1 Roche lobe over flow and disk formation

Since NS-LMXBs do not possess strong stellar winds, their mass transfer occurs via the Roche lobe overflow, wherein the companion star exceeds its limiting gravitational equipotential in size. This is due to either the expansion of the companion star in the course of its stellar evolution or the reduction in binary separation due to emission of gravitational radiation and/or magnetic braking. Let us visualize two point masses, M_1 and M_2, in a circular orbit of radius R, with an orbital period of $P_{\rm orb}$ and orbital angular velocity of $\omega = 2\pi/P_{\rm orb}$. Then, the total potential $\Phi(r)$ is written as

$$\Phi(r) = -\frac{GM_1}{|r - r_1|} - \frac{GM_2}{|r - r_2|} - \frac{1}{2}[\omega \times (r - r_{\rm c})]^2 \tag{2.4}$$

where $|r - r_1|$ and $|r - r_2|$ are the distances from the centers of M_1 and M_2 to the test mass at r, respectively.

A schematic drawing of equation (2.4), called the Roche potential, is shown in Figure 2.3. The Roche potential has a "figure-of-eight" shape. The outer layer of the companion star falls to the compact star through the inner Lagrange point $\rm L_1$, which is defined as the saddle point of the gravitational potential between the two stars in the binary.

Because the matter accreting through $\rm L_1$ towards the neutron star has a specific angular momentum, J, it ultimately settles on a circular ring with Keplerian rotation. The radius of the ring, which is called circularization radius, is given as

$$R_{\rm circ} = \frac{J^2}{GM_{\rm NS}}. \tag{2.5}$$

Within $R_{\rm circ}$, matter comes together in a disk shape, which is called an accretion disk. The accreted matter gradually falls to the neutron star by losing both angular momentum and dynamic energy (gravitational energy plus kinetic energy). At a large radii, this infall of radial matter is governed by outward transept of the angular momentum. As the disk closer to the main neutron star, its radial flow becomes regulated mainly by the rate at which the dynamic energy is dissipated.

2.2.2 X-ray emission and spectral states

Here, we analyze whether the emission from an accreting neutron star is in the X-ray band (i.e., with energies of a few keV). The matter accreting onto the neutron star's

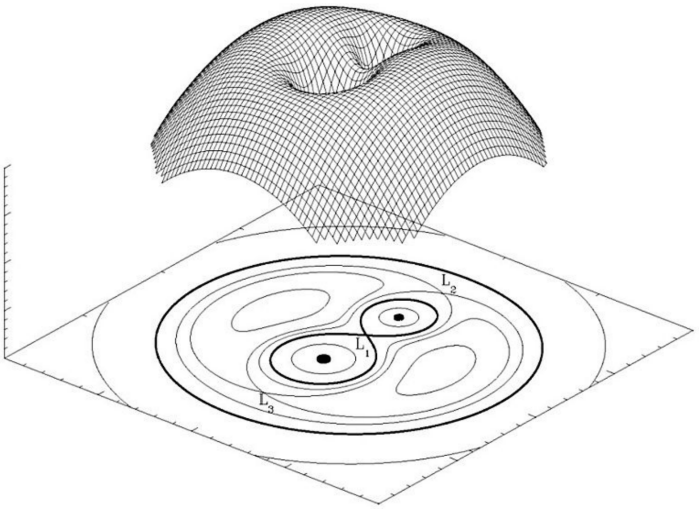

Figure 2.3: Representation of the Roche equipotential in a binary system with a mass ratio of 2. Bottom of the figure shows equipotential surfaces plotted in the 2D plane. L_1, L_2, and L_3 are the Lagrange points where the effects of gravity cease. When one star fills its Roche lobe, the matter can flow through the saddle point L_1 to the other star. This figure was taken from van der Sluys (2006).

surface is thermalized and cooled. If we suppose that the neutron star has a mass of M and the accreting matter has solar abundance, then the Eddington luminosity, at which radiative pressure and gravity are balanced, is written by

$$L_{\rm Edd} = 1.5 \times 10^{38} \left(\frac{M}{M_{\rm sun}} \right) \ {\rm erg \ s^{-1}} \tag{2.6}$$

A typical neutron star with a mass of 1.4 $M_\odot$ has $L_{\rm Edd} = 2.1 \times 10^{38}$ erg s^{-1}. Assuming that this value is emitted as blackbody radiation from the neutron star's surface with an area of $4\pi R_{\rm NS}^2$, the blackbody temperature $T_{\rm BB}$ is estimated as

$$\sigma T_{\rm BB}^4 = \frac{L_{\rm Edd}}{4\pi R_{\rm NS}^2} \quad \text{i.e.} \quad T_{\rm BB} \sim 2 \ {\rm keV} \tag{2.7}$$

where $R_{\rm NS} = 12$ km is a canonical neutron-star radius and σ is the Stefan–Boltzmann constant. Because $T_{\rm BB}$ value is in the X-ray band, NS-LMXBs become luminous X-ray sources.

In practice, the X-ray emission in an NS-LMXB occurs not only from the neutron star's surface but also from the original accretion disk. If we suppose that the disk follows

an optically thick, geometrically thin condition and that matter falls over a radial distance Δr in unit time, then the gravitational energy is released at a rate of $\dot{U} = (GM\dot{M}/r^2)\Delta r$. The concept of standard accretion disk (Shakura & Sunyaev 1973) assumes that 0.5 $\dot{U}$ is converted to the Keplerian rotational energy of matter, and the remaining 0.5 $\dot{U}$ is emitted from both sides of a disk annulus of radial thickness Δr as the local blackbody radiation. The 50-to-50 energy division is a result of Virial theorem. By equating 0.5 $\dot{U}$ with the annulus luminosity, $2 \times 2\pi r\ \Delta r\ \sigma T(r)^4$, we obtain

$$\sigma T(r)^4 = \frac{GM\dot{M}}{8\pi r^3}, \quad \text{or} \quad T(r) \propto r^{-3/4} \tag{2.8}$$

where $T(r)$ is the disk temperature at a radius r from the neutron star. A more detailed formalism is given in §2.3.1. Thus, the disk becomes hotter towards the smaller r, and its integrated emission becomes a superposition of the blackbody spectra with a range of temperatures, which is known as "multi-color blackbody radiation". The predicted spectrum was observationally confirmed by Mitsuda et al. (1984) and Makishima et al. (1986).

When $\dot{M}$ is fast, i.e., the source luminosity is above $\sim 0.1 L_{\rm Edd}$, the standard accretion disk is thought to continue down to $r \sim R_{\rm NS}$. Then, the overall X-ray spectrum is composed of two components with equal bolometric luminosities: a softer multi-color blackbody from the standard accretion disk and a harder single-temperature blackbody from the neutron star's surface. The latter results from the thermalization of Keplerian energy at $r \sim R_{\rm NS}$, and is characterized by a temperature comparable to that in equation (2.7). When a source exhibits this type of spectrum, it is said to be in the soft state as it falls steeply to a typical photon energy above $\sim$ 10 keV.

As $\dot{M}$ decreases, a reduced emissivity causes the innermost part of the disk to make a transition into an optically thin, geometrically thick condition, which is called coronal flow or simply "corona." As the ion-to-electron coupling weakens, ions in the flow attain an extremely high temperature, close to their free-fall temperature ($\sim$ 200 MeV), and accrete rather spherically onto the neutron star's surface to heat it. Electrons in a coronal flow have a much lower temperature ($kT_{\rm e} = 50 - 100$ keV) as they are strongly cooled when they thermally Comptonize softer X-rays from the heated neutron star's surface. Because this $kT_{\rm e}$ is still higher than that in equation (2.7), the Comptonized photons form an extremely hard X-ray continuum extending to energies up to $\sim$ 100 keV. In this case, the source is said to be in the hard state.

2.2.3 Recurrent outbursts

Some NS-LMXBs exhibit long-term, large-amplitude luminosity changes, known as outbursts. The typical outburst light curves of several NS-LMXBs are shown in Figure 2.4 (left panel). In a typical outburst, the X-ray luminosity increases by at least five orders of magnitude. In some cases, the outbursts recur with relatively well-defined intervals, but in other cases, the outbursts are too infrequent to be called "recurrent." The basic idea of an outburst was proposed by Osaki (Osaki, 1974), and the corresponding theories were formulated by Meyer and Meyer-Hofmeister (1980), Cannizzo (1993, 1998), and Osaki (1996). In this model, an outburst operates because of hysteresis relation between the surface density, Σ, and the vertically integrated viscous stress, $\nu\Sigma$ (ν is the kinematic viscosity coefficient), at a fixed radius of the accretion disk. When plotting an equilibrium solution on $\log \nu\Sigma$–$\log \Sigma$ plane, we obtained an S-curve relation, such as in Figure 2.4 (right panel). In a quiescent phase, the disk is located at a larger radius, almost comparable to the radius of the Roche potential. As the accreting matter continues to pile up in the disk, the disk evolves from A $\rightarrow$ B in Figure 2.4 (right). When the surface density approaches a critical value of $\Sigma_{\rm max}$, the state of the disk jumps from B $\rightarrow$ C. At this time, the temperature increases, and the matter is ionized as a result. The increase in viscosity causes the matter to fall to the central object and produce an outburst. Because the mass infall rate exceeds the rate from the companion, the surface density and the temperature of the disk gradually decrease (C $\rightarrow$ D). When the surface density reaches a minimum value $\Sigma_{\rm min}$, the disk reverts to state A.

Through the outbursts, a transient NS-LMXB exhibits transitions between the soft and hard states. The typical spectral shapes of these states are shown in Figure 2.5. When a transient NS-LMXB begins an outburst, it is usually in the hard state. Then, the source becomes brighter in a relatively short time (e.g., a week or so), and at a certain luminosity, it makes a transition to the soft state Ono et al. (2017). This event is observed as a sudden increase in X-ray intensity below $\sim$ 10 keV, accompanied by a decrease in intensity at higher energies. After reaching the peak outburst, the source gradually becomes dimmer but remains in the soft state at a much lower luminosity than the transition threshold in the rising phase. This is due to a hysteresis effect, which is similar to the case of Figure 2.4 (right). Finally, the source makes a transition back to the hard state before fading away.

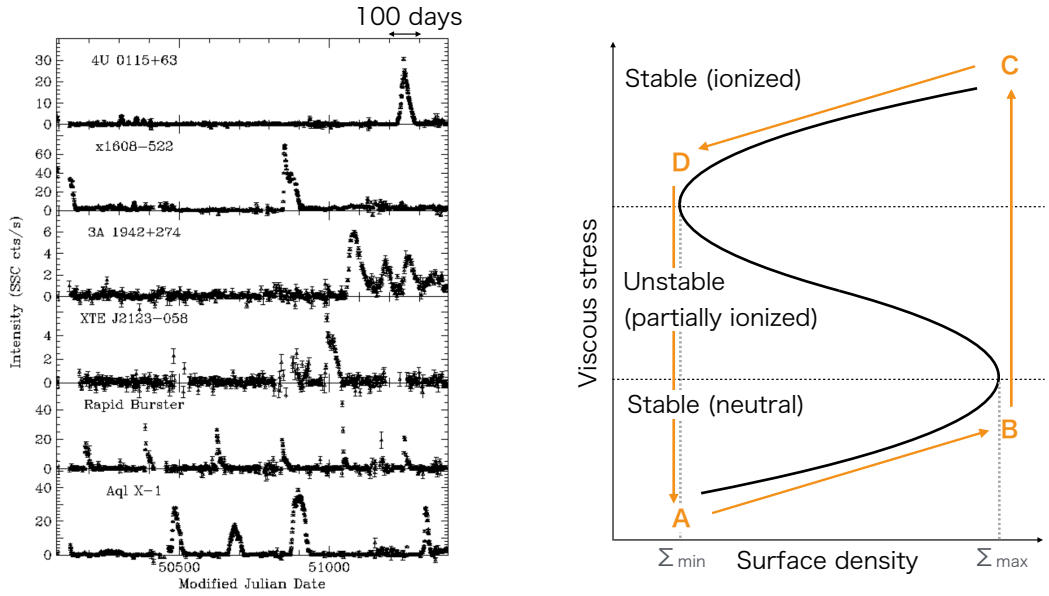

Figure 2.4: (Left) Light curves of six neutron-star transients taken by ASM/RXTE in an energy range of 1.5–12 keV (taken from H. Bradt et al. 2000). (Right) S-curve in $\log \nu\Sigma$–$\log \Sigma$ plane (see text).

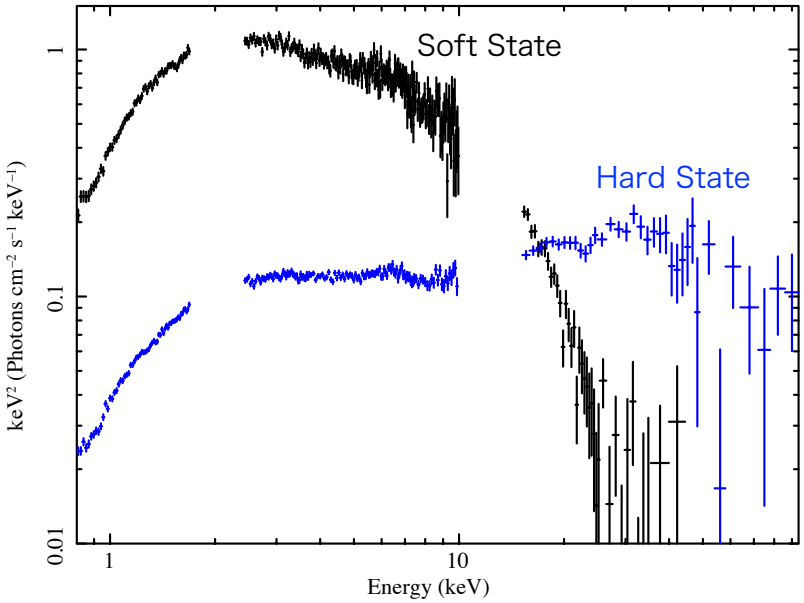

Figure 2.5: Typical νF_ν spectra of the NS-LMXB Aql X-1, in the soft state (black) and the hard state (blue).

2.3 The Accretion Disk

In many binary systems, including binary neutron stars and black holes, the accreting matter form a disk around the compact object because of their angular momenta. The mass accretion rate and viscosity play an important role in the accretion disk structure and geometry. The concept of accretion disk was introduced by Lynden-Bell (1969) and formulated by Shakura & Sunyaev (1973) as a standard disk, as mentioned in §2.2.1. In this section, we describe the concept of standard accretion disk and a spectral model for its integrated emission.

2.3.1 Standard accretion disk

Generally, matter in an accretion disk experiences the following four forces: gravitational force, centrifugal force, Coriolis force, and pressure gradient. The standard model assumes that the radial velocity is negligible (i.e., no Coriolis force) and the radial pressure gradient is much smaller than the gravitational force. As a result, the overall flow forms at each successive radius r a geometrically thin disk that rotates with a Keplerian velocity, v_ϕ

$$v_\phi = \sqrt{\frac{GM}{r}}, \tag{2.9}$$

where M is the mass of the compact object. Since v_ϕ increases with a decrease in r, the inner layers have higher angular velocity. Hence, the angular momentum is transferred via viscosity from inner to outer regions. The viscosity generates heat, which is assumed to be efficiently transferred to the disk surface via conduction and locally emitted as blackbody radiation. Assuming that the rate of viscosity heating is balanced with the radiative cooling rate, the disk temperature profile can be given approximately as in equation (2.8). A more detailed calculation considering the angular-momentum transport yields

$$T(r) = \left[\frac{3GM\dot{M}}{8\pi r^3\sigma}\left(1-\sqrt{\frac{r_{\rm in}}{r}}\right)\right]^{1/4} \tag{2.10}$$

where $r_{\rm in}$ is the radius of the inner-most disk, where the viscous stress is assumed to have vanished.

Amid local blackbody radiation, the photon flux at an arbitrary radius r of the disk can be given from the Stefan–Boltzmann's law as

$$F(r) = 2\sigma T(r)^4 = \frac{3GM\dot{M}}{4\pi r^3}\left(1-\sqrt{\frac{r_{\rm in}}{r}}\right). \tag{2.11}$$

The overall luminosity from the disk surface $L_{\rm d}$ is obtained by integrating equation 2.11,

$$L_{\rm d} = \int_{r_{\rm in}}^{\infty} \frac{3GM\dot{M}}{2r^2}\left(1-\sqrt{\frac{r_{\rm in}}{r}}\right)dr = \frac{GM\dot{M}}{2r_{\rm in}}. \tag{2.12}$$

As observed before, this is exactly half the gravitational energy release per unit time as the matter keeps falling from infinity to $r_{\rm in}$. According to the Virial theorem, the remaining half is stored at $r = r_{\rm in}$ as the Keplerian rotational energy. Furthermore, if we use the approximation of equation (2.8), we obtain $\dot{M} = 8\pi r^3 \sigma T(r)^4/GM$, which can be substituted into equation (2.11) to yield

$$L_{\rm d} = 4\pi r_{\rm in}^2 \sigma T_{\rm in}^4 \tag{2.13}$$

with $T_{\rm in} \equiv T(r_{\rm in})$. This form eventually becomes the Stefan–Boltzmann's law.

2.3.2 Multi color disk interpretation

As already discussed in §2.2.1, the multi-color disk (MCD) model is a spectral model that explains the integrated spectrum from a standard accretion disk (Mitsuda et al. 1984; Makishima et al. 1986). This is obtained by summing up the Plank distribution from different parts of the disk. The MCD spectrum is obtained by integrating from the innermost disk radius $r_{\rm in}$ to the outermost disk radius $r_{\rm out}$;

$$f(E) = \int_{r_{\rm in}}^{r_{\rm out}} B[E,T(r)]2\pi r\cos i dr = \int_{T_{\rm out}}^{T_{\rm in}} (T/T_{\rm in})^{-11/3} B[E,T(r)]dT/T_{\rm in}, \tag{2.14}$$

where

$$B[E,T(r)] = \frac{2}{h^2c^2}\frac{E^3}{\exp[hE/k_{\rm B}T(r)]-1} \tag{2.15}$$

is the Plank distribution, i is an inclination angle, and $T_{\rm out} \equiv T(r_{\rm out})$.

In Figure 2.6 (left) and (right), a sample of the MCD spectrum and a schematic drawing of MCD can be observed. Generally, $kT_{\rm in}$ does not exceed the temperature of the neutron star surface, ($kT_{\rm bb} \sim 2$ keV, at $L_{\rm Edd}$). Therefore, the typical $kT_{\rm in}$ is below a few keV. Because $kT_{\rm out}$ is usually outside of the X-ray band (UV or optical), the spectra are determined by the parameters, $r_{\rm in}\cos i$ and $kT_{\rm in}$. For energies $E \gtrsim 2kT_{\rm in}$, the spectrum is well described by a single blackbody temperature, $T_{\rm bb} = 0.7T_{\rm in}$. When $kT_{\rm out} \ll E \lesssim 0.3kT_{\rm in}$, the MCD spectrum takes the shape of power law with an energy index of 1/3. The total luminosity of the MCD component is represented by equation (2.13)

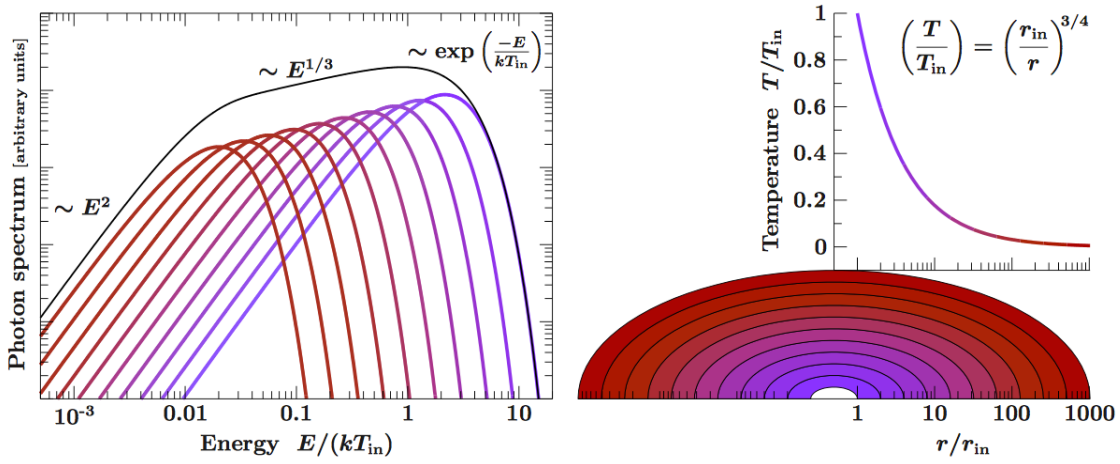

Figure 2.6: (left) Spectrum resulting from the superposition of multiple blackbody spectra originating from individual rings in a standard accretion disk (taken from Hanke 2011). (right) Schematic distribution of disk temperature $T(r)$.

2.4 Comptonization

In the hard state (§2.2.2), which is realized a few percentage points below $L_{\rm Edd}$, LMXBs take on the power-law shape spectra, with a high energy roll over (Figure 2.5 blue). This is because low-energy photons in the optically thick emissions from a neutron star's surface and/or the inner part of a binary's accretion disk are Compton-scattered by hot thermal electrons that constitute the optically thin inner accretion flow (or "corona"; §2.2.2). In this section, we provide an introduction to the Comptonization.

2.4.1 Compton kinematics

Compton scattering is the most basic interaction between electrons and photons. We suppose that the incident (scattered) electron's velocity, photon energy, and angle are β_0 (β_1), ϵ_0 (ϵ_1), and θ_0 (θ_1) in the laboratory frame, K, respectively. A final-state energy of photon is then written as

$$\epsilon_1(\theta_1', \phi; \epsilon_0, \beta_0) = \frac{\epsilon_0\gamma_0(1-\beta_0\cos\theta_0)}{1+\frac{\epsilon_0\gamma_0(1-\beta_0\cos\theta_0)}{m_ec^2}(1-\cos\theta_1')} \times \gamma_0[1+\beta_0(\cos\theta_0'\cos\theta_1' - \sin\theta_0'\sin\theta_1'\cos\phi)] \tag{2.16}$$

where

$$\theta_1' = \tan^{-1}\left[\sin\frac{\sin\theta_0}{\gamma_0(\cos\theta_0 - \beta_0)}\right], \tag{2.17}$$

$m_e c^2 = 511$ keV is the electron rest mass and ϕ is the twist angle of $\vec{\epsilon_1'}$ around $\vec{\beta_1'}$ in the K$'$ frame. The primes are the quantities measured in the electron rest frame K$'$ (index 0 and 1 bear the same meaning as the K frame). In the limit of $\beta = 0$, equation (2.16) is reduced to the normal Compton scattering; therefore, the final photon energy is expressed as

$$\epsilon_1 = \frac{\epsilon_0}{1 + (\epsilon_0/m_e c^2)\,(1 - \cos\theta_0)}. \tag{2.18}$$

At rest, the electron receives energy from the photon. In contrast, when it has higher kinetic energy compared to the photon, the electron transfers the net energy to the photon. The latter is called inverse Compton scattering.

The differential cross-section for Compton scattering is given by the Klein–Nishina formula (Klein & Nishina 1929)

$$\frac{d\sigma_{\rm KN}}{d\Omega} = \frac{3}{16\pi}\sigma_{\rm T}\left(\frac{\epsilon_1}{\epsilon_0}\right)\left(\frac{\epsilon_0}{\epsilon_1} + \frac{\epsilon_1}{\epsilon_0} - \sin^2\theta_1\right), \tag{2.19}$$

where

$$\sigma_{\rm T} = \frac{8\pi}{3}r_0^2 = 6.652 \times 10^{-25}\ \ {\rm cm}^2 \tag{2.20}$$

This is the classical Thomson cross-section, with $r_0 = 2.81 \times 10^{-13}$ cm as the classical electron radius. The total cross-section is obtained by integrating equation (2.19) with respect to the scattered angle, θ (Rybick & Lightman, 1986) as

$$\sigma_{\rm KN} = \frac{3}{4}\sigma_{\rm T}\left[\frac{1+x}{x^3}\left\{\frac{2x(1+x)}{1+2x} - \ln(1+2x)\right\} + \frac{1}{2x}\ln(1+2x) - \frac{1+3x}{(1+2x)^2}\right], \tag{2.21}$$

where $x = h\nu/(m_e c^2)$.

2.4.2 Comptonization of monochromatic photons

Let us consider Compton scattering between photons with monochromatic energy and electrons with temperature $kT_{\rm e}$, and size l of number density n_e. The mean free path of the photons due to Compton scattering is $\lambda = (n_e\sigma)^{-1}$. When $l \gg \lambda$, the photons are scattered by electrons several times before escaping the electron cloud; thus, the initial photon spectrum, with a $\delta-$function shape, is modified and broadened. In contrast, if $l \ll \lambda$, the scattering will be to a minimum. Therefore, if we introduce the optical depth as

$$\tau = \sigma_{\rm T} n_{\rm e} l, \tag{2.22}$$

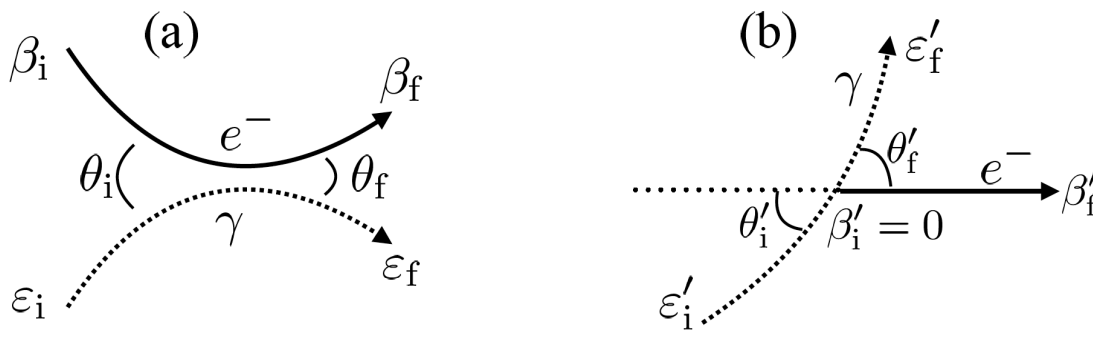

Figure 2.7: Geometries of the Compton scattering in the observer's frame K and in the electron rest frame K' (taken from Sakurai, 2015).

where the Compton cross section is approximated by $\sigma_{\rm T}$, then the resulting emission spectrum will depend on the energy distribution of the electrons and the mean number of scatterings.

If we consider the case where $kT_{\rm e} \gg h\nu$, then the repeated scatterings of soft photons by hot electrons will produce a hard tail in the photon spectrum, extending blueward of the original line spectrum. As illustrated in Figure 2.8, this effect is determined by the Compton y-parameter,

$$y = \frac{4kT_{\rm e}}{m_e c^2}\max(\tau, \tau^2). \tag{2.23}$$

The first factor, $4kT_{\rm e}/m_e c^2$, is the energy gain of a photon per scattering event, namely $\Delta\nu/\nu$, and $\max(\tau, \tau^2)$ is the number of scattering events. If $\tau \ll 1$, then the number of scattering events is $\sim \tau$. At this time, the resulting spectrum becomes a power law (Figure 2.8) with a cutoff at $h\nu \sim 3kT_{\rm e}$. The photon index of the power law is determined by the Compton y-parameter as

$$\Gamma = -\frac{1}{2} + \sqrt{\frac{9}{4} + \frac{4}{y}}. \tag{2.24}$$

Thus, the power law becomes flatter (Figure 2.8) with an increase in y. For $y = 1$, we obtain $\Gamma = 2.0$. The power-law spectrum extends up to $E \sim kT_{\rm e}$ and decreases exponentially above the energy.

When τ is large ($\tau \gg 1$), the Comptonized spectrum no longer has a simple cutoff power-law shape. The energies of photons and electrons approach an equilibrium because

of sufficient momentum transfer. As a result, in the high-energy range at $h\nu \sim 3kT_e$, the spectrum becomes blackbody-like, exhibiting a Wien hump, which directly reflects the Maxwellian energy distribution of the electrons. However, Wien spectrum is not tantamount to blackbody (Planck) spectrum, as the photon number is conserved in the former (particularly Compton scattering) but not in the latter.

Generally, in astrophysics, thermal photons instead of monochromatic photons are the sources of seed photons for Comptonization, e.g., blackbody radiation from the neutron star surface or the inner bands of the accretion disk. In this case, the Comptonized spectrum can be represented by the convolution of an input spectrum and the above result for the monochromatic photon. This condition is illustrated in Figure 2.8, where seed photons from a blackbody source with a temperature of $kT_{\rm s} = 0.7$ keV are Comptonized by a thermal electron cloud of $kT_{\rm e} = 100$ keV with various values of τ. Thus, the Comptonized blackbody spectra with $\tau < 2$ are characterized in three sections. In the lowest energy end of $h\nu < 4kT_{\rm s}$, a hump corresponding to a see-through (unscattered) seed photon is observed, and its Rayleigh–Jeans region is relatively well conserved. In the intermediate energies between $\sim 4kT_{\rm s}$ and $\sim kT_{\rm e}$, the spectrum is approximately like a power law, and its photon index is described by equation (2.24). Finally, in the highest energy end of $h\nu > 3kT_{\rm e}$, the spectrum falls exponentially, reflecting only the electron temperature.

2.4.3 Comptonization models

The spectral changes caused by Comptonization are calculated based on the Kompaneets equation (Kompaneets 1956), which describes the evolution of the phase-space density of electrons and photons, as

$$\frac{\partial n}{\partial y} = \frac{1}{x^2}\frac{\partial}{\partial x}\{x^4(n' + n + n^2)\} \quad (x = E/m_e c^2), \tag{2.25}$$

where n is the phase-space density of photons and y is given by equation (2.23).

Equation (2.25), being a complicated, non-linear, partial differential equation, may not yield simple analytic solutions. Therefore, its solutions are usually obtained by numerical codes developed by various authors. In this thesis, we used the codes named `nthcomp` (Lightman & Zdziarski 1987; Lightman et al. 1987; Zdziarski et al. 1996; Zycki et al. 1999) and `compPS` (Poutanen & Svensson, 1996). The former gives a numerical solution for the Kompaneets equation, whereas the latter considering relativistic effects (e.g., Klein Nishina cross-section) calculates the Comptonized spectra by numerically solving a radia-

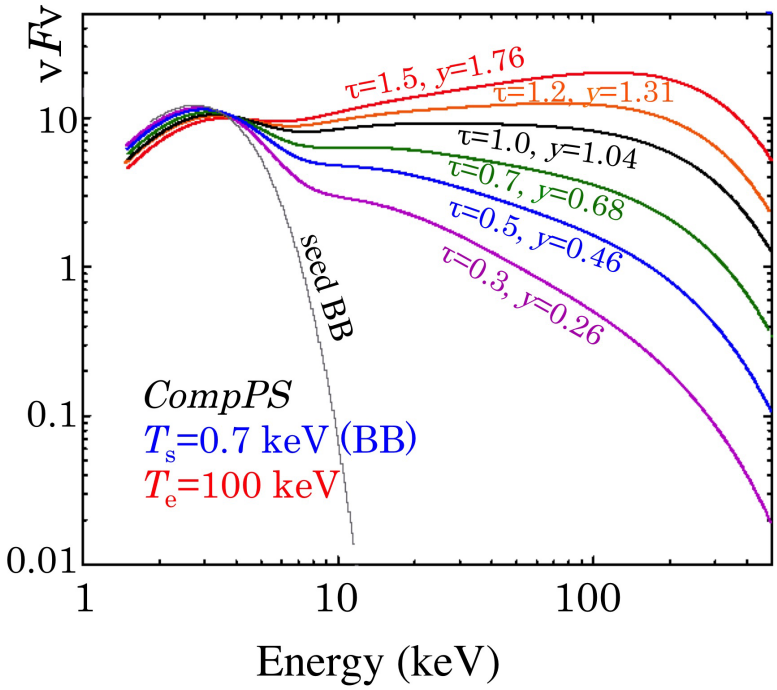

Figure 2.8: Comptonized spectral shapes with several optical depth. Seed photon temperature $T_{\rm s}$ and coronal electron temperature $T_{\rm e}$ are fixed to 0.7 keV and 100 keV, respectively. Gray curve shows a seed blackbody spectrum. This figure was taken from Makishima (2014).

tive transfer equation. The application range of this model is $\tau < 3$, which is determined by its iterative calculation coverage. These models are consistent with the simple blackbody radiation at $\tau \to 0$.

2.5 X-ray Burst and Nucleosynthesis

2.5.1 Type-I X-ray bursts

Since neutron stars in NS-LMXBs are only weakly magnetized, the accreting material can freely spread over their surface. There, matter is compressed, heated, and eventually subjected to thermonuclear flashes, the so-called Type-I X-ray bursts. This is one of the most remarkable features of NS-LMXBs. Since its discovery in 1975 with the *ANS* satellite (Grindlay et al., 1976), the understanding of this explosive phenomenon has been

developed by a series of X-ray missions, including *Hakucho* (e.g., Inoue et al. 1981), *Tenma* (e.g., Waki et al. 1984), *RXTE* (e.g., Strohmayer et al. 1999), *BeppoSAX* (e.g., Boella et al. 1997), and MAXI (Serino et al., 2016). For the sake of reference, Type-II bursts, which have been observed only form one or two sources, are probably due to instabilities in an accretion disk.

Figure 2.9 shows a typical light curve of a Type-I burst. From this, it can be seen that Type-I burst has a short (< 1 s) rise time, followed by an exponential decay on time scales of a few tens of seconds. The burst emission exhibits a blackbody spectrum with a peak temperature of ~ 2 keV and a peak luminosity that can be identified with the $L_{\rm Edd}$ of equation (2.6). During their decay phase, Type-I bursts exhibit spectral softening, reflecting a decrease in the temperature of the atmosphere of a neutron star due to cooling. A burst-active NS-LMXB emits Type-I bursts repeatedly, with typical intervals ranging from hours to days. Moreover, some of these objects occasionally emit the so-called superbursts (Keek et al. 2008, Serino & Iwakiri 2017), which have much longer durations (> 1 hr) than the normal Type-I bursts.

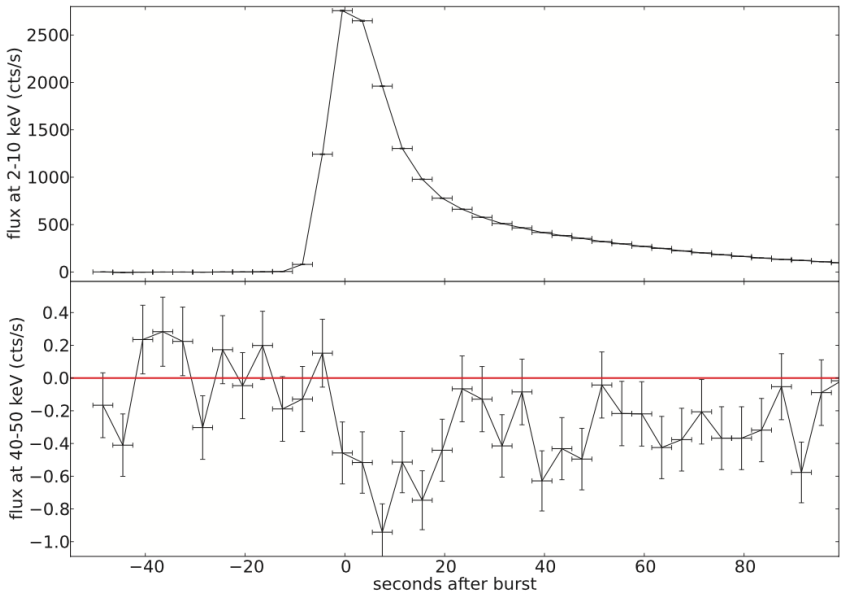

Figure 2.9: Typical light curves of a Type-I burst in 2–10 keV (top) and 40–50 keV (bottom) ranges, observed from Aql X-1 (Chen et al., 2013).

Begining with the pioneering works by Joss and Rappaport (1977) and Taam (1980), theoretical studies of Type-I bursts were conducted in the 1980's. These include Japanese contributions (Fujimoto et al. 1981, Hanawa et al. 1983, Fujimoto et al. 1987), which were carried aut in close collaboration with burst observations using *Hakucho*. Through these theoretical works, Type-I bursts have been interpreted as a result of unstable thermonuclear burning on or beneath a neutron star's surface. This is based on an important observation: the total energy emitted as persistent X-rays from a burst-active NS-LMXB over a sufficiently long period (e.g., a month) is 40–100 times greater than that emitted from all other bursts observed from the same object over the same period. This ratio is in agreement with the ratio of the gravitational energy release by accretion (200 MeV per nucleon) to the typical nuclear reactions (a few MeV per nucleon). In addition, evidence for elements synthesized in thermonuclear ashes are observed in the spectrum (in't Zand & Weinberg 2010; Kajava et al. 2017).

Yet another form of support for the nuclear-reaction interpretation of X-ray bursts comes from an observed luminosity dependence of the burst activity. Although all NS-LMXBs emit Type-I bursts, they stop producing these bursts as they become exceedingly luminous ($> 0.3 L_{\rm Edd}$), or equivalently, $\dot{M} > 10^{-8}\ M_\odot\ {\rm yr}^{-1}$. Under such conditions, the accreting matter on the neutron star's surface would attain temperatures high enough to continuously fuel the nuclear reaction rather than intermittently. Similarly, when light from a source becomes faint, e.g., $< 10^{-2} L_{\rm Edd}$, causing the neuron star's surface to become cooler, it either emits infrequent Type-I bursts or becomes inactive. This is because it would then take a long time for a substantial amount of new matter to accumulate and attain a sufficiently high density that could trigger nuclear reactions even under low temperatures.

Accreting neutron stars in HMXBs are not known to produce Type-I bursts, presumably because these neuron stars are highly magnetized and the accreting matter is funneled to their magnetic poles to attain very high temperatures (e.g., > 10 keV). As a result, the nuclear reactions would occur continuously, like in exceedingly luminous NS-LMXBs.

2.5.2 Nucleosynthesis on neutron stars

As already stated, X-ray bursts are a manifestation of explosive nucleosynthesis in binaries, accreting mass on or underneath the neutron star's surface. Although the synthesis is considered to involve a complex chain of nuclear fusion reactions, the largest energy out-

put is available when hydrogen in the accreting material transmutes into helium though the carbon—nitrogen–oxygen (CNO) cycle. In many cases, the triple-alpha reaction, in which three ^{4}He nuclei fuse into one ^{12}C nucleus, is considered to proceed simultaneously.

In an LMXB system, the neutron star's surface could be in a proton-rich environment (unless the donor is a helium star) as it is continuously fed with fresh accreting matter consisting mainly of hydrogen. In that case, the nuclear synthesis will proceed further via the rp-process; Wallace & Woosley 1981). That is, nuclei will successively capture protons faster than the produced proton-rich nuclei experience β^{+} decay. As shown in Figure 2.10, the path of the rp-process runs through a marginally richer proton side on a nuclear chart than stable nuclear burning.

According to theoretical studies (e.g., Schatz et al. 2001, Fisker et al. 2008,José et al. 2010), this process can produce heavy elements beyond iron group. In several pioneering works, Schatz et al. (2001) claimed the process would proceed until all hydrogen atoms were consumed; or, as shown in Figure 2.11, the reaction reaches the so-called SnSbTe cycle, wherein alpha decay prevents the synthesis of heavier nuclei. However, the actual endpoint of this process strongly depends on ignition conditions and the nuclear structure. Fisker et al. (2008) performed numerical simulations of Type-I burst nucleosynthesis under different temperature conditions. They found that the reaction flow reaches $^{93,\ 93}$Pd, when the peak temperature of the corresponding type-I burst is 9.93×10^{8} K. José et al. (2010) also performed a burst simulation with different metallicities and confirmed the creation of heavy elements up to SnSbTe mass region by the rp-process. Elomaa et al. (2009) directly measured the masses of Sb isotopes for the first time, and revealed that the rp-process could not form a closed SnSbTe cycle because of the low proton-separation energy ($\sim$ 424 keV) of ^{106}Sb.

In this way, the theoretical works performed so far agree on the production of heavy elements at least up to the SnSbTe mass region. However, observational evidence of the rp-process on the neutron star's surface is still insufficient.

The superburst phenomenon is also thought to have a close relation to the rp-process nucleosynthesis. If we suppose the nuclear reaction to not proceed beyond carbon and that a large amount of carbon was accumulated, then, at a certain threshold, these carbon nuclei would burn unstably to produce a superburst that is 1,000s of times more energetic than the normal Type-I bursts. Naturally, these superbursts are promising sites for the rp-process, and evidence of spectral features that could be attributed to the synthesized

elements were detected in a superburst spectrum from 4U 1636−53 (Keek et al., 2014).

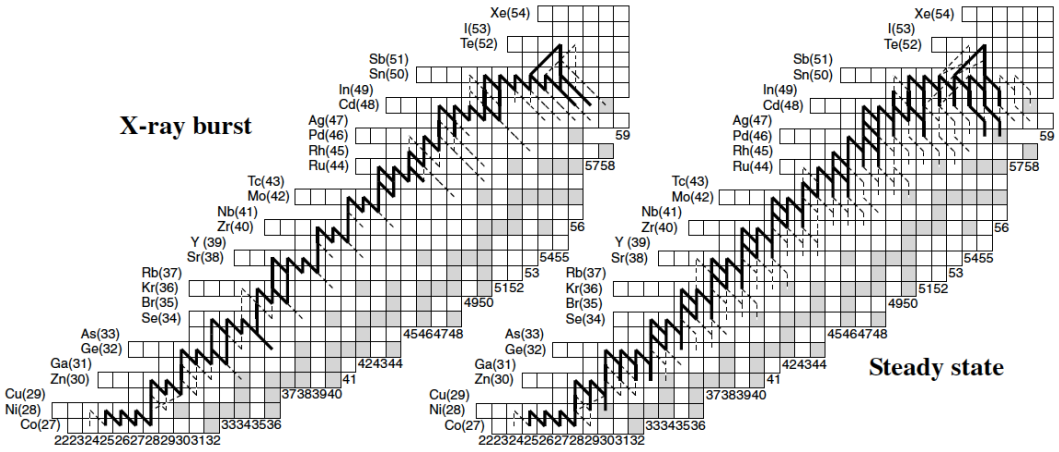

Figure 2.10: The time-integrated reaction flow above Ga during an (left) X-ray burst and for (right) stable burning. Reaction flows of more than 10% (solid line) and of 1–10% (dashed line) of the reaction flow through the 3α reaction (taken from Schatz et al. 2001). This figure was taken by Schatz et al. (2001).

2.5.3 Type-I bursts as an astrophysical probe

Type-I bursts are important from the perspectives of not only nucleosynthesis of heavy elements but also neutron-star diagnostics and other astrophysics problems. Listed below are several examples.

1. In some bursts, the X-ray luminosity L saturates at $L_{\rm Edd}$. By carefully measuring the effective temperature T on that occasion, and utilizing the Stefan-Boltzmann's law as $L = 4\pi R_{\rm NS}^2 \sigma T^4$, $R_{\rm NS}$ can be estimated. The results yield $R_{\rm NS} \sim 12$ km (e.g., Suleimanov et al. 2012).

2. When a Type-I burst ignites on a limited region of the neutron-star surface, X-ray pulsations synchronized with the rotation can be observed until the nuclear burning spreads over the whole surface. This phenomenon, called burst oscillation, provides a rare chance to detect the rotation of neutron stars in NS-LMXBs, which is otherwise difficult to observe. In fact, this oscillation was observed from Aql X-1 at a frequency of 550 Hz, though only for 150 sec (Casella et al., 2008)

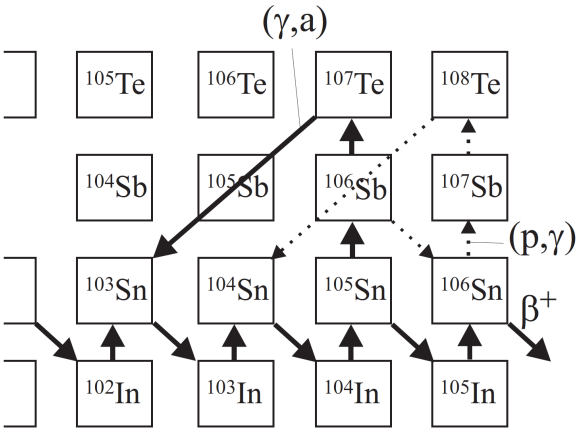

Figure 2.11: The reaction in the SnSbTe cycles during an X-ray burst (taken from Schatz et al. 2001). In the case of proton captures, the arrows indicate the direction of the net flow, namely, the difference of the flow via proton capture, and the reverse flow via (γ,p) photo-disintegration. The line styles are the same as in Figure 2.10.

3. Several authors have reported possible detections of gravitationally redshifted Fe–K absorption lines (or edges) in burst spectra (e.g., Waki et al. 1984). Although the phenomenon is still controversial, a secure confirmation of these lines, followed by an accurate measurement of the gravitational redshift would allow accurate determination of the mass-to-radius ratio of that neutron star, and improve our understanding of the nuclear EoS.

4. Using Type-I burst as a standard candle, Inoue et al. (1981) estimated the distance between our solar system and its galactic center to approximately 8 kpc rather than the value believed at that time, 10 kpc. This and other observations have motivated the International Astronomical Union to revise the distance to the Galactic center from the value of 10 kpc adopted in 1964 to the new value of 8.5 kpc (Kerr & Lynden-Bell, 1986).

Chapter 3

Aquila X-1

3.1 Overview

Aquila X-1, or Aql X-1, first discovered by Kunte et al. (1973), is a typical recurrent transient NS-LMXB, and is located at a distance of 5.2 ± 0.7 kpc (Jonker & Nelemans, 2004). It forms an 18.95-h binary, together with an optical companion whose magnitude in X-ray quiescence is $V = 21.6$ (Chevalier et al., 1999) and estimated mass is ~ 0.76 $M_\odot$ (Mata Sánchez et al., 2017). As illustrated in Figure 3.1, this object exhibits quasi-periodical X-ray outbursts in every 200–300 days (Kitamoto et al. 1993; Šimon 2002), with a typical duration being ~ 1 month. It is also known to produce Type-I X-ray bursts as described in §2.5 (Koyama et al. 1981; Czerny et al. 1987) and superburst (Serino & Iwakiri et al. 2017). During Type-I bursts, X-ray oscillations with a frequency of 549 Hz were discovered by Zhang et al. (1998). This oscillation reveals the spin of the neutron star, although this phenomenon is not yet detected in persistent X-rays from Aql X-1.

3.2 *Suzaku* Observations

Aquila X-1 was observed with *Suzaku* in 2007 and 2011. In this section, we review the results of the *Suzaku* spectral analysis of these observations.

3.2.1 Decaying phase of outburst in 2007

In 2007, Suzaku observed the outburst indicated in the blue region in Figure 3.1(left). The closeup of the light curve is shown in Figure 3.2 (left). These observations successfully covered the decay phase of the outburst. The arrows indicate the Suzaku pointings.

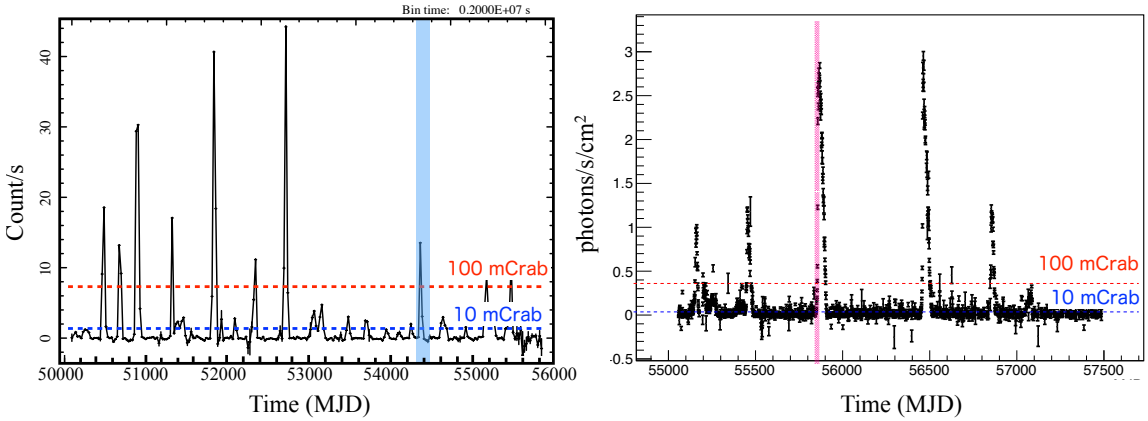

Figure 3.1: The X-ray light curve of Aql X-1 with (left) the ASM/RXTE was obtained in the energy range of 1.3–12.1 keV, and (right) with *MAXI* in the range of 2–20 keV. The vertical blue (left) and magenta (right) stripes indicate *Suzaku*'s observations. The red and blue dashed lines show the flux (unit of the Crab flux) corresponding to 100 mCrab and 10 mCrab.

The 1st, 2nd,..., and 7th observations were performed on September 28 15:35:03, October 3 23:49:36, October 9 05:04:11, October 15 08:09:00, October 19 09:12:43, October 24 23:34:40, and October 30 06:35:01, respectively. We define the 1st, 2nd,..., and 7th observations as Obs. D1, D2,..., and D7. These data were analyzed by Sakurai et al. (2012, 2014).

As shown in Figure 3.3, the spectral shapes gradually changed as the luminosity decreased. This is the state transition described in §2.2.3. The luminosity changed from $\sim 0.1 L_{\rm Edd}$ to $10^{-4} L_{\rm Edd}$ ($L_{\rm Edd} = 2 \times 10^{38}$). Obs. D1 was in the typical soft state, which corresponds to the luminous phase of the outburst. The best-fit spectra are shown in Figure 3.4 (top panel). Because the blackbody radius of the seed photon was less than 10 km (= typical neutron star radius), the matter may have accreted onto the equatorial region of the neutron star's surface. Obs. D2–D4 were in the luminous hard state and have similar spectral shape and luminosity. The best-fit spectra are shown in Figure 3.4 (middle panels). According to the normalization of the disk component, the inner-edge radius of the accretion disk truncated far from the surface ($r_{\rm in} \sim 20-30$ km). Because the blackbody radius of the seed photon increased (~ 10 km), the corona engulfed the neutron star spherically. The best-fit spectra of the dim, hard state are shown in Figure 3.4 (bottom panels). After Obs. D5, the X-rays from the source became dimmer. In Obs. D6 and

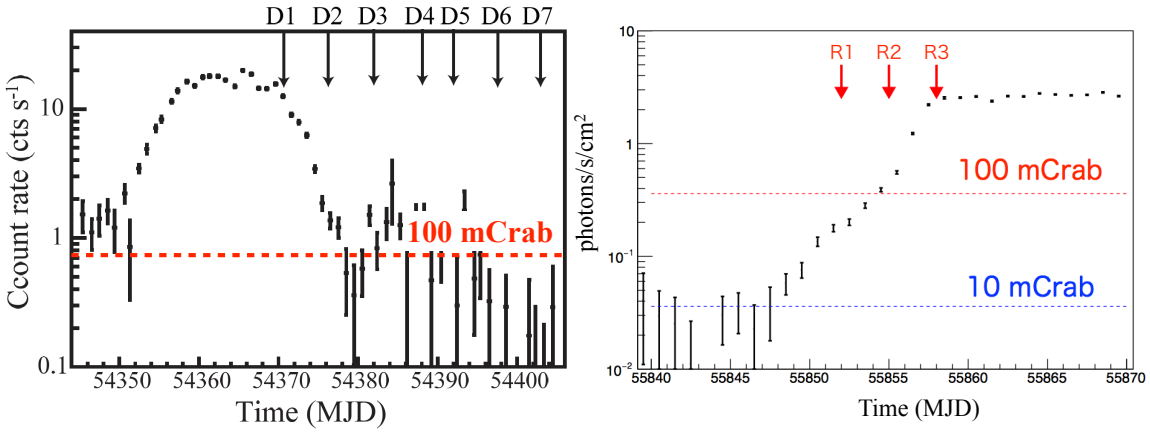

Figure 3.2: (left) X-ray light curve of Aql X-1 obtained with the *RXTE* ASM in and energy range of 1.3–12.1 keV (taken from Sakurai 2015), and (right) with *MAXI* in 2–20 keV. Vertical arrows indicate *Suzaku* observations. Red and blue dashed lines are same as in Figure 3.1.

D7, mass accretion rate was low; the Alfven radius became larger than the neutron star's radius. Thus, the accreted matter is considered to have fallen along the magnetic field. Because the matter eventually falls onto the magnetic dipoles, the blackbody radius of the seed photon became smaller than the neutron star's radius. One of the most important results of their analysis is that the all spectra could be represented by same components that have the multicolor disk emissions and Comptonized emissions.

3.2.2 Rising phase of outburst in 2011

The 2011 data observed the large outburst, indicated by the magenta meshed region in Figure 3.1 (right). The zoomed light curve is shown in Figure 3.2 (right). The arrows indicate Suzaku's observations, and the dates of the 1st (Obs. R1), 2nd (Obs. R2), and 3rd (Obs. R3) observations are October 18, October 21, and October 24, respectively. These observations were performed in three pointings in the rising phase of the outburst. Especially in the 2nd observation, a rare transition was captured, which lasted for ~ 80 ks as shown in Figure 3.5. Nine Type-I bursts occurred in this observation (arrows in Figure 3.5).

νF_ν spectra are shown in Figure 3.6. Obs. R1 and Obs. R2 (before transition) are in the luminous hard state, which are approximately one order of magnitude brighter than the hard state in the 2007 data (Obs. D2–D4). Obs. R2 (after transition) and Obs.

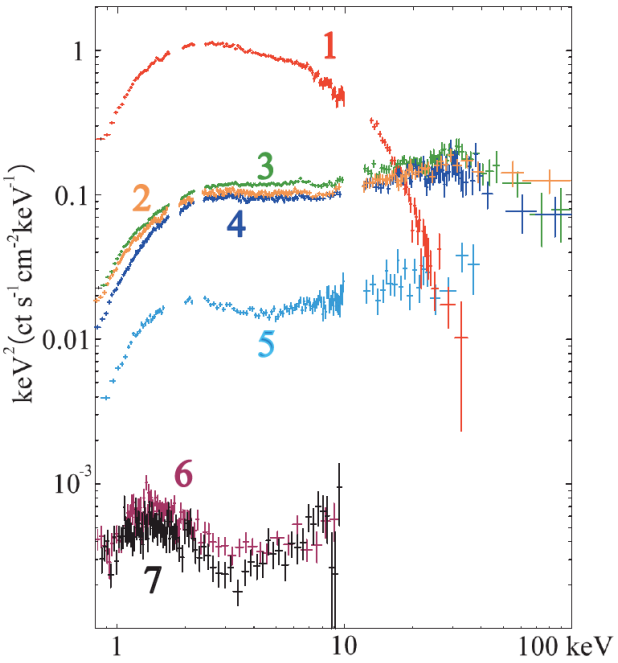

Figure 3.3: Background-subtracted and response-removed νF_ν spectra of Aql X-1, obtained in 2007 in the seven pointings; Obs. D1 (red), Obs. D2 (orange), Obs. D3 (green), Obs. D4 (dark blue), Obs. D5 (light blue), Obs. D6 (purple), and Obs. D7 (black) (taken from Sakurai et al. 2014.

R3 were in the soft state, and were also brighter than the 2007 data. Ono et al. (2017) analyzed the second dataset divided into several epochs to study the spectral parameter changes through the transition. The best-fit spectra and fit residuals are shown in Figure 3.7. According to their analysis, all spectra were represented by the typical emission model of NS-LMXB as well as the model Sakurai et al. (2012, 2014) had reported. Fit parameters changed almost continuously across these epochs. They further discussed the geometry changes in the corona. Using the obtained parameters of the coronal optical depth, which is determined by the slope of the Comptonized component, they revealed that the Comptonizing corona had shrunk in the radial direction as the hard-to-soft state transition. Moreover, they found that this transition may be related to a vertical flattening of the corona or a decrease in the radial velocity of the accretion flow in the corona, or both.

3.2.3 An enigmatic hump on Suzaku spectra in hard state

Although the spectra in the luminous hard state, Obs. D2–D4 in the 2007 data, were successfully represented by the canonical emission model of NS-LMXB, one puzzling issue still remains— the spectra from Obs. D2, Obs. D3, and Obs. D4 exhibit an excess feature around 30 keV, as observable from Figure 3.4 (middle panels). This feature was noted by Sakurai et al. (2012) who partially attributed it to the reflection signal. However, they did not discuss the details any further as the feature was not very significant. In the present thesis, we focus on this feature, assess its statistical significance, and qualify its properties through model fitting. We attempt to interpret this feature in the context of thermonuclear synthesis on a neutron star's surface.

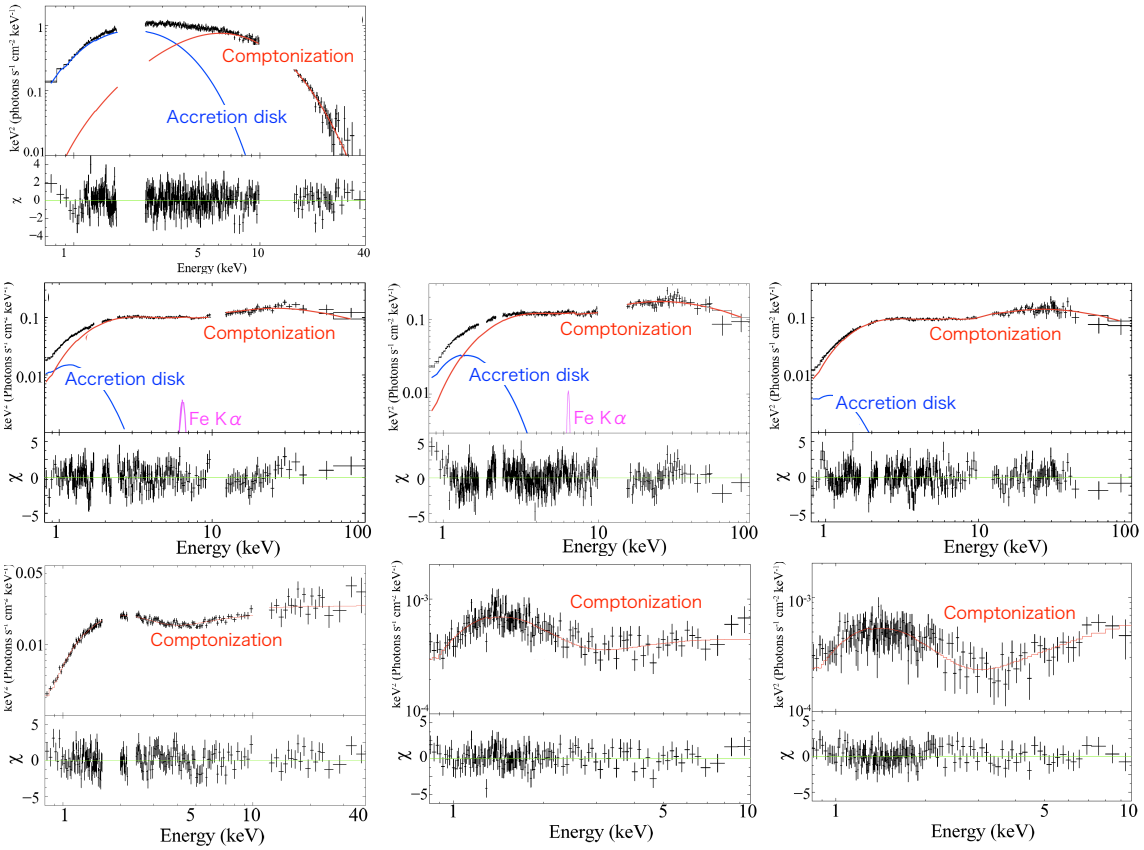

Figure 3.4: Unfolded spectra of 2007 data. The top panel shows Obs. D1 in the Soft state. Middle panels are Obs. D2–Obs. D4 in the luminous hard state. Bottom panels are Obs. D5–Obs. D7 in the dimmed hard state. Red, blue, and magenta solid lines represent the Comptonization components, the disk blackbody components, and the Fe K_α lines, respectively. These figures were taken from (Sakurai, 2015).

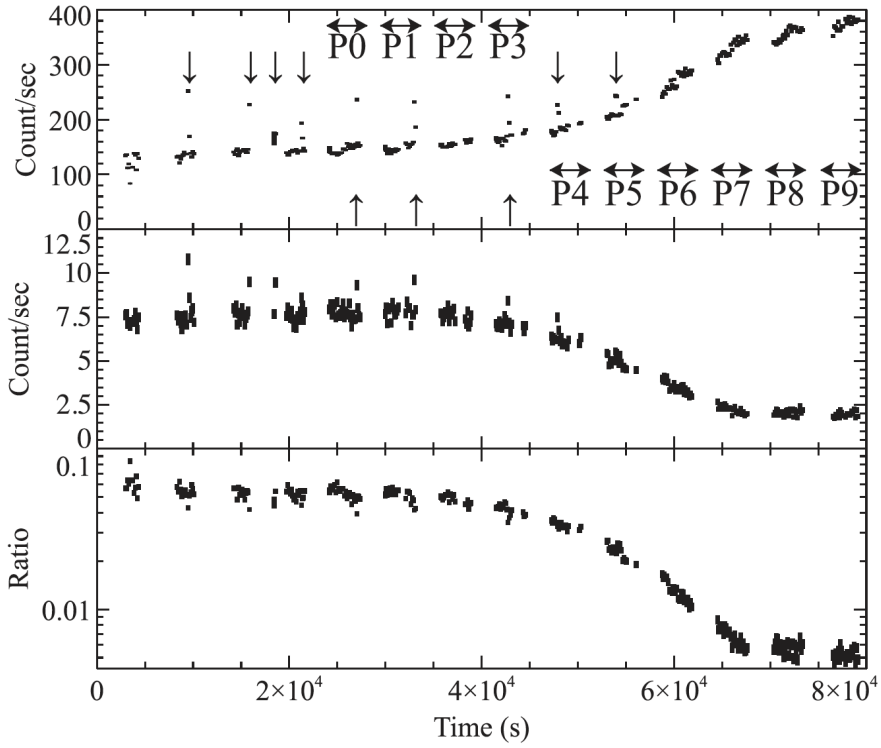

Figure 3.5: *Suzaku* light curve of 2011 data. P0, P1,..., and P9 are the divided epochs given by Ono et al. (2017) (taken from Ono et al. 2017). The arrows indicate Type-I burst events. The top and middle panels show the light curves in the energy range of 0.8–10 keV (XIS) and 15–60 keV (HXD-PIN), respectively. The bottom panel compares the HXD-PIN and XIS hardness ratios.

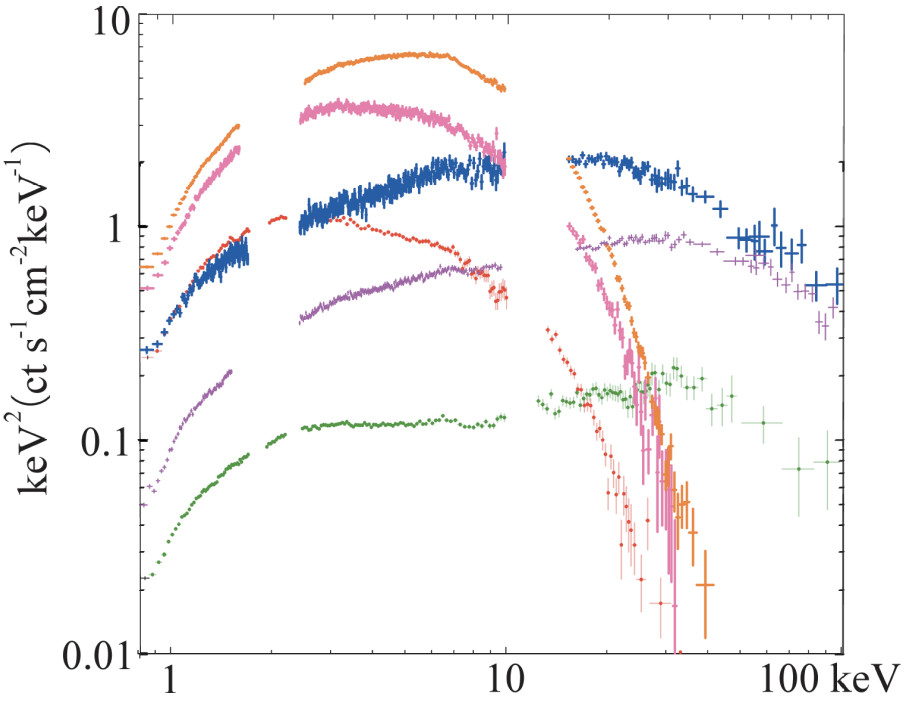

Figure 3.6: νF_ν spectra of the 2011 Suzaku data (taken from Sakurai 2015). Purple, blue, magenta, and orange lines represent the spectra of Obs. R1, Obs. R2 (before transition), Obs. R2 (after transition), and Obs. R3, respectively. Green and red lines represent Obs. D1 and Obs. D3 of the 2007 data for reference.

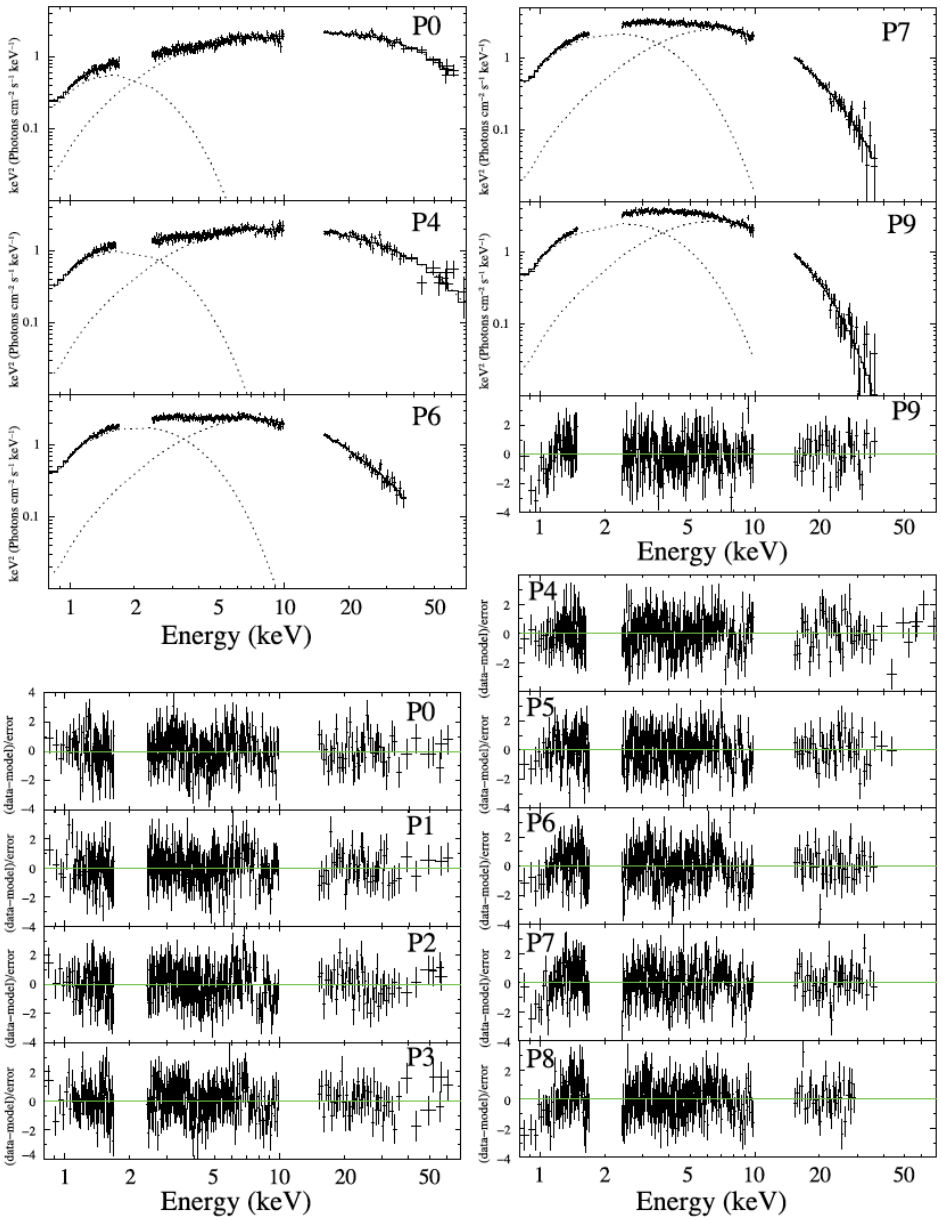

Figure 3.7: Simultaneous fitting of XIS, HXD-PIN, and HXD-GSO spectra of epochs P0, P4, P6, P7, and P9 in νF_ν form. The fit residuals are shown for all ten epochs. This figure was taken from Ono et al. (2017).

Chapter 4

INSTRUMENTATION

4.1 Overview of *Suzaku*

The X-ray Observatory *Suzaku* (Mitsuda et al., 2007) was a Japanese X-ray astronomy satellite, following *Hakucho* (Kondo et al., 1981), *Tenma* (Tanaka et al., 1984), *Ginga* (Makino & ASTRO-C Team, 1987), and *ASCA* (Tanaka et al., 1994). Formerly known as ASTRO-E2, *Suzaku* was a re-challenge mission of the ASTRO-E satellite, which was lost on February 10, 2000 after the failure of its M-V-4 rocket. On July 10, 2005, after a hiatus of 5 years, *Suzaku* was launched successfully by the Japan Aerospace Exploration Agency (JAXA) from the Uchinoura Space Center (USC). As the heaviest (1.7 ton) scientific satellite ever built by Japan at that time, *Suzaku* was a Japanese–US joint mission, developed by the Institute of Space and Astronautical Science at the JAXA in collaboration with the US National Aeronautics and Space Administration (NASA)'s Goddard Space Flight Center, and many domestic and a few US-based institutions.

Suzaku followed a nearly circular orbit at an altitude of 570 km, an inclination angle of 30°, and an orbital period of approximately 96 min. Figure 4.1 shows a schematic view of *Suzaku*. The satellite had a total height of 6.5 m and a weight of 1,680 kg. As summarized in Table 4.1, Suzaku carried onboard three scientific instruments. The first one, called the X-Ray Telescope (XRT; Serlemitsos et al. 2007, Uchiyama et al. 2008), was an X-ray optics system composed of five grazing incidence X-ray telescopes, each focusing 0.2–12 keV X-rays onto its own focal plane. Another one was the X-ray Imaging Spectrometer (XIS; Koyama et al., 2007), consisting of four X-ray CCD cameras. Each camera was installed at the focal plane of the corresponding module of the XRT and measured the position and energy of individual photons. The third one was the

Hard X-ray Detector (HXD; Takahashi et al., 2007), which is a non-imaging detector that measured the energy and precise occurrence time of individual events for energies above $\sim$ 10 keV and up to $\lesssim$ 100 keV. Four sets of XRT+XIS modules as well as the HXD were co-aligned to simultaneously observe the same target. There was another instrument onboard, called the X-Ray Spectrometer (XRS; Kelley et al. 2007), which was placed at the focal plane of the fifth X-ray telescope, measured individual X-ray energy with high accuracy. However, the XRS lost its function due to an unexpected evaporation of liquid helium in approximately a month from the launch, when the observation was about to start.

Although *Suzaku* was continuously pointed towards an observing target, useable data were acquired only for 40–50% of each day because the target was periodically (every 95 min) occulted by the Earth and the spacecraft often passed through regions of high background radiation (e.g., the South Atlantic Anomaly). Typically, individual observations lasted for 0.5 days to a few days. More than 2,700 observations were performed during the mission term of 9 years. Their archive data are available via the DARTS system.

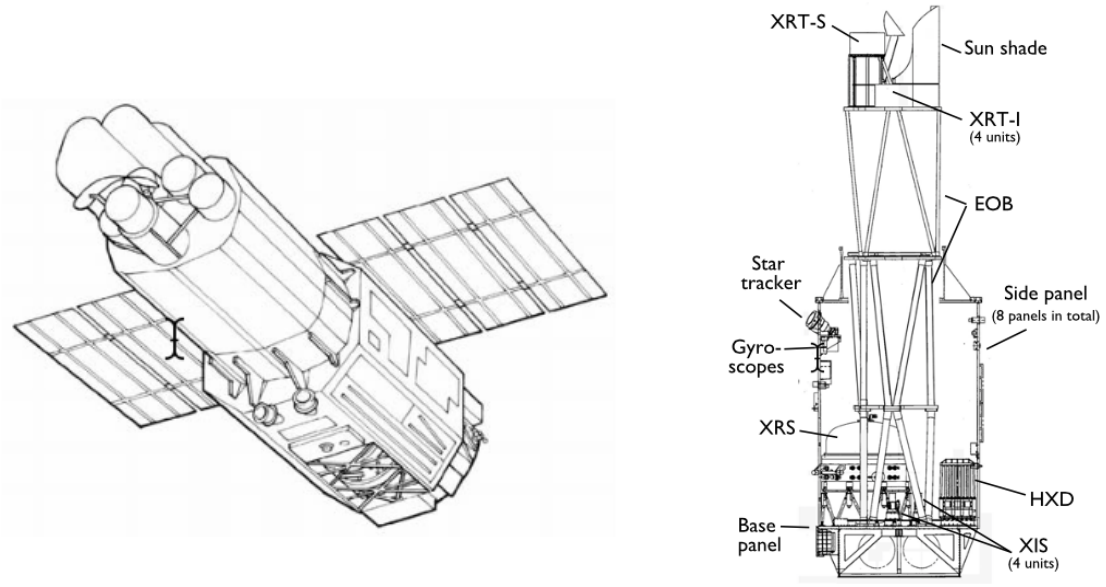

Figure 4.1: Schematic view of the *Suzaku* satellite (left) and its cross-sectional view (right). The figure was taken from Mitsuda et al. (2007).

Table 4.1: Scientific instruments of *Suzaku* (Mitsuda et al., 2007).

XRT	Number of modules	5
	Focal length	4.75 m
	Field of view	$17'$ at 1.5 keV
		$13'$ at 8 keV
	Plate scale	$0.'724$ mm^{-1}
	Effective area	440 cm^2 at 1.5 keV
		250 cm^2 at 8 keV
	Angular resolution	$2'$ (HPD)
XIS	Number of modules	4 (XIS0, 1, 2, and 3)
	Field of view	$17.'8 \times 17.'8$
	Bandpass	0.2–12 keV
	Pixel grid	1024×1024
	Pixel size	24 μm $\times$ 24 μm
	Energy resolution	$\sim$ 130 eV at 6 keV (FWHM)
	Effective area	330 cm^2 (FI), 370 cm^2 (BI) at 1.5 keV
	(incl XRT-I)	160 cm^2 (FI), 110 cm^2 (BI) at 8 keV
	Time resolution	8 s (normal mode), 7.8 ms (P-sum mode)
HXD	Number of modules	1
	Field of view	$4.^\circ5 \times 4.^\circ5 (\leq 100)$ keV
	Field of view	$34' \times 34' (\leq 100)$ keV
	Bandpass	10–600 keV
	–PIN	10–70 keV
	–GSO	40–600 keV
	Energy resolution (PIN)	3.0 keV (FWHM)
	Energy resolution (GSO)	$7.6\sqrt{E_{\rm MeV}}\%$ (FWHM)
	Effective area	$\sim$ 160 cm^2 at 20 keV, $\sim$ 26 cm^2 at 100 keV
	Time resolution	61 μs

4.2 X-Ray Telescope (XRT)

When incident on dense and smooth materials with a shallow grazing angle, X-rays can be totally reflected as the specific dielectric constant of matter at the X-ray frequencies is slightly less than unity. Utilizing this property, grazing incidence X-ray telescopes with focusing/imaging capability had become an essential component in the X-ray Astronomy *Einstein* Observatory launched in 1979. These examples include the five modules of the Suzaku XRT, which employed nested conical metal foils to realize the so-called Wolter Type-O optics configuration. As shown in Figure 4.2, the five XRT modules are mounted on the extensible optical bench (EOB) of the spacecraft. One of them named XRT-S is dedicated to the XRS, while the rest of the modules, named XRT-I0, I1, I2, and I3, respectively, were coupled to four XIS cameras. Major parameters of the XRT-I are summarized in Table 4.1. Each XRT module consists of a reflector, a pre-collimator, and a thermal shield. As photographed in Figure 4.3, the reflector consists of tightly nested reflecting metal foils that have conical shapes with a common axis. The top half of the reflector approximates confocal paraboloids, whereas the bottom half, confocal hyperboloids. An X-ray photon is reflected first by the paraboloid section, and then by the hyperboloid section. This, too, is the Wolter Type-I configuration. Because the reflectors are sensitive to changes in temperature, the thermal shield was introduced to thermally isolate the XRT from space and reflect the infrared radiation from the interior of the spacecraft. To prevent stray light, the pre-collimator was located on top of the primary reflector.

The effective areas of the XRT are shown in Figure 4.4, in comparison with those of the other two X-ray missions, *Chandra* and *XMM Newton*. The effective area of *Suzaku* over whole energy band is slightly lower than that of *XMM-Newton*, but higher than that of *Chandra* in energies above 1 keV. Thus, the effective area decreases rapidly above ~ 8 keV, as a combined effect of decreasing reflectivity of the XRT and loss of the XIS quantum efficiency. A slight decrease at < 1 keV is observed due to photoelectric absorption, XRT ' s thermal shield, and the protective SiO_2 layer in the XIS. The sharp features at 0.28 keV, 0.53 keV, 1.56 keV, and 1.84 keV are due to the K-edges of C, O, Al, and Si, respectively. Of these elements, C and Al are mainly present in the thermal shield, whereas O and Al are mainly present in the XIS. Another feature at 2.3 keV in the M-edge of Au, which is used as coating of the XRT reflector foils. When the XRT+XIS observes a point source, such

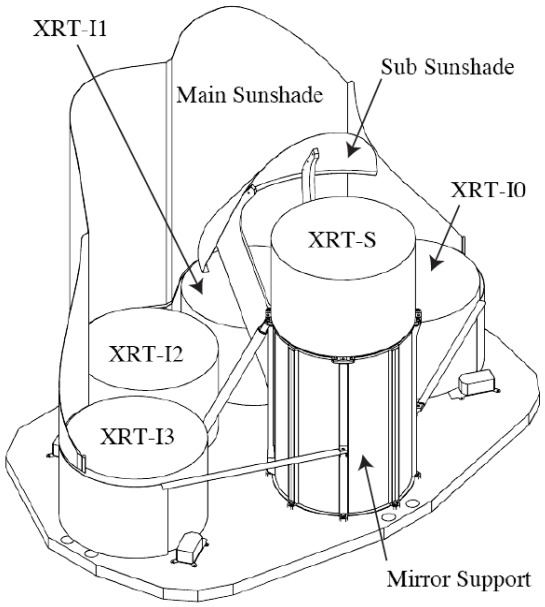

Figure 4.2: Schematic view of the XRT mounted on top of the EOB (from Mitsuda et al. 2007).

as a neutron star or a blackhole, the obtained image suffers from instrumental spreading and can be expressed by the point spread function (PSF) in an integral form called the encircled energy function (EFF). Figure 4.5 shows the images, PSFs, and EEFs of the four XRT-I modules when coupled with the four XIS cameras. Thus, the PSF consists of a sharp core and an extended wing due to X-ray scattering. As a result, the angular resolution of the XRT is relatively high, $< 1'$, in terms of the full width at half maximum (FWHM) of the PSF. However, it worsens to $\sim 2'$ if the half power diameter is employed when the EEF reaches 0.5 (i.e., the diameter containing 50% of all the focused photons). We usually quote the latter as angular resolution of the XRT.

4.3 X-ray Imaging Spectrometer (XIS)

The first observation using an X-ray CCD camera was conducted by *ASCA* SIS. Since then, X-ray CCDs have become principal devices for X-ray astronomy and were adopted for the *Chandra* ACIS and *XMM Newton* EPIC (Turner et al., 2001; Strüder et al., 2001). The XIS camera body consists of a hood, a bonnet, and a base. The hood has five baffles to prevent stray light from entering. The XIS CCDs are sensitive to optical and UV light, and are hence required to have the optical blocking filter (OBF). To reduce thermal

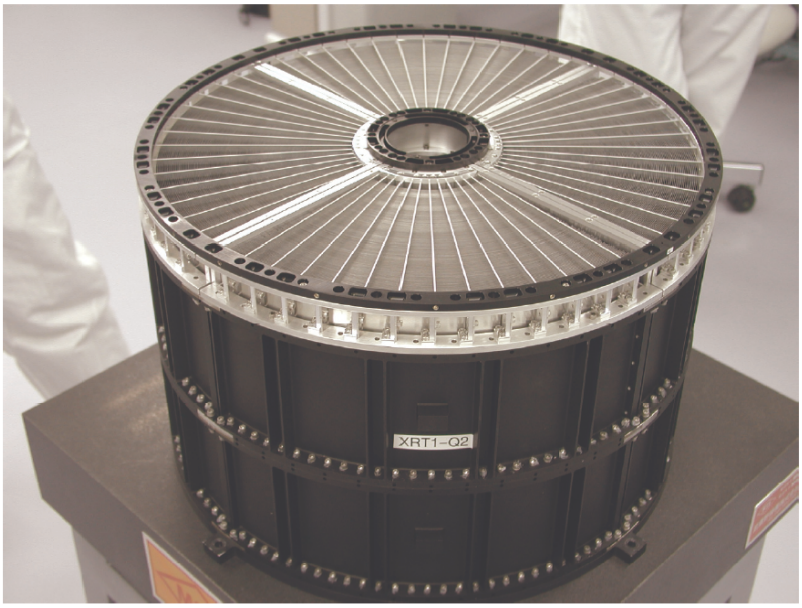

Figure 4.3: Photograph of an XRT-I1 module without the thermal shield (taken from Serlemitsos et al. 2007).

noise, an operation temperature of a CCD must be at a low temperature. Thus, the XIS has a three-stage thermo-electric cooler (TEC) to cool the CCD. The TEC is connected to the CCD, and the heat is dissipated through the heat pipe and sent to the radiation panel on the outside of the spacecraft. Performance of the CCD degrades due to radiation damage by high-energy charged particles. Especially on low-Earth-orbit (LEO) satellites like Suzaku, most of the damage is caused due to the large flux of charged particles in the South Atlantic Anomaly (SAA). The radiation damage increases the dark current and decreases the charge transfer efficiency. To reduce such damage, the XIS sensor is surrounded by a radiation shield.

Figure 4.6 shows a photograph of the XIS camera body (left) and its cross-section (right). The XIS has four sensors, XIS0, XIS1, XIS2, and XIS3, and each sensor consists of four segments, A, B, C, and D, as shown in Figure 4.7. The front side of a CCD is defined as the side with a gate structure. The CCD sensor is characterized into two types: (1) front-illuminated (FI) CCD and (2) back-illuminated (BI) CCD. In the FI-CCDs, incident X-rays come from the front-side of the CCD. XIS0, 2, and 3 belong to this type. In this case, the gate structure acts as a dead layer. The gate structure is made of Si with a thickness of $\sim$0.28 μm and SiO_2 with a thickness of $\sim$0.44 μm. Meanwhile, in a BI-CCD,

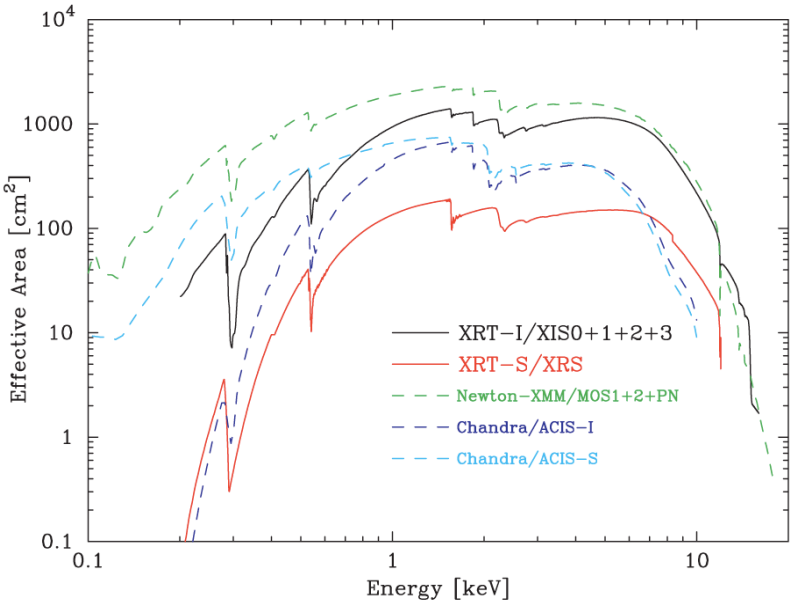

Figure 4.4: Effective areas of the XRT shown as a function of energy, in comparison with those of *XMM-Newton* and *Chandra* (taken from Serlemitsos et al. 2007). The quantum efficiency of XIS is also included.

incident X-rays come from the backside of the CCD. The XIS1 is classified into this type. The BI-CCD has a thin dead layer, 5 nm HfO2, 1 nm Ag, and 3 nm SiO2. Because the FI-CCD suffers from additional photo-absorption, the FI-CCD's sensitivity for low-energy X-rays is lower than that of the BI-CCD. The thickness of a depletion layer of FI-CCD and BI-CCD are ∼65 μm and ∼42 μm, respectively. As shown in Figure 4.8, the quantum efficiency for high-energy X-rays of an FI-CCD is better than that of a BI-CCD.

4.3.1 Data processing mode

Clocking mode

The Suzaku satellite is preparing several observation modes and options. For example, clocking mode has a normal mode and P-sum mode. A burst option and a window option are available in the normal mode. In a normal mode with no option, signals from all CCD pixels are readout every 8 s, and 1024×1024 pixel data are generated. Whereas in the burst option, any arbitrary exposure within 8 s can be selected to generate a full-sized image. This option is used for a bright, extended source to prevent photon pileup. In the window option, signals from only a part of the CCD active image are readout. Pixel ranges

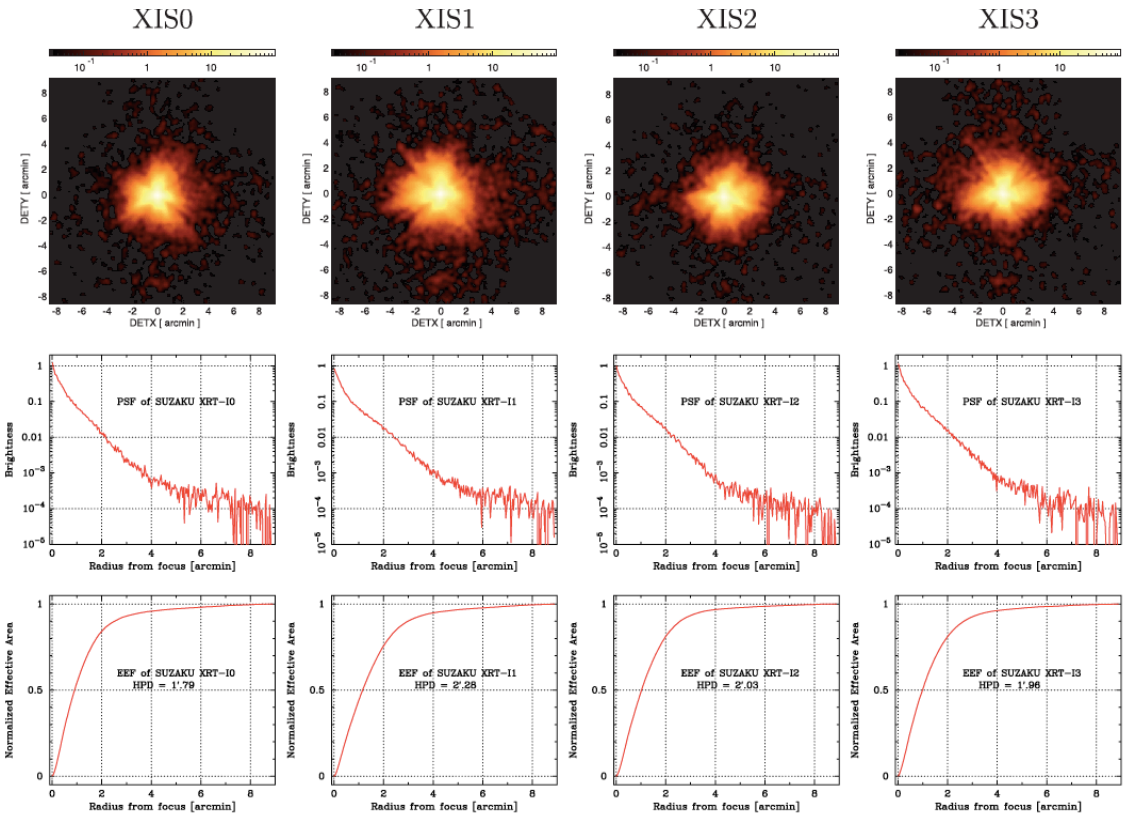

Figure 4.5: Images (top panels), point spread function (middle panels), and encircled energy function (bottom panels) of XRT-I. From left to right, results on XRT-I0+XIS0, XRT-I1+XIS1, XRT-I2+XIS2, and XRT-I3+XIS3 are presented in columns. This figure was taken from Serlemitsos et al. (2007).

of 256, 128, and 64 along the ActY direction were readout, and are called 1/4, 1/8, and 1/16 windows, respectively. The exposure depends on the window size, 2 s, 1 s, and 0.5 s for the 1/4, 1/8, and 1/16 windows, respectively. This option is used for a bright point source. The XIS data analyzed in this thesis were taken with the 1/4 window option.

In the P-sum mode, several rows (64, 128, or 256 rows) are summed up from the bottom of the CCD image to generate one-dimensional data. The data path is through a flame-store region and fed into a readout node. Data processing is performed at individual rows. Because the processed data constitutes one-dimensional information only, this option is tolerant of the photon pileup and achieves a good time resolution.

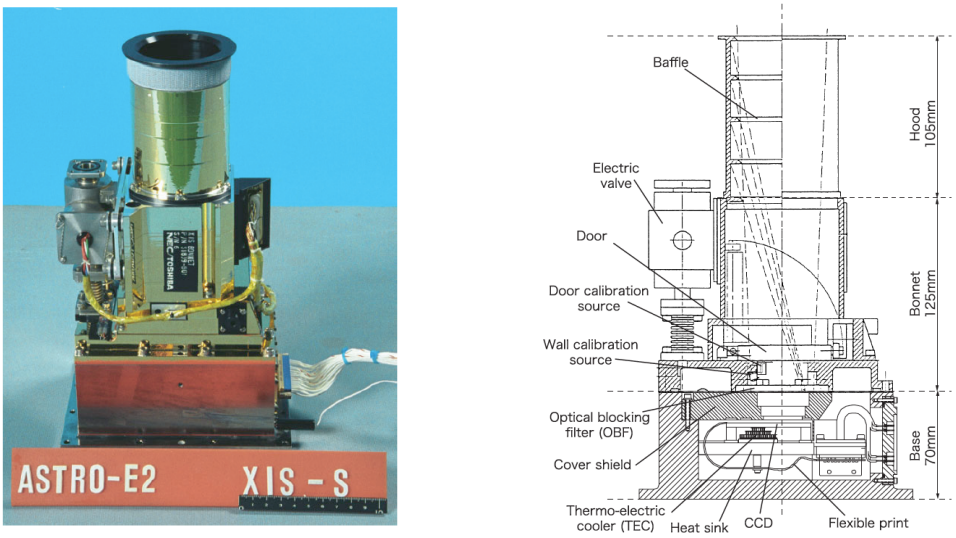

Figure 4.6: XIS camera body (left) and its cross-section (right) (Mitsuda et al. 2007).

4.3.2 Photon pileup

The XIS is a position-sensitive integrating instrument with a normal interval of 8 s between signal readouts. When more than one photon hits the same CCD pixel or one of its immediate neighbors, the CCD cannot correctly measure the energy of the incident photons. This phenomenon is called photon pileup. The pileup effect could be a significant problem when observing a bright point source, and could cause distortions in the image and spectrum. If several photons strike the same pixel at the same time, the CCD detects multiple signals as one large signal; the energy spectrum becomes harder. If the several photons hit one pixel, the generated charges pour into the neighbor pixels, distorting the image. To prevent photon pileup, Suzaku prepared some observational options as describe above (§4.3.1). Yamada et al. (2012) performed a comprehensive study of the pileup phenomenon at the XIS by measuring some bright X-ray sources.

4.4 Hard X-ray Detector (HXD)

4.4.1 The system design

The HXD is a non-imaging, collimated instrument developed jointly by the University of Tokyo, ISAS/JAXA, RIKRN, and many other institutes. The total mass of the HXD exceeds 200 kg, which makes it by far the heaviest cosmic X-ray experiment ever built in Japan. Nevertheless, the overall power consumption of the HXD is extremely low, approximately 40 W, as required for a space-based experiment. The HXD consists of the

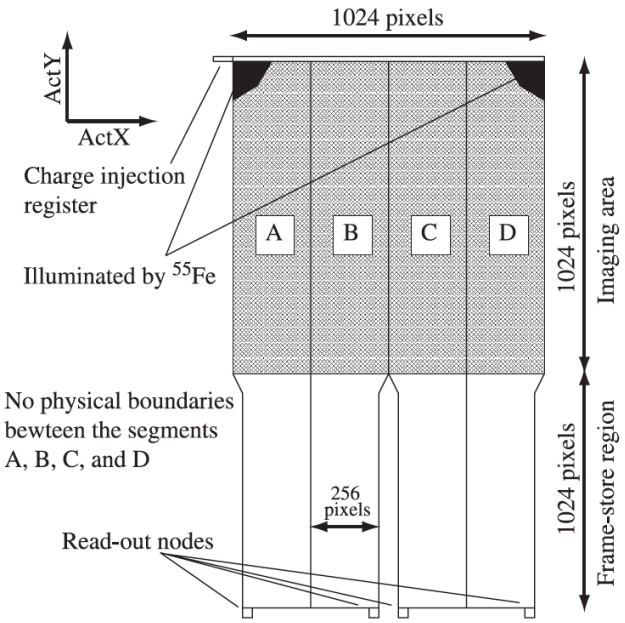

Figure 4.7: XIS sensor part. (Mitsuda et al. 2007).

sensor part HXD-S, the analog electronics part HXD-AE, and the digital electronics part HXD-DE. X-rays from celestial objects are detected by HXD-S, and the generated analog signal pulses are transmitted to HXD-AE in 116 parallel chains. Receiving these signals, HXD-AE performs an analog-to-digital conversion to obtain pulse heights of individual photons. In addition, HXD-AE supplies power to pre-amplifiers and high-voltage power supplies attached to HXD-S. HXD-DE is a CPU-based signal processing unit that uses a pair of 80C836 CPUs (for redundancy) at an extremely low clock speed of 12 MHz to suppress the power consumption. It receives digitized data from HXD-AE, compress them, performs further screening, and edits the results into telemetry packages. In addition, HXD-DE receives commands from the spacecraft Command Decoder, and interprets them.

4.4.2 HXD-S

Configuration

Figure 4.9 shows a picture of HXD-S, and Figure 4.10 illustrates the same. HXD-S consists of the main detector part, anti-coincidence shielding part, radiation cooling part, and a mechanical housing. Because the HXD observes in a high-energy range, above 10 keV, where background signals become progressively dominant, HXD-S has been designed to achieve the highest sensitivity by suppressing the background to an extremely low level of $\sim 10^{-4}$ cts s^{-1}cm^{-2}keV^{-1}.

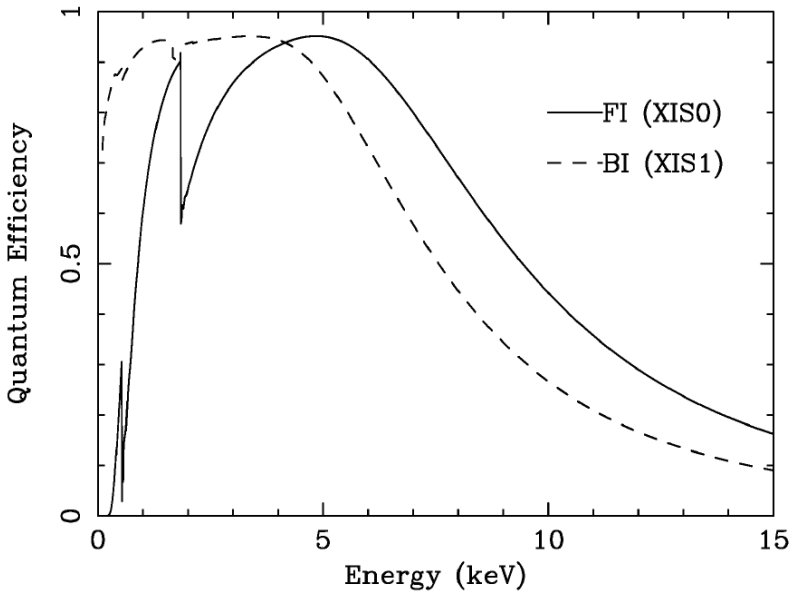

Figure 4.8: Quantum efficiencies of FI-CCD and BI-CCD (Mitsuda et al. 2007).

Well counter units

As shown in Figure 4.10, the main detector part of HXD-S consists of 16 well-type counters (well counter units), instead of a single detector with a large area. This compound-eye configuration has several advantages. One is that technical risks that come with fabricating a single, large detector can be avoided. Another is that heavy dead times due to high counting rates can be avoided by making individual detectors rather small, and processing their signals in parallel. In addition, background can be reduced by taking mutual anti-coincidences among different well-type detectors.

A well counter unit is illustrated in Figure 4.11. It weighs 4.63 kg and consists of crystal scintillators, a photo-multiplier tube (PMT), four Silicon PIN diodes (HXD-PIN), a fine collimator, and front-end electronics. The largest component is the crystal scintillators, which are further divided into three parts—a well-shaped BGO ($Bi_4Ge_3O_{12}$) section called the BGO top piece, a BGO block section (BGO bottom piece), and four GSO (Gd_2SiO_5) scintillators, each $24 \times 24 \times 5$ mm^3 in size. The BGO top piece provides coarse collimation, the BGO bottom piece is used for anti-coincidence, and the GSO scintillators serve as the main detector part above $\sim$ 50 keV (HXD-GSO). The scintillation lights from these scintillators are all read by a common PMT produced by Hamamatsu Photonics. The

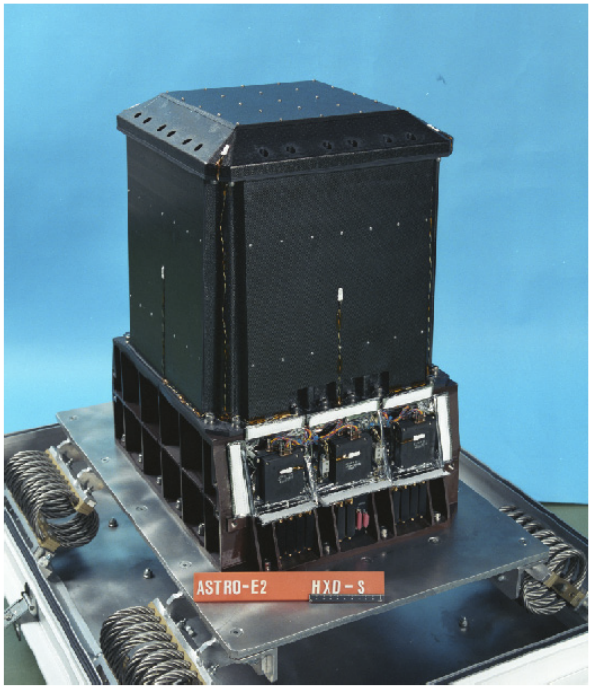

Figure 4.9: Photograph of HXD-S (Takahashi et al., 2007).

individual analog signal pulses produced from the PMT are first processed by the front-end electronics and then fed into HXD-AE where pulse-shape discrimination distinguishes the GSO and BGO events (see below).

Silicon PIN diodes

Although the crystal scintillators used in the well counter units have high stopping power for hard X-rays, their sensitivity is limited to energies above $\sim$ 50 keV. To lower the detection threshold to $\sim$ 10 keV, below which the XIS starts working, four 2-mm-thick silicon PIN diodes are placed in front of the GSO scintillators. Lower-energy (typically 10–50 keV) photons from celestial objects are detected photon-by-photon by these PIN diodes, whereas more energetic ones pass through the PIN diodes and are detected by the GSO crystals. By placing one type of radiation detector on top of another is the best configuration for the optimal use of the limited volume as a satellite payload instrument. The signals from each PIN diode are read out by its own low-noise pre-amplifier, and are sent to HXD-AE like the PMT outputs.

The four PIN diodes, which are placed inside the deep well of BGO, are tightly shielded from non-celestial radiation as well. Nevertheless, the signal aperture defined by the BGO top piece (§4.4.3) is still too wide for the PIN diodes because many neighboring celestial

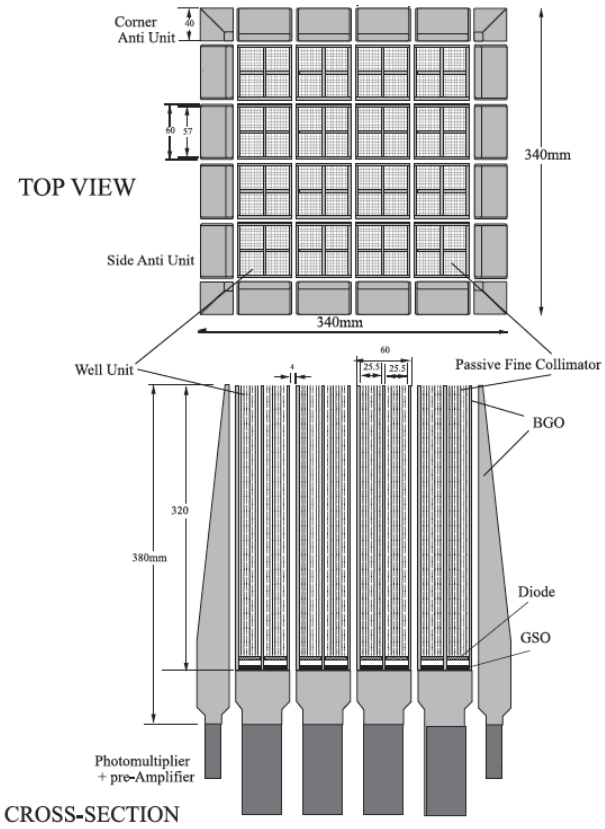

Figure 4.10: Drawing of HXD-S (Takahashi et al., 2007). The top and bottom panels show its top view and a cross-sectional view, respectively.

sources could contaminate data in these energy ranges. Therefore, a fine collimator made of phosphor–bronze pipes is inserted into the BGO top piece to further reduce the aperture (see §4.4.3).

The energy resolution and low threshold of HXD-PIN are determined by a competition between the signal pulse heights and the electrical noise in the pre-amplifiers. When the diodes are cooled, the leakage current and electrical decrease rapidly. Therefore, HXD-S as a whole is radiatively cooled in orbit to $\sim -20^{\circ}$ by a combined use of a pair of radiator panels and heat pipes.

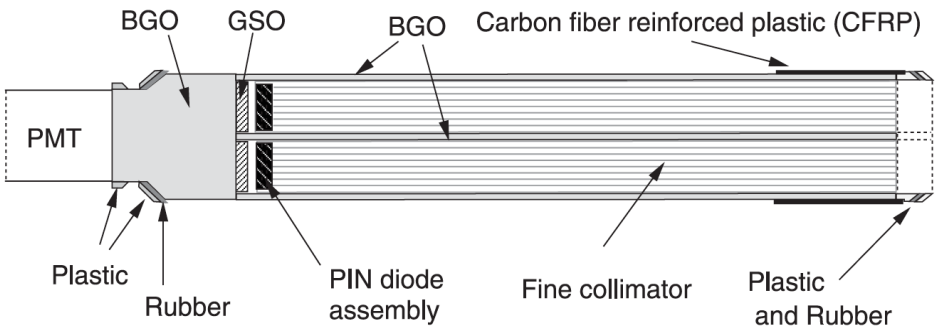

Figure 4.11: Detailed view of one HXD well counter unit (Takahashi et al., 2007).

Background rejection via " phoswich" technique

The output data from HXD are simply a list of photons, each tagged with a detector ID (the well-unit number from 0 to 15), an ID specifying either PIN or GSO, two pulse heights (see below), the arrival time, and some auxiliary information such as presence/absence of simultaneous hits in the other well units and/or the surrounding anti-counters (explained later). These events arrive from not only the celestial targets being observed through the aperture but also various background sources, as summarized in Table 4.2. Because HXD is a non-imaging instrument, we cannot generally state which of the detected events are genuine celestial signals and which originate from the background. Therefore, it is vital for HXDs to reduce the background noise.

The method to read two different types of scintillators (BGO and GSO) by a common PMT is called the" phoswich" (phosphor sandwich) method. By reading both scintillators with a single PMT instead of two, the instrument can be made lighter, smaller, and low power consuming. Although this technique has a long history, the long well-type BGO top piece was for the first time introduced in a balloon experiment (e.g., Takahashi et al. 1993), which later developed into HXD.

Here, we explain the phoswich configuration in detail. The BGO top and bottom pieces together provide a passive shield for the main detectors (HXD-GSO and HXD-PIN). However, because of the severe weight limitations of conducting a space experiment, the BGO shield cannot be made thick enough to completely stop incoming gamma-rays. Instead, it is just thick enough, in the 4π directions, to afford a Compton optical depth

of approximately unity (~ 3 g cm^{-2}). Therefore, the gamma-rays incident from sideways would give Compton-hit signals in the BGO, even if they penetrated BGO and eventually arrive at one of the four GSO crystals. From such an event, which must be rejected, the PMT will receive a mixed light output from the two crystals. Such an event will have a relatively long, light-decay profile, because light pulses from the BGO have a decay constant of ~ 700 ns, which is much longer than that of the GSO signals, which is ~ 120 ns. In contrast, a genuine celestial X-ray event would have a short GSO decay profile characteristic. Thus, although a pulse-shape analysis is conducted in HXD-AE, "GSO-like" events can be distinguished from‘‘ BGO-like" events (more rigorously, "BGO+GSO-like") ones. If an event is clearly BGO-like, it is discarded onboard, whereas GSO-like events, as well as those in the gray zones, are transmitted to the ground control for further examination (§4.4.4).

In HXD-AE, the pulse-shape analysis, or pulse-shape discrimination (PSD), is performed using an analog application specific integrated circuit (ASIC) developed for the HXD. In this ASIC, an analog pulse from a PMT is split into two charge integration chains, one having a time constant of 150 ns (called Fast shaper) and the other, 1 μs (Slow shaper). Thus, each event yields two pulse heights (PHs), called Fast PH and Slow PH. Figure 4.12 (a) is an example of plots called "Fast–Slow diagram," where each incoming event is plotted by a dot on the plane of Fast PH vs. Slow PH. These particular data were obtained by irradiating a well unit with ^{22}Na, which emits 511 keV and 1,275 keV gamma-ray lines. There, the BGO-detected events form a branch with a steeper slope, because longer-decay BGO light pulses can be fully integrated by the Slow shaper, but only partially by the Fast shaper. This means that Fast PH $<$ Slow PH. In contrast, the signals from a GSO can be integrated similarly by both chains (Slow PH = Fast PH), so that they could form a branch with a milder slope. Another branch is seen connecting the 511 keV photo-peaks of GSO and BGO; it consists of events that are scattered in one scintillator and absorbed by the other. By selecting events inside a region called the "selected region," we can extract only those events that had an energy deposit only in the GSO. Figure 4.12 (b) shows the result of this PSD application.

Antic-coincidence shielding part

In the 4×4 matrix formed by the 16 well counters, four innermost units are tightly surrounded by 12 outer units, but the outer ones are not. Therefore, for additional shield-

Table 4.2: Major components of the HXD background and their origins.

Major and Minor classifications		Origin
Particles	Charged particles	Primary cosmic rays (mainly energetic protons)
		Secondary cosmic rays (protons, electrons, muons)
	Neutrons	Produced in the atmosphere by cosmic rays
Gamma-rays	Cosmic X-ray background (CXB)	Numerous unresolved active galactic nuclei
	Atmospheric gamma-rays	Created in the atmosphere by cosmic rays
	Internal backgrounds	Natural radioisotopes in the detector materials
		In-orbit radio-activation of the detector materials

ing of the outer well counter units, 20 anti-coincidence counter units (or anti-counters) surround the well counter matrix. Each Anti-counter is a 2.6 cm-thick BGO pillar weighing 4.12 kg, except the four corner units that weigh 2.72 kg each. They have a wedge-like shape to save the weight while yielding the same path length through the BGO, as viewed from the PIN and GSO detectors. An anti-unit (except the corner ones) has a geometrical area of 800 cm^2 and an effective area of 400 cm^2 for 1-MeV gamma-rays. The anti-counters provide a powerful, active anti-coincidence shield against charged particles impinging sideways, and background gamma-rays that would Compton-scatter one of the main detectors and escape if there were no anti-counters.

4.4.3 Performance of the HXD

Figure 4.13 shows the effective areas of HXD-PIN and HXD-GSO as a function of energy—that of PIN and GSO at 20 keV and 100 keV are 160 cm^2 and 260 cm^2, respectively. The PIN effective area decreases below $\sim$ 12 keV as the thermal noise begins to dominate and gradually increases beyond $\sim$ 30 keV due to a decrease in the stopping power. The sharp drop in the GSO 's effective area below 40 keV range is due to absorption by the PIN diodes placed in front. Thus, the nominal energy ranges of HXD-PIN and HXD-GSO are 10–70 keV and 40–600 keV, respectively. The energy resolution of PIN and GSO are 3.0 keV (FWHM) and $7.6\sqrt{E_{\rm MeV}}\%$ (FWHM), respectively. HXD has a high time resolution of 61 μs, which is much higher than that of the XIS (2 s or 8 s).

The field of view (FOV) of the well units is collimated to $4^\circ.5 \times 4^\circ.5$ (FWHM) by their

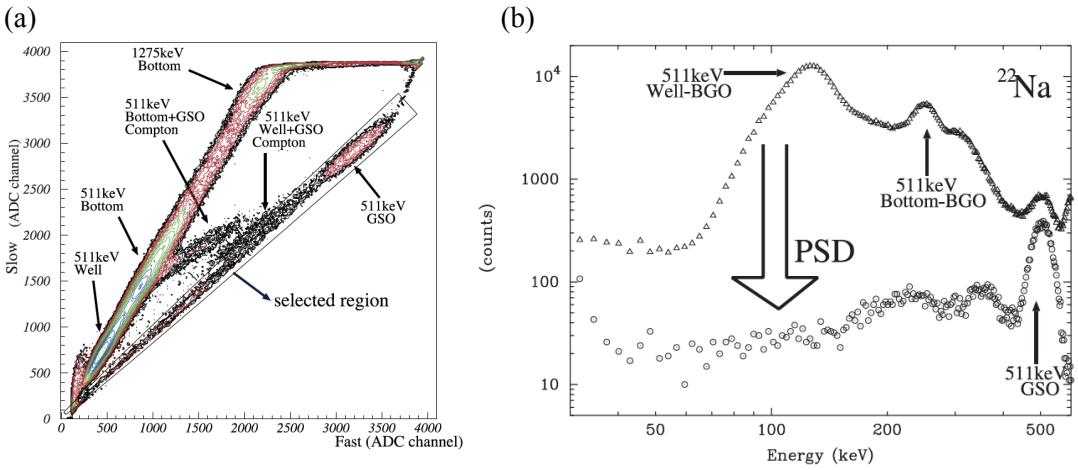

Figure 4.12: (a) A Fast–Slow diagram using PMT signals from one well counter, obtained on ground by illuminating a ^{22}Na source. Several branches are indicated. (b) The pulse-height spectra derived from the left panel, shown before and after applying the PSD (Kokubun et al., 2007).

BGO top piece. Furthermore, the fine passive collimator described above limits the FOV to $34' \times 34'$ f (FWHM). However, this narrower FOV is available only in energies below $\sim$ 100 keV because the fine collimators become transparent for higher energy photons. Therefore, HXD-PIN and HXD-GSO observe an X-ray sky through an FOV of $34' \times 34'$ and $4^\circ.5 \times 4^\circ.5$, respectively.

After the launch of *Suzaku* on July 10, 2005, the HXD's start-up operation began on July 22 and continued till August 19 when it became fully operational and acquired its "first light." Since then, till the end of *Suzaku*'s operation in August 2015, the HXD kept working normally and its in-orbit performance was (almost) as designed. Its low-background design in particular was successfully verified in orbit, as explained in the next subsection. However, one of the two heat pipes had failed (for unknown reasons) immediately after the launch. As a result, the temperature of HXD-S was, sometimes, higher (e.g., -15°) than anticipated. Therefore, the lower threshold of HX-PIN became $\sim$ 12 keV rather than the design value of 10 keV.

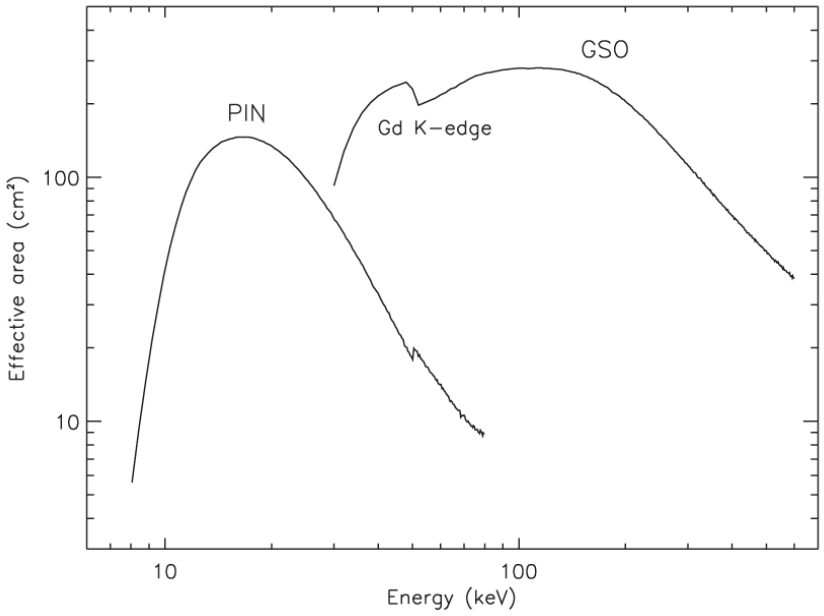

Figure 4.13: Effective areas of HXD-PIN and HXD-GSO (Takahashi et al., 2007).

4.4.4 Background subtraction

Background rejection in on-ground analysis

In the present thesis, we analyze a spectral feature in the HXD data. Therefore, its background property is important. This problem can be analyzed from two questions, namely how to *reject* backgrounds through post-observation data analysis (or data screening) and how to *subtract* the residual background from the obtained celestial data. With reference to Kokubun et al. (2007), we review these issues in this and subsequent sections.

As described in §4.4.2, the onboard background rejection using PSD is carried out only coarsely. On the one hand, the role of background rejection is to reduce the rate of data to be transmitted to ground. On the other hand, it should enable more sophisticated and optimized background rejections to be conducted in the post-observation data analyses. Towards the latter goal, the HXD team analyzed the actual in-orbit data and arrived at the optimal ‘‘ cut ’’ on a Fast–Slow diagram. They also found the best anti-coincidence conditions among the 116 signal chains (Kokubun et al., 2007); 16×2 (Fast and Slow) from HXD-GSO, 64 (4 times the 16 well units) from HXS-PIN, and 20 from the anti-counters. Usually, these optimum cuts are applied to the HXD data before being made publicly available; therefore, users need not perform these complicated data screening by themselves.

As shown in Figure 6.10, these rejection steps worked successfully, both in HXD-PIN and HXD-GSO,; thus, it can be concluded that the final background level was closer to what was anticipated.

Modeling, prediction, and subtraction of the HXD background

Although the HXD achieved the expected low background level, the final data still contain residual background events that can no longer be distinguished from true celestial X-rays. Among the various background components listed in Table 4.2, those dominating the residual background are natural radioactive isotopes in the detector materials, radioisotopes produced when the spacecraft passes through the SAA (§ 4.3), and atmospheric neutrons. These neutrons easily pass through the BGO shield and induce a recoil signal in the HXD-PIN (Kitaguchi, 2009). Because the HXD has neither imaging capability nor an ‘‘ offset detector ’’ that points to a source-free region in the sky, the instantaneous background must be estimated, or modeled, and subtracted from the accumulated on-source data. The ultimate sensitivity of HXD is often limited by its reproducibility or systematic errors of this background subtraction.

In subtracting the HXD background, the biggest difficulty is that the atmospheric neutrons and the SAA-induced radio activation signals vary significantly, as presented in Figure 4.15. There, the background intensity in HXD-PIN (left panel) varies periodically by a factor of two, in anti-correlation with the geomagnetic cutoff rigidity (COR) at the position of the spacecraft. In regions with low COR, which is mostly at high latitudes, numerous softer primary cosmic rays can enter the atmosphere and produce more neutrons. Similarly, the HXD-GSO background rate (right panel) decreases as a function of time $t_{\rm SAA}$ after the spacecraft exits the SAA; during the SAA passages, significant amounts of radio isotopes are generated inside the detector, which decay with various time constants.

The HXD team constructed two reliable methods for predicting the HXD background (Fukazawa et al., 2009). Both methods start by accumulating a large volume of HXD data taken when the target objects are behind the Earth, and then sorting them into a database for non-X-ray background (NXB), where “non X-ray” means that the cosmic X-ray background (CXB) is occulted by the Earth and is hence absent. Then, in one method (called “quick”), the spectra in the database are sorted according to the COR and $t_{\rm SAA}$, which are then superposed in a way appropriate for the analysis of the actual observation. Therefore, the background events in this case are actually the ones in the database. The

other method (called "tuned") derives long-term (e.g., a month) NXB light curves using the database, in a certain number of energy bins. These light curves are then fitted with an empirical function, which includes a fair number of parameters such as the COR and $t_{\rm SAA}$. Once these parameters are determined, the function can be used to predict the expected count rate at a given time of observation for a given energy band. Finally, "fake" HXD events are produced by a Monte-Carlo method, to reproduce the count rates predicted by the best-fit model. The confirmed reproducibility of these methods is listed in Table 4.3 for several observation conditions. Thus, the second method wherein the 1σ systematic error of the NXB modeling is less than $\sim 3\%$ for HXD-PIN in 15–40 keV is considered more accurate (and 1% for HXD-GSO in 50–100 keV though not shown in the table).

The CXB, which is from numerous active galactic nuclei (accreting massive black holes) at various redshifts), is not modeled by the above method. The CXB is estimated in a separate way and subtracted, which is rather easy because it is independent of the sky direction and the time of observation.

Table 4.3: Standard deviation (1σ) of residuals between the PIN Earth data and model (Fukazawa et al. 2009).

15–40 keV	10 ksec		20 ksec		40 ksec	
	quick	tuned	quick	tuned	quick	tuned
Standard deviation (σ)	3.75%	2.31%	3.23%	1.72%	2.96%	0.99%
Statistical error ($\sigma_{\rm stat}$)	1.83%		1.36%		0.93%	
Systematic error ($\sigma_{\rm sys}$)	3.27%	1.40%	2.93%	1.05%	2.81%	0.34%
40–70 keV	10 ksec		20 ksec		40 ksec	
	quick	tuned	quick	tuned	quick	tuned
Standard deviation (σ)	5.53%	4.92%	4.34%	3.51%	3.39%	2.87%
Statistical error ($\sigma_{\rm stat}$)	4.03%		3.01%		2.03%	
Systematic error ($\sigma_{\rm sys}$)	3.78%	2.82%	3.12%	1.81%	2.71%	2.02%

4.5 NuSTAR Observatory

The nuclear spectroscopic telescope array (NuSTAR; Harrison et al. 2010) was launched onboard the Pegasus XL rocket from Kwajalein Atoll on June 13, 2012. NuSTAR follows a

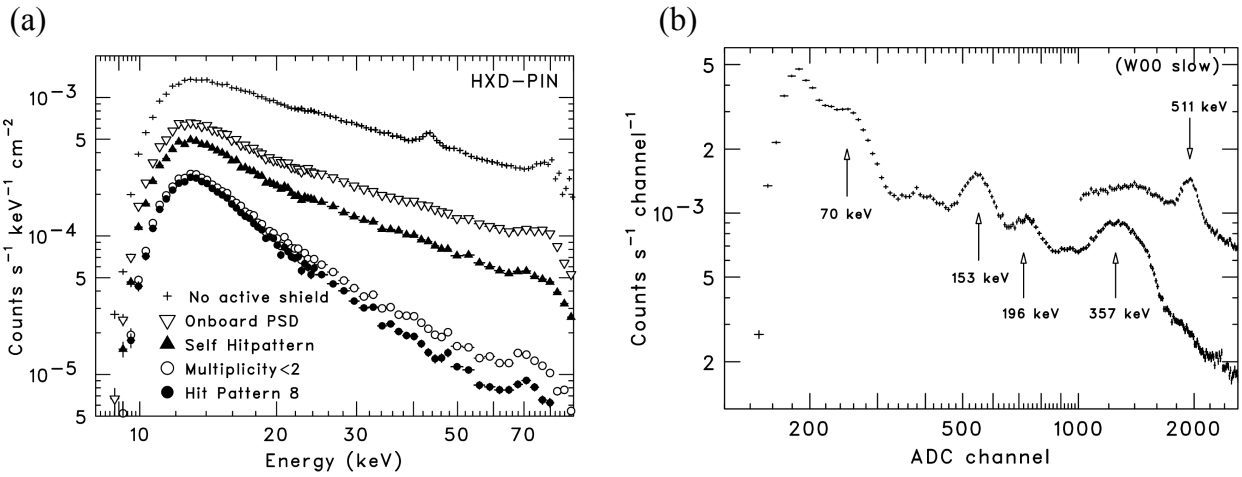

Figure 4.14: (a) The in-orbit background spectra of HXD-PIN (64 diodes summed up) are acquired from a blank sky and processed under various screening conditions. The highest spectrum is considered raw data, whereas the lowest one is considered the final spectrum achieved on ground through standard post-observation screening. (b) The same as left panel, but for HXD-GSO (one well unit). The lower spectrum is the final spectrum employing full PSD and anti-coincidence, whereas the higher one (shown only for channels $>$ 1,000) represents the events rejected by the anti-coincidence screening (Kokubun et al., 2007).

LEO of 650 km $\times$ 610 km with 6 degree inclination. Properties of its scientific instruments are listed in Table 4.4. An overview of the NuSTAR satellite is given in Figure 4.16. This satellite is the first telescope focusing on the high-energy range of 6–79 keV and has a sensitivity two orders of magnitude higher than other telescopes. The primary scientific goal of this satellite is to study high-energy X-ray sources.

NuSTAR employs the Wolter-I type X-ray mirrors (Hailey et al., 2010), which is the same type as the *Suzaku* satellite and consists of 133 mirror shells coated with Pt/SiC and W/Si multilayers. The maximum radius, overall length, and focal length of the mirror are 191 mm, 450 mm, and 10 m, respectively. NuSTAR has two mirror units (each 38 kg) and its optics operate in the energy range of 3–79 keV.

NuSTAR has two cadmium-zinc-telluride (CdZnTe) detectors (Chen et al., 2002; Kitaguchi et al., 2011) on the focal plane of the mirror. As shown in Figure 4.17, each detector is divided into four segments, each of which has a geometrical size of 200 $\times$ 200 mm^2, a

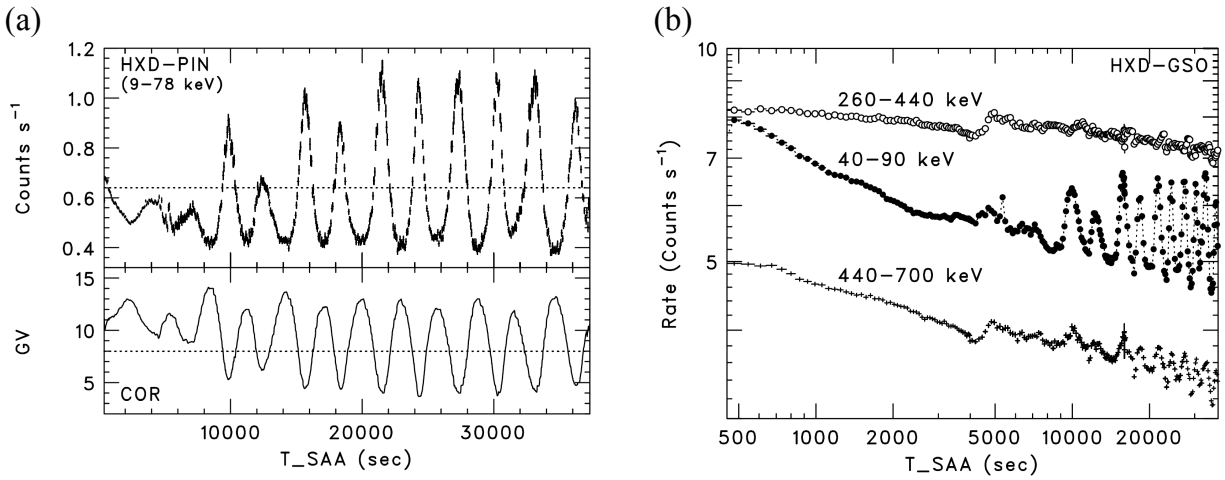

Figure 4.15: (a) In-orbit background light curves of HXD-PIN and (b) HXD-GSO (Kokubun et al., 2007).

thickness of 2 mm, and a grid size of 32×32 pixels. With an energy resolution of 0.4 keV, the CdZnTe detector is a state-of-the-art semiconductor detector operated at room temperature and is highly efficient in converting photons into electrons. The electron signals are digitally recorded using custom application-specific integrated circuits (ASICs) designed by the NuSTAR Caltech Focal Plane Team.

Table 4.4: Optics and focal plane configuration summary (Harrison et al., 2010)

Optics configuration	Focal length	10.15 m
	Number of shells	133
	Number of azimuthal segments	6 (inner)/12 (outer)
	Inner radius	5.44 cm
	Outer radius	19.1 cm
	Shell length	22.5 cm
	Min. grazing angle	1.34 mrad
	Max. grazing angle	4.7 mrad
	Coating (outer)	W/Si
	Coating (inner)	Pt/C
Focal plane configuration	Pixel size	0.6 mm/12.3″
	Focal plane size	$13' \times 13'$
	Pixel format	32×32
	Threshold	2.5 keV
	Max. processing rate	400 evt/s
	Max. flux measurement rate	10^4 /s
	Time resolution	2 μs
	Dead time fraction (weak source)	2%

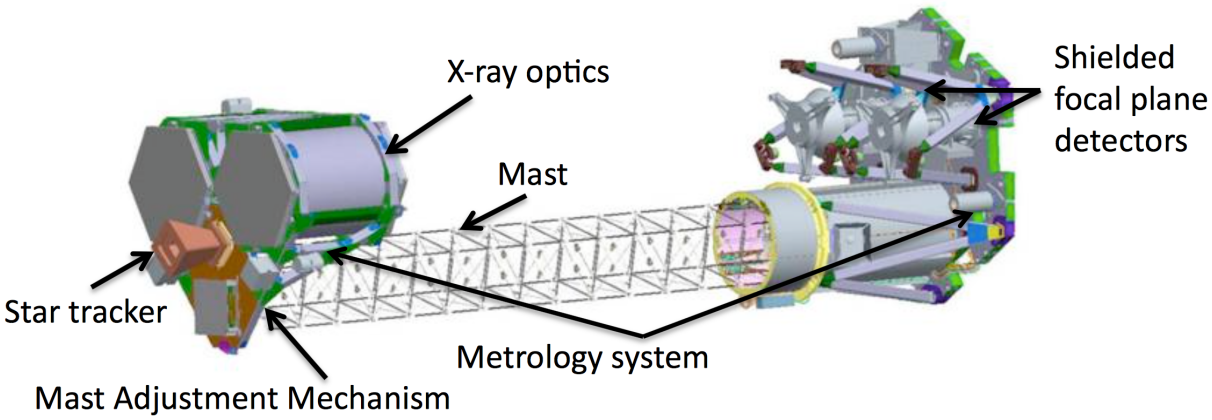

Figure 4.16: Overview of *NuSTAR* satellite (taken from Harrison et al. 2010).

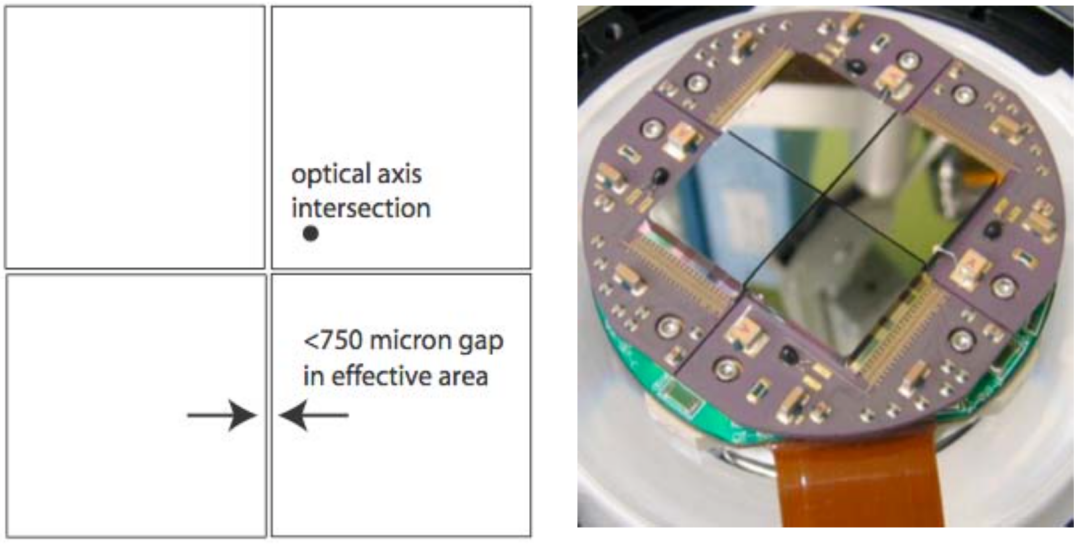

Figure 4.17: (left) The *NuSTAR* focal plane configuration and (right) photograph of an engineering test module (taken from Harrison et al. 2010).

Chapter 5

OBSERVATION AND DATA PROCESSING

5.1 Observations

Returning to Figure 3.1 (left), the long-term RXTE/PCA light curve of Aql X-1, a blue region indicates the epoch in which *Suzaku* observed Aql X-1. Aquila X-1 was in a typical outburst, and seven *Suzaku* pointings were made from September 28 to October 30, 2007 (Figure 3.2 left), to cover the outburst's decay phase. These observations are summarized in Table 5.1. The XIS nominal pointing was adopted in all observations. The XIS was operated with the 1/4 window option. Sakurai et al. (2012) noted that the spectra of Obs. D2–D4 exhibited an excess feature around 30 keV, as shown in Figure 3.4 (middle three panels). However, they did not discuss further details because the individual features were not statistically significant. In this study, we performed spectral studies of the three data, from D2–D4.

Suzaku again observed Aql X-1 in 2011 during the rising phase of the outburst, indicated in the magenta region in Figure 3.1 (right). Three pointings were made in October, and we call them Obs. R1, Obs. R2, and Obs. R3 (see Figure 3.2 right). In this thesis, we analyze the first dataset, R1, because the source was in the luminous hard state, which is similar to the three datasets gathered in 2007.

Aquila X-1 was again observed with *NuSTAR* at the end of a large outburst in 2016. *MAXI* light curve is shown in Figure 5.1 and an arrow indicates the *NuSTAR* pointing. This observation was performed on September 27, 2016, at 04:46:08, for 73 ks (ObsID: 80001043002). In this thesis, we analyze Obs. D2, D3, and D.4 to model the excess feature

and analyze the Obs. R1 and *NuSTAR* observations, which were in the same spectral state as Obs. D2 to D4, to confirm whether these spectra also exhibit similar features.

Table 5.1: *Suzaku* observations of Aquila X-1

Obs. #	Obs. ID	Date	Exposure (ksec)	Clock[a]	Snap (s)[b]
D1	402053010	2007-09-28 15:35:03	13.8	burst	0.5
D2	402053020	2007-10-03 23:49:36	15.1	normal	2
D3	402053030	2007-10-09 05:04:11	19.7	normal	2
D4	402053040	2007-10-15 08:09:00	17.9	normal	2
D5	402053050	2007-10-19 09:12:43	17.9	normal	2
D6	402053060	2007-10-24 23:34:40	21.4	normal	2
D7	402053070	2007-10-30 06:35:01	17.5	normal	2
R1	406010010	2011-10-18 12:51:33	32.8	burst	0.5
R2	406010020	2011-10-21 03:42:33	25.2	burst	0.5
R3	406010030	2011-10-24 17:26:47	34.0	burst	0.5

[a] XIS clock mode.

[b] XIS snap time (data-taking live time).

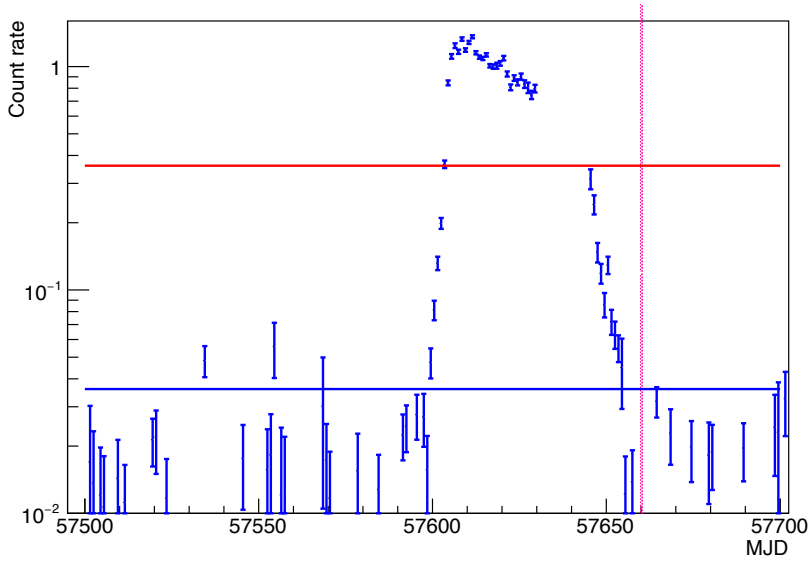

Figure 5.1: *MAXI* light curve in energy range of 2–20 keV. The magenta region shows the *NuSTAR* pointing. Horizontal red and blue lines are fluxes corresponding to 100 mCrab and 10 mCrab, respectively.

5.2 *Suzaku* Data Reduction

X-ray events are accumulated photon-by-photon with an arrival time, PH, and a hit position on the CCD camera. The data-reduction process includes the following two steps. First, bad data such as noisy pixels in a CCD camera, the period after passing the SAA, and Earth's occultation are eliminated by selecting good timing interval (GTI) from an unfiltered event. Second, hardware-specific quantities of arrival time in a satellite clock, PH, and the hit position on a CCD camera (for XIS) are converted to a universal time, photon energy, and celestial coordinates, respectively. To perform the data reduction, it is necessary to know the energy calibration or attitude solution. This information is provided by NASA/GSFC as caliblation database (CALDB).

5.2.1 XIS data processing

We used XSELECT in HEASoft (ver. 6.18; Arnaud 1996) to extract the XIS images, light curve, and spectra from the cleaned XIS event files (screened by the above selection criteria). Figure 5.2 shows the XIS images of Obs. D2–D4. We accumulated the on-source events within a circle of $2'$ radius, and extracted the background events from a rectangular region next to the source region of size $\sim 100 \times 250$ pixels. The spectral feature in the hard X-ray band is important to our analysis; hence, we need to avoid spectral distortions due to the pileup effect. To eliminate the pileup events, we excluded the core of the CCD image with a radius of $\sim$ 18 to 27 pixels in the detector coordinates, which was large enough to reduce the pileup effect below 1%. The detector response and auxiliary files were generated with `xisrmfgen` and `xissimarfgen` in HEASoft. We generated 400,000 photons to simulate the auxiliary files.

5.2.2 HXD data processing

We applied `aepipeline` to the HXD raw data to extract the cleaned events, which were screened by the following selection criteria: (a) the instantaneous pointing within 1.5 arcmin of mean (b) the time after passing SAA is larger than 500 s (c) the time to next SAA should be larger than 180 s (d) the cutoff rigidity is larger than 6 GeV (e) the target object should be above the Earth rim by at least 5°. We used `hxdpin(gso)xbpi` in FTOOLS to extract the spectra, light curves, and response files. The NXB spectra were created from a fake event file provided by the HXD team. The cosmic X-ray back-

ground (CXB) spectrum was simulated by the `hxdpinxbpi` tool, which is based on the parametrization of Boldt (1987).

$$CXB(E) = 9.41 \times 10^{-3} \left(\frac{E}{1\ \mathrm{keV}}\right)^{-1.29} \exp\left(\frac{E}{40\ \mathrm{keV}}\right) \quad \mathrm{photonss^{-1}cm^{-2}keV^{-1}FOV^{-1}} \tag{5.1}$$

Later, both the NXB and CXB were subtracted from the on-source spectra and light curves. In the three observations, the HXD-PIN and HXD-GSO signals were successfully detected over 15–50 keV and 50–100 keV, respectively.

Figure 5.4 shows the background-subtracted light curves of XIS, PIN, and GSO for Obs. D2–D4. As shown in Figure 5.4, these light curves have no X-ray burst events, and the time variation is random with less than 10%, which means data is not in state transition and spectral change is not expected. Therefore, in our analysis, time-averaged spectra were utilized. Furthermore, in the 2011 data, as shown in Figure 5.5, the light curve has no significant time variability; therefore, we analyzed the time-averaged spectrum.

5.3 Data Reduction for *NuSTAR*

To create cleaned and calibrated event files with `nupipeline` on HEASoft, the extracted images of FPMA and FPMB, which are the focal plane detectors, are shown in Figure 5.6. We accumulated a source region with a circle of 1 arcsecond radius and selected the background events from a circular region of the same size as the source region. Then, we ran `nuproduct` in HEASoft to extract the spectral and light curve files. The background-subtracted light curves are shown in Figure 5.7. These data are approximately an order of magnitude dimmer than the 2007 data. Although the observed flux gradually decreased $\sim 67\%$ with time, to improve the photon statistics, we utilized a time-averaged spectra.

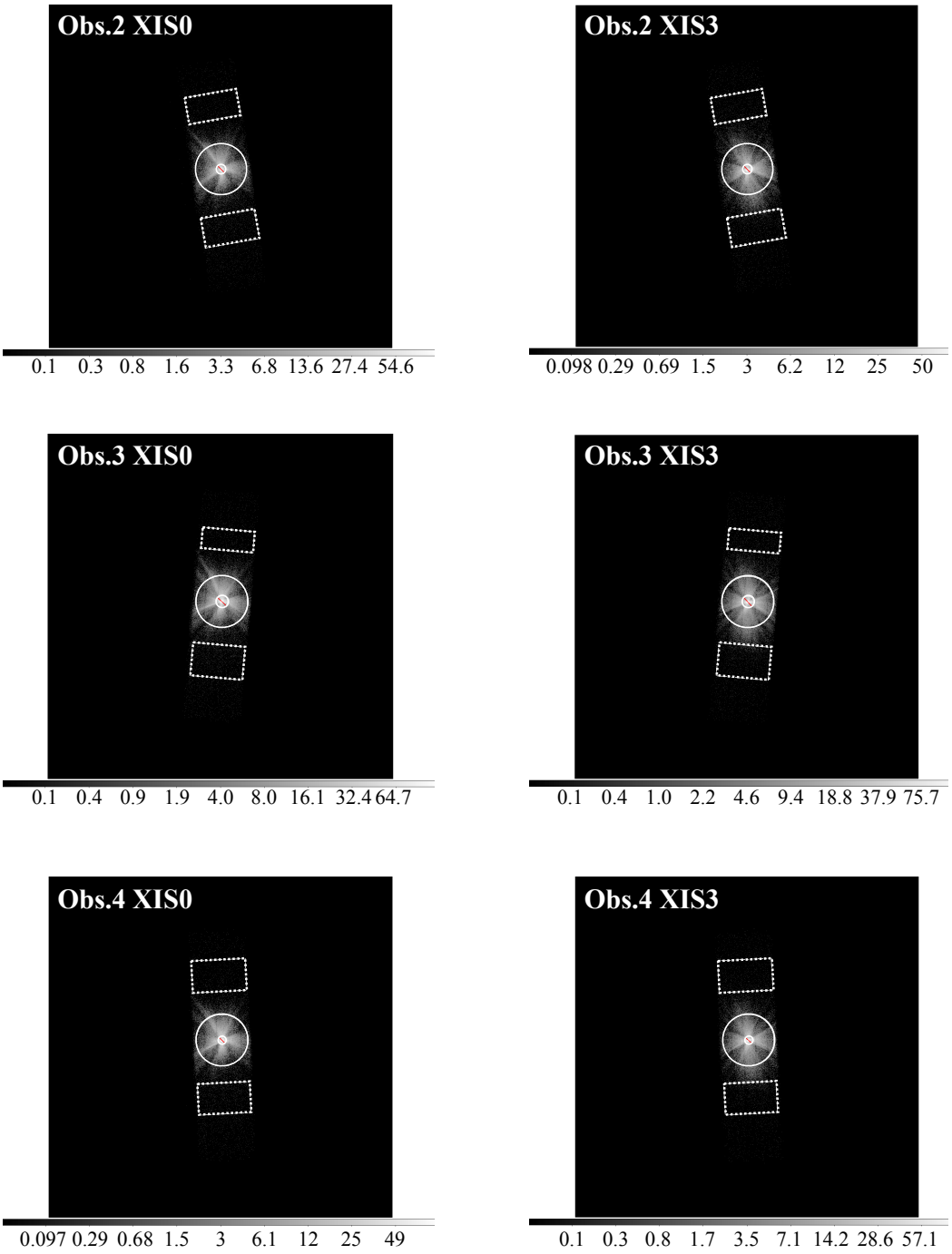

Figure 5.2: XIS images of Aql X-1 Obs. D2–D4. Source and background regions are shown by solid and dashed lines, respectively. Circles representing the center of the source region have been excluded to eliminate pileup events.

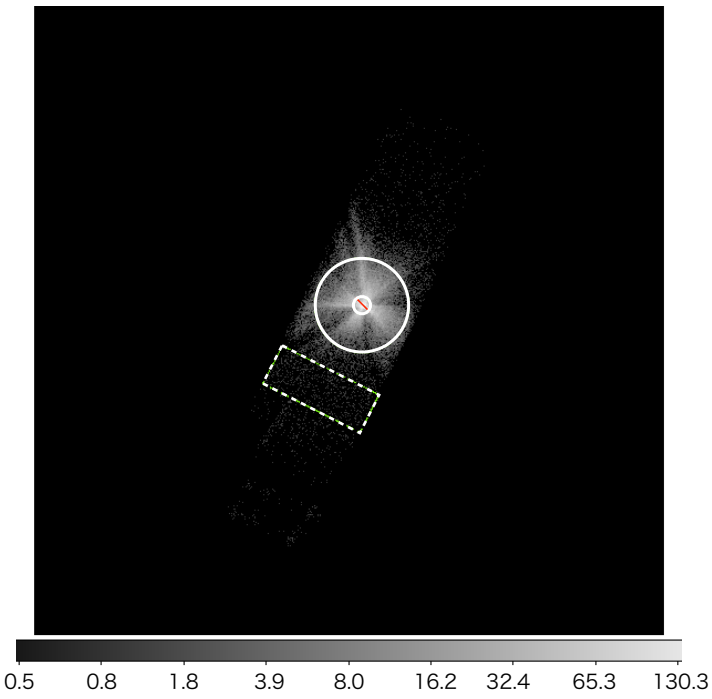

Figure 5.3: Same figure as Figure 5.2, but XIS images belong to Aql X-1 Obs. R1.

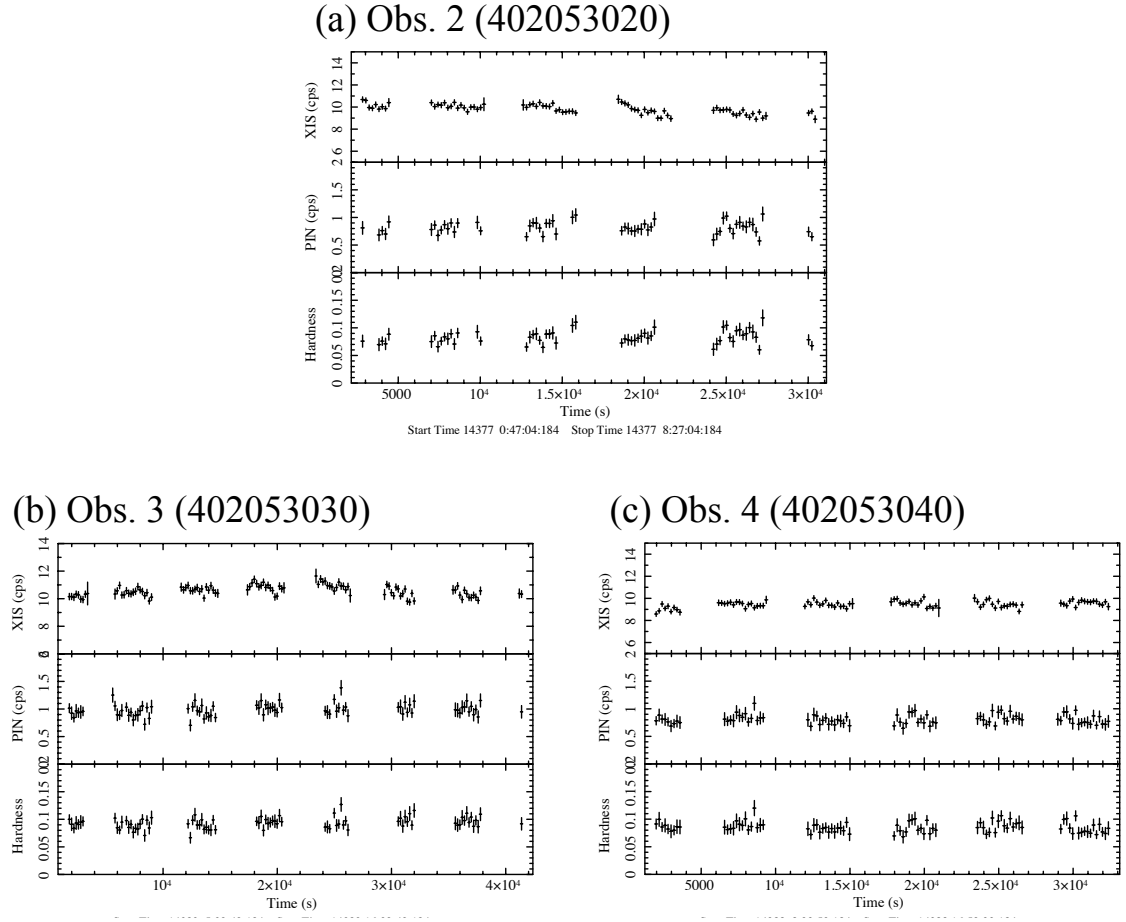

Figure 5.4: *Suzaku* light curve of Obs. D2, Obs. D3, and Obs. D4. Each top and middle panel illustrates XIS and HXD-PIN light curves, respectively. Bottom panels show the ratio of HXD-PIN to XIS.

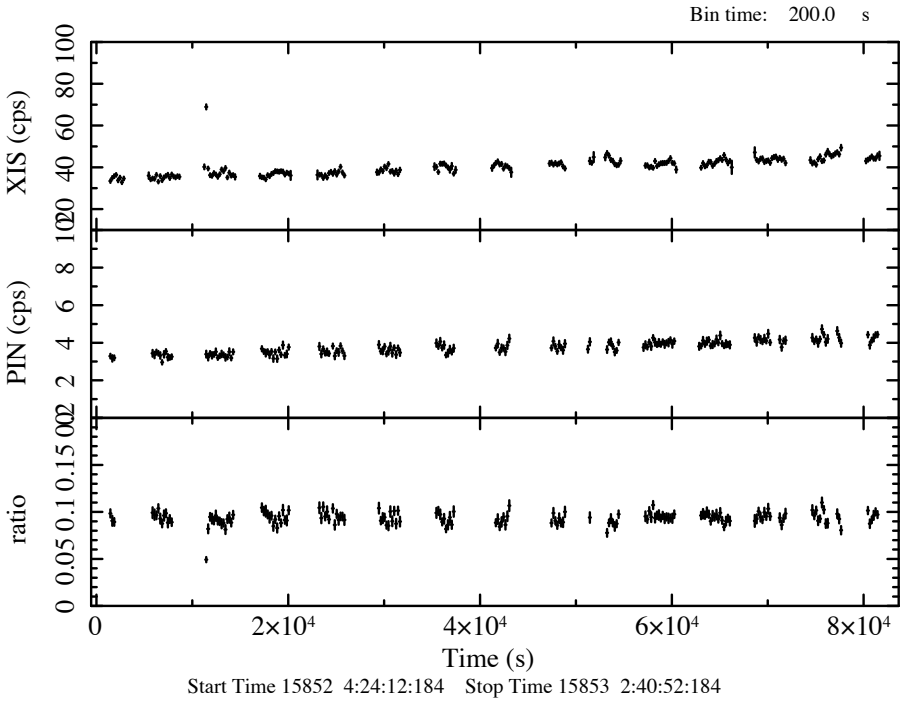

Figure 5.5: Same figure as Figure 5.4, but the *Suzaku* light curve belongs to Obs. R1.

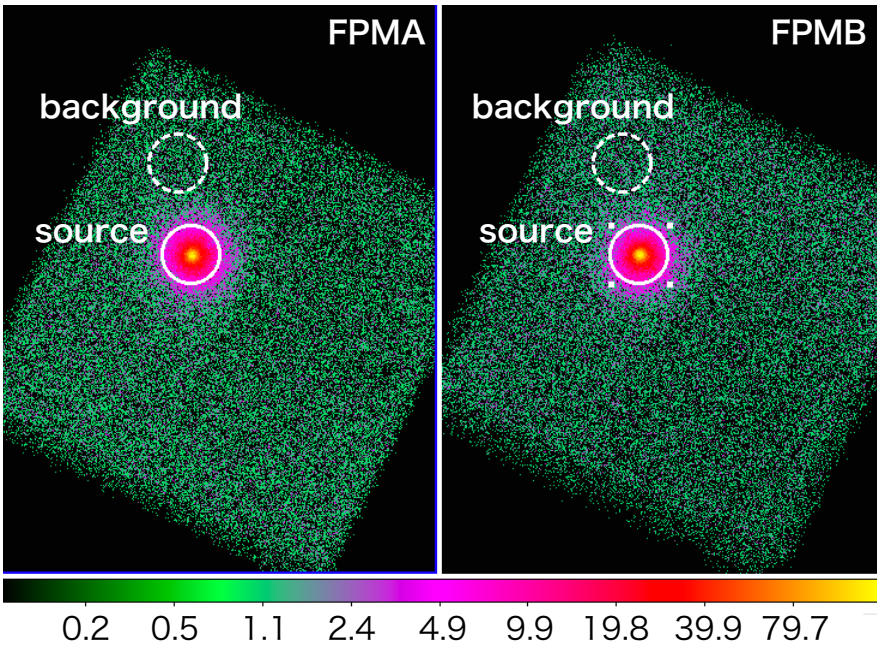

Figure 5.6: Images of (left) FPMA and (right) FPMA. Solid and dashed circles represent the source and background regions, respectively.

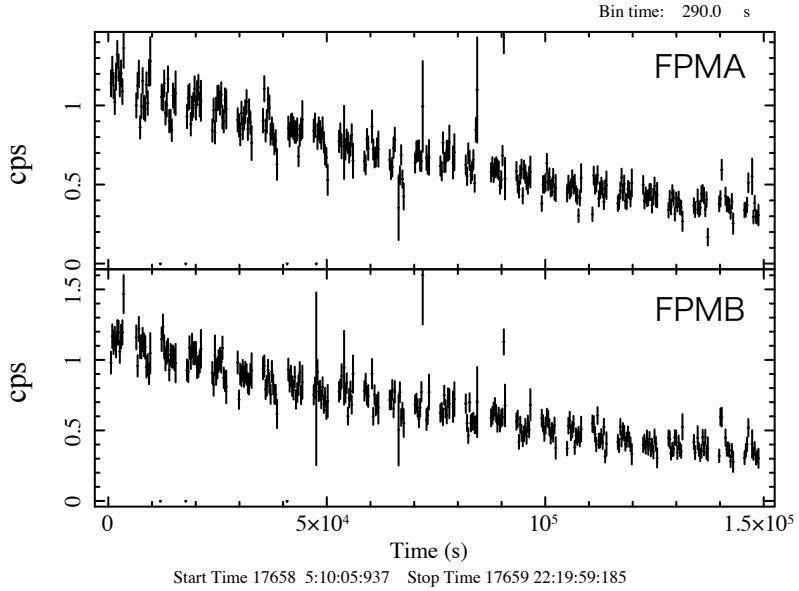

Figure 5.7: Background-subtracted light curves. Top and bottom panels are FPMA and FPMB, respectively.

Chapter 6

ANALYSIS AND RESULTS

In this chapter, we try to fit the individual spectra from Obs. D2, D3, and D4 with a canonical LMXB emission model and its variants, to confirm the presence of hump-like excess mentioned in Chapter 1, §3.2.3, and §5.1. In order to quantify it, the three spectra are summed up to maximize the photon statistics. The analysis employs the XSPEC (version 12.9.1) tool, in which all the spectral models used in the present study are predefined. In the following spectral analysis, we simultaneously fit the XIS and HXD spectra with a common model. That is, the model is convolved with the XIS and HXD responses, which are to be compared with the actual XIS and HXD spectra. The cross-normalization between the actual XIS and HXD data in reality deviates marginally from the nominal value of 1.00. It has been calibrated with the Crab Nebula data obtained on many occasions (Ishida 2006, 2007; Maeda 2008). We multiplied a fixed constant factor of 1.158 to the HXD spectra after Kokubun et al. (2007) and Sakurai et al. (2012). To avoid instrumental effects, we ignored the range of 1.7–2.4 keV, which corresponds to the silicon K-edge and gold M-edge. This is due to the large calibration uncertainties around the energy band.

6.1 Analysis of the Individual Spectra

From each of the three observations (§5.1), we produced the XIS and HXD (PIN+GSO) spectra and fitted them simultaneously using the two-component spectral model of NS-LMXBs, which was constructed by Sakurai et al. (2012, 2014). The model consists of a multi-color blackbody emission from the optically thick accretion disk and a single-zone, Comptonized blackbody emission model. The former component is represented by `diskbb`

(Mitsuda et al., 1984), which is parametrized by the inner-edge temperature $kT_{\rm in}$ and the normalization, $K_{\rm MCD}$, related to the inner-disk radius as

$$R_{\rm in} = \xi\kappa^2 (K_{\rm MCD})^{1/2} \left(\frac{D}{10 \text{ kpc}} \right) (\cos i)^{-1/2} \tag{6.1}$$

where $D = 5.2$ kpc is the working distance, $i = 45^\circ$ is an inclination assumed following Sakurai et al. (2012), $\xi = 0.412$ describes the effects of the inner-boundary condition of the disk, and $\kappa = 1.7$ (Shimura and Takahara, 1995) is the color heating factor. The latter one is represented by `compPS` (Poutanen & Svensson, 1996) which is parametrized by the electron temperature $kT_{\rm e}$, the seed blackbody temperature $kT_{\rm bb}$, the coronal optical depth τ, the reflection solid angle, and the normalization, $K_{\rm Comp}$, which is related to the blackbody radius of the seed blackbody as

$$R_{\rm bb} = (K_{\rm Comp})^{1/2} \left(\frac{D}{10 \text{ kpc}} \right). \tag{6.2}$$

In this way, seed photons of the `compPS` model are assumed to be the blackbody radiation emanating from the neutron star's surface, and the Comptonized electrons are assumed to have a Maxwellian distribution. A reflection component, which represents the effect of reflection and reprocess from the neutron star's surface, in `compPS`, was considered. We chose a `compPS` geometry parameter of 4, which means that the corona is distributed spherically around the neutron star, and fixed the binary inclination to 45°.

As shown in previous studies (Lin et al. 2007; Sakurai et al. 2012,2014), an Fe K_α emission line is observed in the present Aql X-1 spectra. A Gaussian model was therefore incorporated by fixing its mean and width to 6.4 keV and 0.1 keV, respectively (Sakurai et al., 2012). The interstellar absorption was modeled by `tbabs`,

$$\texttt{tbabs}(E) = \exp(-N_{\rm H}\sigma(E)), \tag{6.3}$$

where $N_{\rm H}$ is the hydrogen column density and $\sigma(E)$ is the photo-ionized cross-section referring to the abundance table of Wilms et al. (2000). We fixed the parameter to $N_{\rm H} = 0.36 \times 10^{22}$ cm^{-2}, which has been well determined by Sakurai et al. (2012). Hereinafter, our fits will incorporate a systematic uncertainty of 1%, following Sakurai et al. (2012). We fitted the individual spectra with the `tbabs*{diskbb + compPS(bbody) + Gaussian(FeK)}` model, and hereinafter refer to it as "the canonical model."

Panels (a)–(c) of Figure 6.1 show the spectra from three observations, all fitted with the canonical model. The best-fit parameters are listed in Table 6.1. In the present thesis, we

consider that a fit is acceptable when the null-hypothesis probability is $> 5\%$. In addition, the three spectra were found to have consistent spectral shape parameters (within errors in 90% limit), including the inner-edge disk temperature of $kT_{\rm in} \sim 0.24$ keV, the blackbody temperature of $kT_{\rm bb} \sim 0.48$ keV, the Comptonizing electron temperature of $kT_{\rm e} \sim 55$ keV, the optical depth of $\tau \sim 1.1$, and the reflection solid angle of $\sim 2\pi$.

Although the canonical model was generally successful, the fit results all exhibited an excess feature at 30 keV, which is most prominent in Obs. D3; this anomaly is the crux of the present thesis. To examine whether the feature is statistically significant, and if so, whether it is consistent among the three observations, we temporarily added a Gaussian component around 30 keV to the canonical continuum. In the fits to the Obs. D2 and Obs. D4 spectra, the Gaussian width, σ, was not well constrained; therefore, it was fixed to 4.5 keV, which was obtained from Obs. D3.

The obtained fits are presented in panels (a')–(c') of Figure 6.1, and the best-fit parameters of the Gaussian component are listed in Table 6.2. The derived equivalent width (EW) is positive (at 90% confidence level). Furthermore, within the margin of errors, the EW is mutually consistent among the three spectra, and so is the Gaussian centroid energy $E_{\rm c}$. The continuum parameters did not change much after the addition of the Gaussian component. Thus, all the three spectra significantly and consistently exhibit the excess feature around 30 keV above the Comptonized continuum.

Table 6.1: The best-fit parameters of individual fitting of Obs.2–4.

Component	Parameter	Obs. 2	Obs. 3	Obs. 4
`diskbb`	$kT_{\rm in}$ (keV)	0.25 ± 0.03[c]	0.26 ± 0.03	$0.20^{+0.05}_{-0.03}$
	$r_{\rm in}$ (km)[ab]	30^{+11}_{-7}	33^{+9}_{-7}	34^{+27}_{-15}
`CompPS`	$kT_{\rm e}$ (keV)	59 ± 7	48 ± 5	58 ± 6
	$kT_{\rm bb}$ (keV)	$0.49^{+0.03}_{-0.02}$	0.49 ± 0.03	$0.47^{+0.02}_{-0.01}$
	τ	1.0 ± 0.1	1.3 ± 0.1	1.1 ± 0.1
	reflection (2π)	$0.84^{+0.31}_{-0.26}$	$1.0^{+0.3}_{-0.2}$	$0.89^{+0.28}_{-0.24}$
	$R_{\rm bb}$ (km)[a]	10 ± 1	11 ± 1	11 ± 1
`Gaussian (FeK)`	norm (10^{-5})	$0.61^{2.9}_{-0.61}$	5.8 ± 3.1	$0.59^{2.6}_{-0.59}$
Fit goodness	χ^2_ν (ν)	1.13 (219)	1.00 (219)	1.22 (219)

[a] Assuming a distance of 5.2 kpc without its error (0.7 kpc).

[b] Assuming the source inclination of 45 degrees.

[c] We employed 90% confidence range to determine the errors.

Table 6.2: Gaussian parameters obtained from individual spectrum. The symbols are defined in text.

Obs. #	$E_{\rm c}$	σ	EW	χ^2/dof	
	(keV)	(keV)	(keV)	w/o Gaussian	w Gaussian
Obs. 2	31^{+4}_{-3}	4.5 (fixed)	$7.3^{+3.2}_{-3.2}$	1.13 (219)	1.08 (217)
Obs. 3	33^{+3}_{-2}	$4.5^{+4.1}_{-2.1}$	$8.8^{+6.4}_{-3.5}$	1.00 (219)	0.88 (216)
Obs. 4	31 ± 5	4.5 (fixed)	$3.7^{+2.6}_{-2.5}$	1.22 (219)	1.21 (217)

6.2 Analysis of the Merged Spectrum with Several Continuum Models

Now that the three spectra were confirmed in §6.1, to exhibit a consistent continuum shape and a consistent 30 keV feature, they were summed up with `addascaspec` in HEASoft to improve the photon statistics. The merged spectrum, as shown in Figure 6.2 (red spectrum), is similar in shape to the individual spectra (Figure 3.3), but with better photon statistics. To the GSO data points, we added (in quadrature) a larger systematic error,

that is, 1σ systematic uncertainty of NXB, which is 0.7% of the average NXB intensity (Fukazawa et al., 2009), and it is comparable to $\sim$20% of the signal. For reference, this systematic error of the GSO data was considered negligible when analyzing the individual spectra, because of larger statistical errors they would introduce.

6.2.1 Fit with the canonical continuum model

To the merged spectrum, the same canonical model as in §6.1 was applied. The obtained best fit parameters, which are listed in Table 6.4, are consistent with those obtained from the individual spectra. Then, as shown in Figure 6.5a, the spectrum was roughly represented over the 0.8–100 keV range by this model. However, a positive residual was again seen around 30 keV, even after the fit considered the reflection effect that produces a broad hump around a few tens of keV. Because of the improved statistics, the fit deteriorated to χ^2_ν (ν) =1.23 (219), implying a null-hypothesis probability of 1.2% for this model to be acceptable. To confirm that the fit failure was due to the 30 keV excess, the same fit was repeated by eliminating data in the energy range of 23–40 keV. The fit goodness was then significantly improved to χ^2_ν (ν) =1.07 (205). This result shows that the canonical model was rejected due to the 30 keV excess.

To confirm that the feature could be represented by modifying the reflection signals, other continuum models that include the reflection effect were considered, including `pexriv` (García et al., 2014) or `relxill` (Magdziarz & Zdziarski, 1995). Because these models assume the continuum to have a power-law shape, they cannot represent the blackbody spectral shape in the low-energy band. Hence, we ignored the data below 5 keV and obtained the fit shown in Figure 6.3. Thus, the feature remained statistically significant, even after employing these alternative models for reflection. This stands to reason as these reflection models, including that incorporated in `compPS`, are all based on Compton scattering and photoelectric absorption in thick neutral matter, and would not differ significantly in local spectral shapes (except, possibly, for the iron-K edge).

Because we applied the pileup rejection, the core region of the CCD image was eliminated, causing the effective area to substantially decrease. In principle, this procedure did not affect the normalization of the fitting model as the response files were built by considering the above information. However, if this correction to the XIS response is inaccurate, the fit result obtained so far employing the canonical HXD vs. XIS cross-normalization of 1.158 would no longer be justified. Therefore, we repeated the fitting by leaving the

PIN vs. XIS and GSO vs. XIS cross-normalizations both as free parameters. The best-fit spectrum is shown in Figure 6.4. The best-fit cross-normalizations obtained for HXD-PIN and HXD-GSO together with the χ^2/dof are listed in Table 6.3. These values are consistent with the canonical value, 1.158, and the fit goodness did not change significantly [1]. Naturally, the significance of the 30 keV feature remained unaffected.

Table 6.3: The obtained cross-normalization factor for PIN and GSO relative to the XIS.

	PIN	GSO	χ^2/dof
fix	1.058	1.058	$268.77/219 = 1.23$
free	1.09 ± 0.06	1.2 ± 0.3	$265.03/217 = 1.22$

6.2.2 Fit with a modified canonical model

The canonical model has several variants including the one adopted by Lin et al. (2007); it assumes that a fraction of the blackbody photons from a neutron star's surface are Comptonized, whereas the rest reach us directly without Comptonized. Hence we constructed the model as `tbabs*{diskbb + bbodyrad + compPS(BB) + Gaussian(FeK)}`, where `bbodyrad` represents the directly-visible blackbody component, with its normalization left free and its temperature tied to the seed-photon temperature of `compPS`. However, when this model was applied to the merged spectrum, the normalization of `bbodyrad` became consistent with zero, within errors, and the other parameters were essentially the same as those obtained in §6.2.1, including the blackbody temperature of 0.48 ± 0.01 keV. The constraint placed on the radius of the blackbody (assuming a spherical emission region) was < 2.3 km (90% limit). Therefore, as it can be seen in Figure 6.5b, this model has essentially reduced to the canonical model. Naturally, the fit quality could not improve with $\chi^2(\nu) = 1.23$ (218).

As a further modification, we allowed the blackbody temperature and the seed-photon temperature to vary separately. Then, as shown in Figure 6.5c, the fit was slightly improved to $\chi^2 = 1.12$ (217). However, the 30 keV hump is still visible to a similar degree. How do we address the physical implication of the fit? First, the `bbodyrad` temperature remained at 0.50 ± 0.02 keV, because it was constrained by the 1.5–2.5 keV part of the

[1] We confirmed that our analysis results in the following sections do not change significantly even when leaving the cross-normalization.

spectrum. Then, to make room for the `bbodyrad` component, the `CompPS` seed temperature was increased to 1.1 ± 0.1 keV and the Compton τ was increased by 10% from the canonical fit. Furthermore, to compensate for the increased seed temperature and the higher τ, the `CompPS` normalization had to be decrease by a factor of $\sim 13 \approx 2.2^3 \times 1.1^2$. As a result, the fit now yields a blackbody radius of 8.3 ± 0.7 km (a quadrature sum of `bbodyrad` and the `CompPS` seed). Although this value itself is reasonable, the fit also implies that only a minor ($\sim$ 7% or less) fraction of the emission region has a temperature twice as high and only the photons from that region are Comptonized. Because such a configuration is rather difficult to consider, hereinafter we ignore the directly visible blackbody component.

Table 6.4: The best-fit parameters obtained with the canonical and modified canonical models.

Component	Parameter	Canonical	Modified 1	Modified 2
`diskbb`	$kT_{\rm in}$ (keV)	$0.24^{+0.03}_{-0.02}$	$0.24^{+0.02}_{-0.01}$	$1.25^{+0.03}_{-0.02}$
	$r_{\rm in}$ (km)	30^{+8}_{-5}	30^{+7}_{-3}	30^{+7}_{-6}
`bbodyrad`	$kT_{\rm bb}$ (keV)	-	0.48 (= $kT_{\rm bb}$ in `compPS`)	0.50 ± 0.02
	$r_{\rm bb}$ (km)	-	< 2.3	8.1 ± 0.6
`CompPS`	$kT_{\rm e}$ (keV)	55 ± 4	55^{17}_{-5}	59^{+6}_{-7}
	$kT_{\rm bb}$ (keV)	$0.48^{+0.02}_{-0.01}$	0.48 ± 0.01	1.06 ± 0.10
	τ	1.1 ± 0.1	$1.12^{+0.13}_{-0.04}$	$1.18^{+0.08}_{-0.14}$
	reflection (2π)	$0.91^{+0.17}_{-0.16}$	$0.91^{+0.14}_{-0.15}$	$0.59^{+0.20}_{-0.17}$
	$R_{\rm bb}$ (km)	11 ± 1	11 ± 1	$2.1^{+0.5}_{-0.3}$
`Gaussian (FeK)`	norm (10^{-5})	2.5 ± 1.8	2.5 ± 1.7	3.2 ± 1.9
Fit goodness	χ^2_ν (ν)	1.23 (219)	1.23 (218)	1.12 (217)

6.2.3 Double Comptonization model

One of the possible explanations of the 30 keV hump is that it is an artifact of the simplicity of the continuum model. In particular, the Comptonizing corona can have more than one electron temperature, so that different cutoff energies and optical depths could produce more complex continuum shapes. We are hence motivated to test "double Comptonization" models in the following two configurations.

The first configuration follows the idea that the blackbody emission from a neutron

star's surface is Comptonized by a corona surrounding that neutron star; whereas, the emission from the disk is only partially Comptonized by a different corona (possibly localized on the disk surface). This modeling was originally employed by Sugizaki et al. (2013) and Sakurai (2015) to avoid deficits in the seed photons, and by Ono et al. (2016) to reproduce the 25–70 keV part of the spectrum of another LMXB. To examine this form of disk Comptonizaton, we replaced the `diskbb` component of the model in §6.2.1 with a `dkbbfth` model Done & Kubota (2006), in which the disk is assumed to be covered by a Compton corona from the innermost radius $r_{\rm in}$ up to a lager radius $r_{\rm tran}$. The model has five parameters – $kT_{\rm in}$, $r_{\rm tran}$, $kT_{\rm e}$, the photon index of the Comptonized component Γ, which is related to τ, and the normalization, which is translated into $r_{\rm in}$.

The merged spectrum fitted by this configuration of the double Comptonization model is shown in Figure 6.5d, and the best-fit parameters are listed in Table 6.5. The fit improved to χ^2_ν (ν) =1.11 (216), which is acceptable with a null-hypothesis probability of 13.6%. This fit improvement occurred when the disk emission became stronger in the 2–8 keV range (due to the newly invoked Comptonization) and the temperature of `compPS` increased. As a result, the negative residuals previously seen at 8–25 keV diminished. According to equation (A.1) in Kubota & Makishima (2004), we find

$$F^{\rm p}_{\rm disk} + F^{\rm p}_{\rm thc} = 0.0165 \left(\frac{r_{\rm in}}{D_{10}}\right)^2 \left(\frac{kT_{\rm in}}{1\ {\rm keV}}\right)^3 \quad {\rm photons\ s^{-1}\ cm^{-2}}, \tag{6.4}$$

where $F = F^{\rm p}_{\rm disk} + F^{\rm p}_{\rm thc}$ is the total photon flux of the `dkbbfth` component. The above fit yielded $F = 0.17^{+0.11}_{-0.03}$ photons s^{-1} cm^{-2} and $kT_{\rm in} = 0.37^{+0.05}_{-0.06}$ keV. Then, equation (6.4) yields $r_{\rm in} = 7.2^{+3.4}_{-3.7} \leq 10$ km, because a larger value would over-predict the emission below a few keV. However, this disagrees with the fact that the disk in the hard state is truncated at a radius of several tens of kilometers (Ono et al. 2017, Sakurai et al. 2012, Sakurai et al. 2014). Thus, the model is only marginally acceptable in a statistical sense, but not in a physical sense.

The other configuration of double-Comptonization model assumes that the disk is not Comptonized, whereas the blackbody from the neutron star is Comptonized by two different coronae of different temperatures and optical depths. We employed two `CompPS` components to represent this form of double-Comptonization and constructed the model as `tbabs*{diskbb + compPS(bbody) + compPS(bbody) + Gaussian(FeK)}`. The two `CompPS` components were constrained to have the same seed-photon temperature, but allowed to take separate and free $kT_{\rm e}$ and τ. The fit result is presented in Figure 6.5e. When

applied to the overall 0.8–100.0 keV energy range, this model yielded $\chi^2_\nu(\nu) = 1.12$ (216), which is comparable to that from the first double-Comptonization model. To examine the fit goodness around 30 keV, we fit the spectrum again, this time only using the energy range of 8.0–100.0 keV, fixing $kT_{\rm in}$ and the reflection-component intensity to the values obtained from the 0.8–100 keV fit. As a result, the fit became statistically inconsistent with $\chi^2_\nu(\nu) = 1.56$ (44) with a null-hypothesis probability of $\sim 1.1\%$. Thus, the 30-keV structure cannot be explained by the second double-Comptonization model either; the favorable χ^2_ν in 0.8–100 keV was mainly its "dilution" by the large ν in the 0.8–8 keV range. We do not consider this case hereafter.

Table 6.5: Parameters obtained with two forms of double Comptonization models.

Component	Parameter	Compton 1
`dkbbfth`	$kT_{\rm disk}$ (keV)	$0.37^{+0.05}_{-0.06}$
	Γ	2.0 ± 0.2
	kT_e (keV)	$2.3^{+0.5}_{-0.3}$
	norm	$(7.5^{+8.4}_{-3.2}) \times 10^{-2}$
`CompPS`	$kT_{\rm e}$ (keV)	71^{+11}_{-10}
	$kT_{\rm bb}$ (keV)	$0.49^{+0.02}_{-0.01}$
	τ	$0.97^{+0.19}_{-0.16}$
	reflection (2π)	$1.1^{+0.4}_{-0.3}$
	$R_{\rm bb}$ (km)	$9.0^{+0.4}_{-0.5}$
`Gaussian (FeK)`	norm (10^{-5})	2.5 ± 1.9
Fit goodness	χ^2_ν (ν)	1.11 (216)

6.2.4 Partial covering model

Another possible modification of the continuum model to explain the 30 keV hump is to assume partial covering configuration (e.g., Iaria et al. 2013). It represents a condition wherein the emission from a source is partially covered by a thick absorber, parametrized by its hydrogen column density $N'_{\rm H}$ and a covering fraction. Because the spectrum in this case is the sum of a directly observed emission (without the extra absorption) and the absorbed emission, it can take more complex shapes, depending on $N'_{\rm H}$ and the covering fraction.

Along with the above consideration, we multiplied the `pcfabs` factor with the canonical model to construct another modified model: `tbabs*pcfabs*{diskbb + compPS(bbody) + Gaussian(FeK)}`. The fit result obtained by this model is shown in Figure 6.5f, and the best-fit parameters are listed in Table 6.6. Thus, the reproduction of the spectrum around 30 keV was more accurate, with the fit goodness of $\chi^2_\nu(\nu) = 1.07$ (217). However, the 30 keV excess was still visible. Furthermore, the best-fit $N'_{\rm H}$ became extremely high as 1.6×10^{25} cm^{-2}, and the covering fraction was 0.30, which is a significant value. If such a dense absorber with a Compton optical depth > 1 and a significant covering fraction were to be located between the observer and the continuum source, then the X-rays emanating from the source would be scattered into 4π directions, and hence an exceedingly high luminosity would be required. The partial covering model is unphysical, and hence we do not discuss it any further.

Table 6.6: Parameters obtained with the partial covering model.

Component	Parameter	`pcfabs`
`pcfabs`	$N_{\rm H}$ (10^{22} cm^2)	$(1.6^{+0.9}_{-0.7}) \times 10^3$
	Covering fraction	$0.29^{+0.08}_{-0.07}$
`diskbb`	$kT_{\rm in}$ (keV)	0.22 ± 0.02
	$r_{\rm in}$ (km)	40^{+12}_{-7}
`CompPS`	$kT_{\rm e}$ (keV)	47 ± 4
	$kT_{\rm bb}$ (keV)	$0.46^{+0.02}_{-0.01}$
	τ	1.3 ± 0.1
	reflection (2π)	$0.97^{+0.25}_{-0.26}$
	$R_{\rm bb}$ (km)	14 ± 1
`Gaussian (FeK)`	norm (10^{-5})	$3.5^{+2.6}_{-2.5}$
Fit goodness	χ^2_ν (ν)	1.07 (217)

6.3 Modeling of the 30 keV Hump

Because the 30 keV hump was not accounted for while trimming the continuum model (§6.2), it will be regarded as real, as long as only the statistical data uncertainties are considered (systematic effects will be evaluated later). Then, the next step would be to

add on top of the canonical continuum model a spectral component that describes the local feature.

6.3.1 Gaussian model

The simplest form to express the local excess feature should be Gaussian. Although it is primarily empirical, a Gaussian form can have physical meaning as well as it could represent an atomic emission line arising from heavy elements produced by Type-I bursts. Therefore, we fit the data with the `tbabs*{diskbb + compPS(bbody) + Gaussian(FeK) + Gaussian}` model.

The obtained fit results are shown in Figure 6.6a, and the best-fit parameters are presented in Table 6.7. Thus, the model has successfully reproduced the spectrum with a fit goodness of $\chi^2_\nu(\nu) = 1.05$ (216), which is an improvement over the canonical-model fit by $\Delta\chi^2 = 42.9$ ($\Delta\nu = -3$). The associated F-value of 13.7 indicates that the probability for this improvement to occur by chance is 3×10^{-8}. The Gaussian form is centered at $E_c \sim 32$ keV, and is inferred to be moderately extended by $\sigma/E_c \sim 0.2$.. The Gaussian normalization is securely positive and translates to an EW of the feature by ~ 8.6 keV. These parameter values are consistent with those obtained from the canonical model fitting (Table 6.4). The continuum parameters did not change significantly even upon addition of the Gaussian component. The statistical significance of the added Gaussian component is calculated later in §6.4.

6.3.2 Recombination edge emission model

If the 30 keV structure is related to heavy elements, then there is a possibility that the hump is due to their K-edge absorption. Therefore, we multiply an `edge` factor to the canonical model, to construct the model: `tbabs*edge*{diskbb + copmPS(bbody) + Gaussian (FeK)}`. The K-edge energy was varied within the range of 25–50 keV. However, the fit remained relatively poor, $\chi^2_\nu(\nu) = 1.24$ (217), and the shape of the residuals also did not change. Therefore, this possibility is not pursued hereafter.

Another possible spectral feature related to the heavy elements is a recombination edge structure, namely a quasi-continuum emission above the K-edge energy produced when a plasma is strongly photo-ionized by high-energy photons so that heavy ions achieve an ionization temperature that is much higher than the kinetic plasma temperature and the free electrons in the plasma recombine with their ions through free-bound transitions.

This quasi continuum is represented by the `redge` model, which in turn is parametrized by the K-edge energy $E_{\rm e}$, the electron temperature $kT'_{\rm e}$ describing the high-energy extension of the feature, and normalization. We fit the spectrum with the `tbabs`*{`diskbb` + `compPS(bbody)` + `Gaussian(FeK)` + `redge`} model and obtained the results, which are shown in Figure 6.6b. The spectrum was successfully explained by this model with $\chi^2_\nu(\nu) = 1.02\ (216)$, which is even better (by $\Delta\chi^2 = -5.4$) than that explained by the Gaussian model. The fit yielded $E_{\rm e} \sim 27$ keV and $kT'_{\rm e} \sim 11$ keV, respectively. Because the latter is considerably lower than the temperature ($\sim kT_{\rm e}$ in Table 6.7) of the illuminating hard X-rays, the recombination-edge interpretation is self-consistent. Other parameters are listed in Table 6.7. Again, the continuum parameters did not change upon the inclusion of the edge components.

Table 6.7: Results of the Gaussian and `redge` modeling of the 30 keV feature on top of the canonical continuum model. The symbols are defined in text.

Component	Parameter	Gaussian model	`redge` model
`diskbb`	$kT_{\rm in}$ (keV)	0.23 ± 0.02	0.23 ± 0.02
	$r_{\rm in}$ (km)	33 ± 7	33 ± 7
`CompPS`	$kT_{\rm e}$ (keV)	49 ± 4	49 ± 4
	$kT_{\rm bb}$ (keV)	0.46 ± 0.02	$0.46^{+0.02}_{-0.01}$
	τ	1.2 ± 0.1	1.2 ± 0.1
	reflection (2π)	0.9 ± 0.2	1.0 ± 0.2
	$R_{\rm bb}$ (km)	12 ± 1	12 ± 1
`Gaussian`	$E_{\rm c}$ (keV)	32^{+2}_{-3}	-
	σ (keV)	6^{+4}_{-2}	-
	norm (10^{-4})	$4.8^{+4.0}_{-1.8}$	-
	EW	$8.6^{+7.2}_{-3.2}$	-
`redge`	$E_{\rm e}$ (keV)	-	27 ± 1
	$kT'_{\rm e}$ (keV)	-	11^{+10}_{-5}
	norm (10^{-4})	-	$5.0^{+2.6}_{-1.7}$
	EW	-	$6.3^{+3.3}_{-2.2}$
`Gaussian (FeK)`	norm (10^{-5})	2.5 ± 1.8	2.3 ± 1.8
Fit goodness	χ^2_ν (ν)	1.05 (216)	1.02 (216)

6.4 Significance of the Excess Feature

Although the fit improvements obtained with the Gaussian and `redge` component have been described in §6.3.1 and 6.3.2, respectively, the statistical significance of these improvements have not been explained so far. Therefore, here, taking the Gaussian modeling as a representative case, we calculate the statistical significance of the 30 keV feature using the $F-$test, which quantitatively evaluates the fit improvement by adding an additional component. An $F-$value is defined as

$$F = \frac{(\chi_1^2 - \chi_2^2)/(\nu_1 - \nu_2)}{\chi_2^2/\nu_2} \tag{6.5}$$

where χ_1^2 and χ_2^2 are statistical chi-squared components obtained with models 1 and 2, respectively, while ν_1 and ν_2 are the associated degrees of freedom, respectively. In the present case, model 1 is the canonical model and model 2 is the canonical model + Gaussian component. The canonical model fit in §6.2.1 gave $\chi_1^2/\nu_1 = 268.77/219$ and the canonical plus Gaussian model in §6.3.1, $\chi_2^2/\nu_2 = 225.92/216$. Therefore, we obtain $(\chi_1^2 - \chi_2^2)/(\nu_1 - \nu_2) = 42.85/3 = 14.28$, so that the $F-$value becomes 13.6. According to this value and the $F-$value table, the feature is then significant with a chance probability of 3.4×10^{-8}.

Strictly speaking, however, the nominal $F-$test cannot be applied to a line significance testing (Protassov et al., 2002). Therefore, we use a method proposed in section 5.2 in Protassov et al. (2002), to confirm the significance of the feature. This method was actually utilized in Iwakiri et al. (2012). For this purpose, we first used a Monte-Carlo method to simulate a large number of fake spectra through the canonical model, with the parameters fixed to the best-fit values in Table 6.4, the same instrumental response files, the same background data, and the same exposure time (53 ks). All the simulated spectra were binned using the same binning as the real data. In practice, we produced 9,687 fake spectra. Second, the simulated spectra were fit with the canonical model and the Gaussian component in the canonical model +. The Gaussian width was fixed at 6 keV, and its normalization was to take negative values. Then, from each fake spectrum, the $F-$value equation (6.5) was derived. Finally, the number of simulated spectra in which the $F-$value exceeded 13.6 was counted.

One of the simulated spectra is shown in Figure 6.7, and the obtained histogram of $F-$values is shown in Figure 6.8. Of the 9,687 realizations, only in three cases had the $F-$value exceeded the target value of 13.6. Therefore, we obtained a possibility of $3/9687 \sim 3 \times 10^{-4}$ for the serendipitous occurrence of fit improvement by adding a

Gaussian component. Although the probability is considerably higher than is indicated by the simple $F-$test procedure (3.4×10^{-8}), it is still sufficiently small, and allows as to conclude that the excess feature is statistically significant. The evaluation of the `redge` modeling should lead to the same conclusions, because it yielded an even larger value of $F = 15.7$.

6.5 Evaluation of Systematic Errors

Before discussing the origin of the 30 keV hump, the systematic uncertainties in this analysis were evaluated to confirm that the hump structure is not an artifact. Here, the detector response and the background modeling of HXD-PIN are major sources of the uncertainties.

In order to examine the accuracy of the employed HXD-PIN response, data of the Crab Nebula obtained for a similar epoch, namely, August 27, 2008 (Obs. ID = 103007010), for net 33 ks, were analyzed using the same response. This is because the Crab Nebula, which is the remnant of the AD 1054 supernova in the Taurus constellation, emits bright and featureless X-rays via synchrotron process, and its spectrum has been measured by almost all X-ray astronomy satellites as a "standard candle." The 15–50 keV Crab spectrum taken with HXD-PIN was successfully obtained with ($\chi^2/\nu = 90.1/90$), which is represented by a single power law of photon index 2.12 ± 0.01, which agrees with previous measurements with the HXD (Kokubun et al., 2007) and other experiments. As shown in Figure 6.9(b), the model-to-data ratio in 20–40 keV remained within $\pm 3.5\%$ of unity, except a feature at $\sim$ 43 keV, which is probably related to the Gd-K line (see below). This is much smaller than the 30 keV hump structure, which amounts to $\sim 40\%$ of the 20–40 keV continuum, even when employing the modified continuum models (Figure 6.5b to Figure 6.5f). Therefore, the observed 30 keV hump cannot be an artifact arising from uncertainties or inaccuracies of the instrumental response of HXD-PIN.

The NXB component of HXD-PIN is almost featureless, except for the weak Gd-K line at 43 keV arising from fluorescence in the HXD-GSO scintillators underneath HXD-PIN (Kokubun et al., 2007). A background spectrum fit with an empirical double power-law model is shown in Figure 6.10; any local feature in the 20–40 keV energy band is less than 20% of the average value. Because the NXB intensity is approximately 67% of the signal from Aql X-1 in the 20–40 keV band, any possible $< 20\%$ local feature in the NXB

component would correspond to those of $< 13\%$ in the Aql X-1 spectrum. This is not enough to explain the observed 30 keV feature as described above.

According to Fukazawa et al. (2009), the NXB model for HXD-PIN itself is known to contain 2% systematic uncertainties below 70 keV (see Table 4.2). As shown in Figure 6.11, the background signals are three times larger than the source signals at around 50 keV. Therefore, the background would affect the source signal by $\sim 6\%$. However, as seen in Figure 6.11, this is considerably smaller than the statistical error of the HXD-PIN data, which is $\sim 20\%$ for a typical binning of $\Delta E \sim 2$ keV (appropriate for the PIN energy resolution of ~ 3 keV; Table 4.1). Therefore, the systematic errors of the PIN NXB would be negligible. To confirm this reasoning, we re-analyze the merged spectrum by varying the background signal by $\pm 2\%$. As a result, neither the obtained continuum parameters nor the fit goodness changed significantly compared to the nominal fit in §6.2.1.

From these evaluations, considering both the statistical and systematic errors involved in the data, it can be concluded that the 30 keV hump structure is significant.

6.6 Analysis of 2011 *Suzaku* data

Suzaku observed Aquila X-1 once again in October 2011 in a rising phase of another outburst that had taken place. Figure 3.2b shows a MAXI 2–20 keV light curve of Aql X-1 for 200 days in 2011, where the arrows indicate Suzaku 's observation timing. The MAXI mission (Matsuoka et al. 2007) had not been launched in 2007 yet. As already published by Ono et al. (2017), the observation lasting one day captured the source at first in a luminous hard state before witnessing a remarkable hard-to-soft state transition. However, the spectrum "P0" of Ono et al. (2017), a hard-state dataset obtained from a pre-transition period, does not show the hump feature at ~ 30 keV. To examine this observation further, we accumulated data over a longer time (32.8 ks net exposure) before the transition (Obs ID: 406030010), and obtained the spectrum shown in Figure 6.2. In comparison with the merged spectrum, the 2011 spectrum is ~ 5 times brighter with a considerably harder Comptonization slope (e.g. in 3–20 keV), and it shows no particular structure at ~ 30 keV, which is in agreement with Ono et al. (2017). To fit the spectrum, we employed after Sakurai (2015)'s double-seed continuum model: `tbabs*{nthcomp(diskbb) + nthcomp(bbody) + Gaussian(1keV) + Gaussian(FeK) + Gaussian(32keV)}`, and we found that the canonical single-zone Comptonization model suffers from a shortage in

seed-photon flux. Because a harder continuum suggests a relatively high value of τ, we replaced `compPS`, which is valid for $\tau < 3$, with another model, `nthcomp` (Zdziarski et al., 1996). This model can be used for $\tau > 2$. Over the overlapping range of $\tau = 2$ to 3, the two codes are known to give consistent results (Sakurai, 2015).

Figure 6.12a shows the fit of this model, with a fit goodness of $\chi^2_\nu(\nu) = 1.24$ (240). The `nthcomp` parameters were obtained as $kT_{\rm e} = 20 \pm 1$ keV, $kT_{\rm bb} = 0.56 \pm 0.03$ keV (seed photons), and $\tau = 3.67 \pm 0.02$, as calculated using equations (2.23) and (2.24) from the photon index describing the model. Thus, the choice of `nthcomp` is self-consistent. By further adding a Gaussian, with $E_{\rm c} = 32$ keV and $\sigma = 6$ keV, both fixed to the value in Table 6.7, its EW was constrained by $1.22^{+0.80}_{-0.78}$ keV (90% confidence). Although the zero EW is still excluded, the upper limit of 2.02 keV is lower than the lower bound in the 2007 data, 4.9 keV. Therefore, the hump feature is significantly weaker (in EW) than in the merged spectrum from the 2007 outburst. Figure 6.12b shows the fit when the Gaussian is forced to take the maximum allowed EW, and the other parameters are all re-adjusted.

6.7 Analysis of 2016 NuSTAR Data

Aquila X-1 was observed with *NuSTAR* (Harrison et al., 2013) at the end of an outburst in September 2016. As shown in Figure 5.1, this observation was made at a luminosity similar to that in the 2007 *Suzaku* data analyzed in §6.1–6.3. We fitted the spectrum over an energy range of 3–70 keV with the `tbabs*{diskbb + nthcomp(bb) + Gauss(FeK)}` model, and obtained results as shown in Figure 6.13a. Because *NuSTAR* has no sensitivity, $kT_{\rm in}$ and $kT_{\rm bb}$ at 0.24 keV and 0.48 keV, respectively, which are the best-fit values of the 2007 Suzaku data (Table 6.7). The spectrum was well represented by this model with $\chi^2/{\rm dof} = 1.15(74)$. From the fit, kT_e and the power-law index were determined to be 13^{+2}_{-1} keV and 1.83 ± 0.01, respectively. From the photon index, the coronal optical depth was calculated to be ~ 4. The spectrum is slightly harder than that in the 2007 *Suzaku* data, when the photon index was ~ 2. Then, we added a Gaussian component at 32 keV, with its width fixed at 5.9 keV, to examine the spectrum for the 30 keV feature. The best-fit spectrum upon the addition of the Gaussian is shown in Figure 6.13b. Parameters are listed in Table 6.8 Although the best-fit normalization was positive, its error included zero, so that only the upper limit was obtained as < 4.1 keV, which is slightly weaker than obtained with *Suzaku* in 2007 (Table 6.7).

Table 6.8: Parameters of 2016 *NuSTAR* data.

Component	Parameter	continuum	w/ Gaussian
`diskbb`	$kT_{\rm in}$ (keV)	0.24 (fixed)	0.24 (fixed)
	norm (10^4)	2.2 ± 0.7	2.2 ± 0.7
`nthcomp`	Γ	1.83 ± 0.01	$1.82^{+0.01}_{-0.02}$
	$kT_{\rm bb}$ (keV)	0.48 (fixed)	0.48 (fixed)
	$kT_{\rm e}$ (keV)	13^{+2}_{-1}	11^{+3}_{-2}
	norm (10^{-3})	1.90 ± 0.05	1.90 ± 0.05
`Gaussian (FeK)`	norm (10^{-6})	6.3 ± 4.3	6.3 ± 4.3
`Gaussian (30keV)`	$E_{\rm c}$ (keV)	-	32 (fixed)
	σ (keV)	-	6 (fixed)
	norm (10^{-5})	-	< 3.2
Fit goodness	χ^2_ν (ν)	1.15 (74)	1.15 (73)

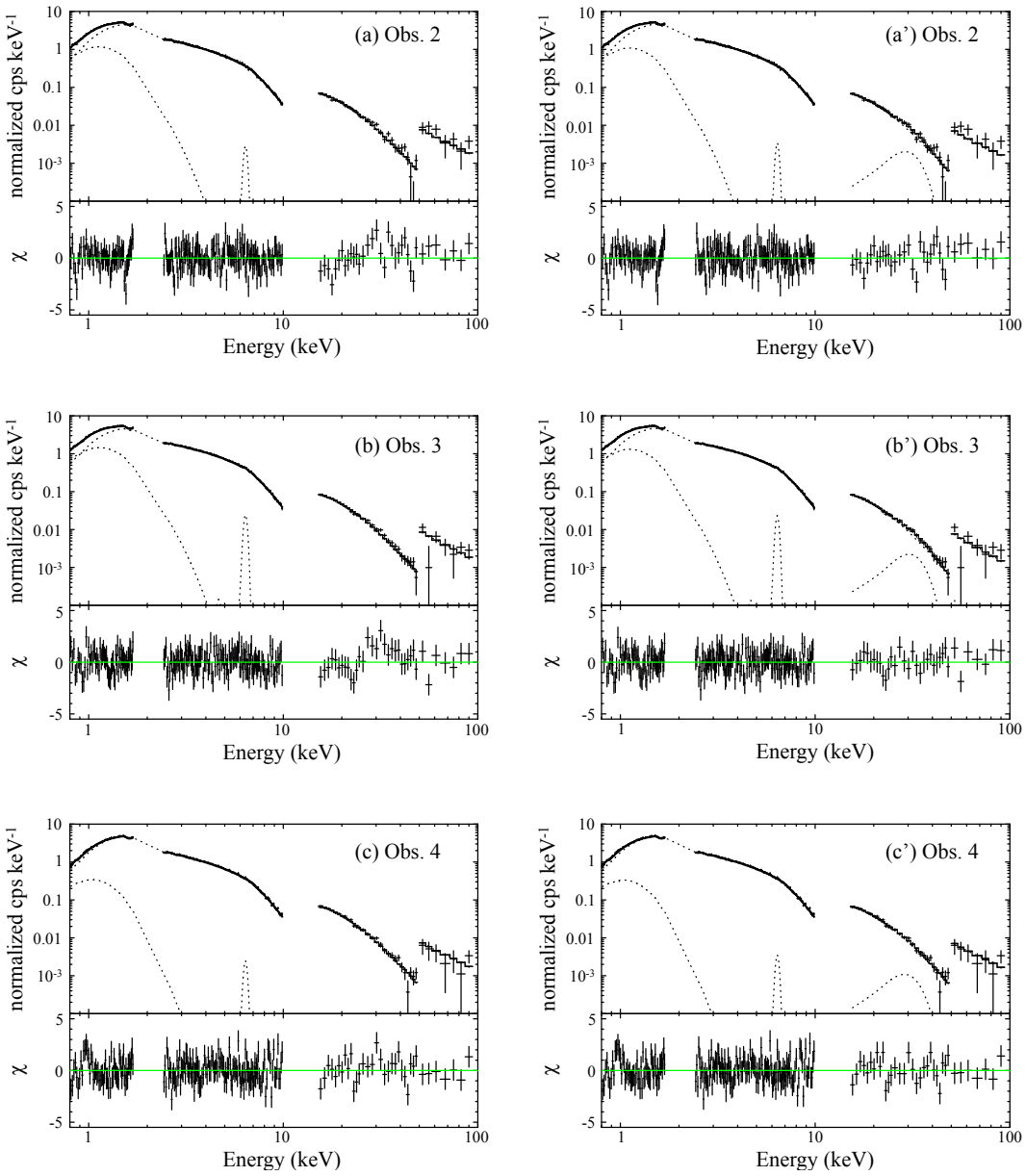

Figure 6.1: Model fits made to the individual Suzaku (XIS+HXD) spectra of Aql X-1. Panels (a), (b), and (c) are the spectra of Obs. 2, 3, and 4, respectively, fitted by the canonical model. Panels (a'), (b'), and (c') are the same spectra, but with a Gaussian component added at ~ 32 keV.

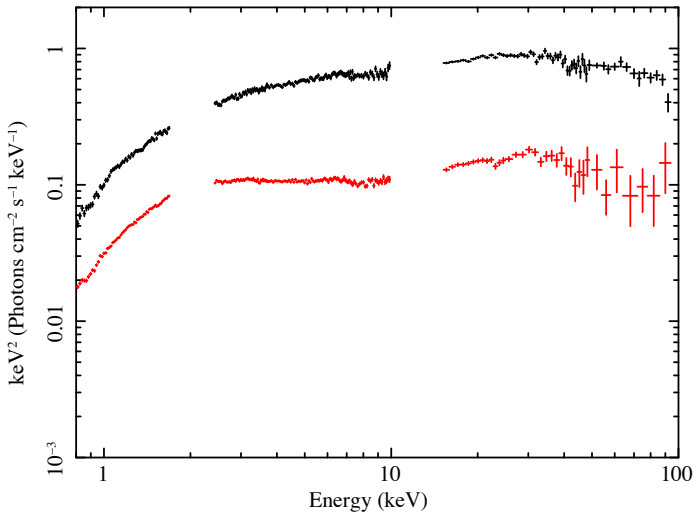

Figure 6.2: Comparison of two Aql X-1 spectra (in νF_ν form) obtained by *Suzaku*. Red shows the merged data from 2007. Black shows a spectrum taken in October 18, 2011, from UT03:42:33 to October 19, 2011, at 02:39:18, before the hard-to-soft state transition, which was reported by Sakurai (2015).

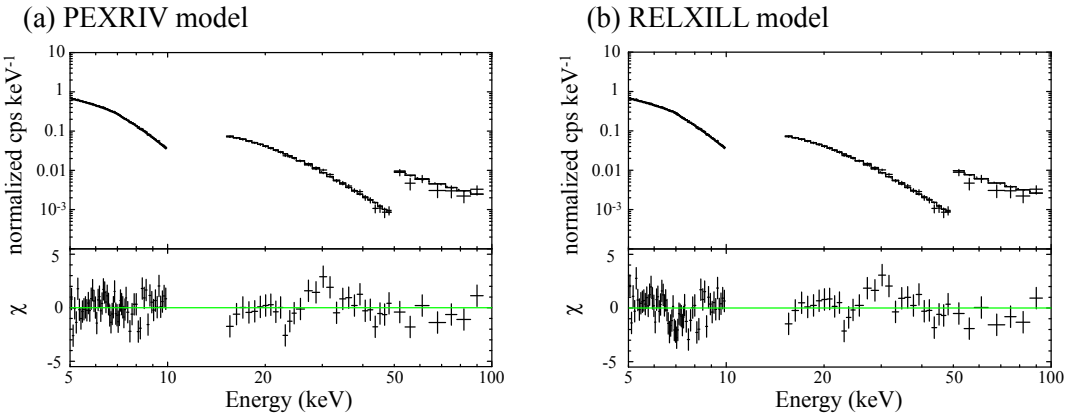

Figure 6.3: (a) Spectra when employing the `pexriv` and (b) `relxill` models to represent the reflection effect.

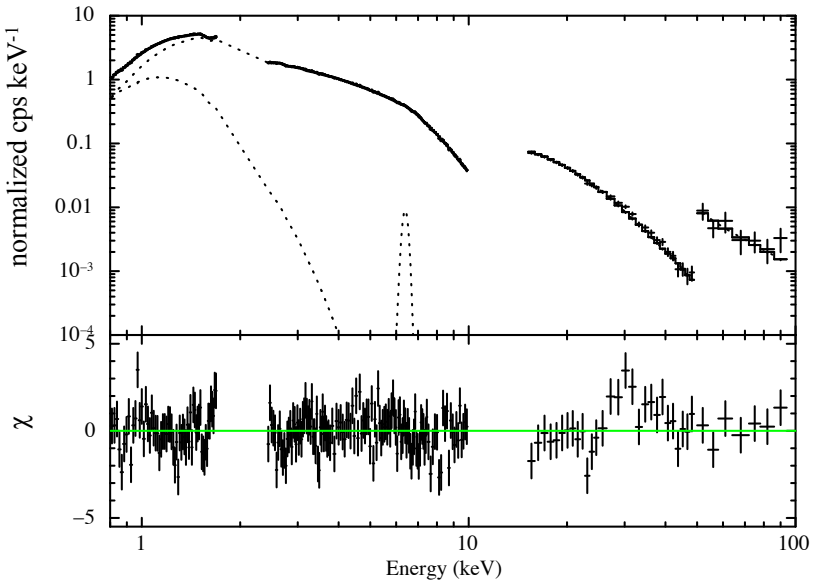

Figure 6.4: Spectrum when leaving the cross-normalization for HXD-PIN and HXD-GSO.

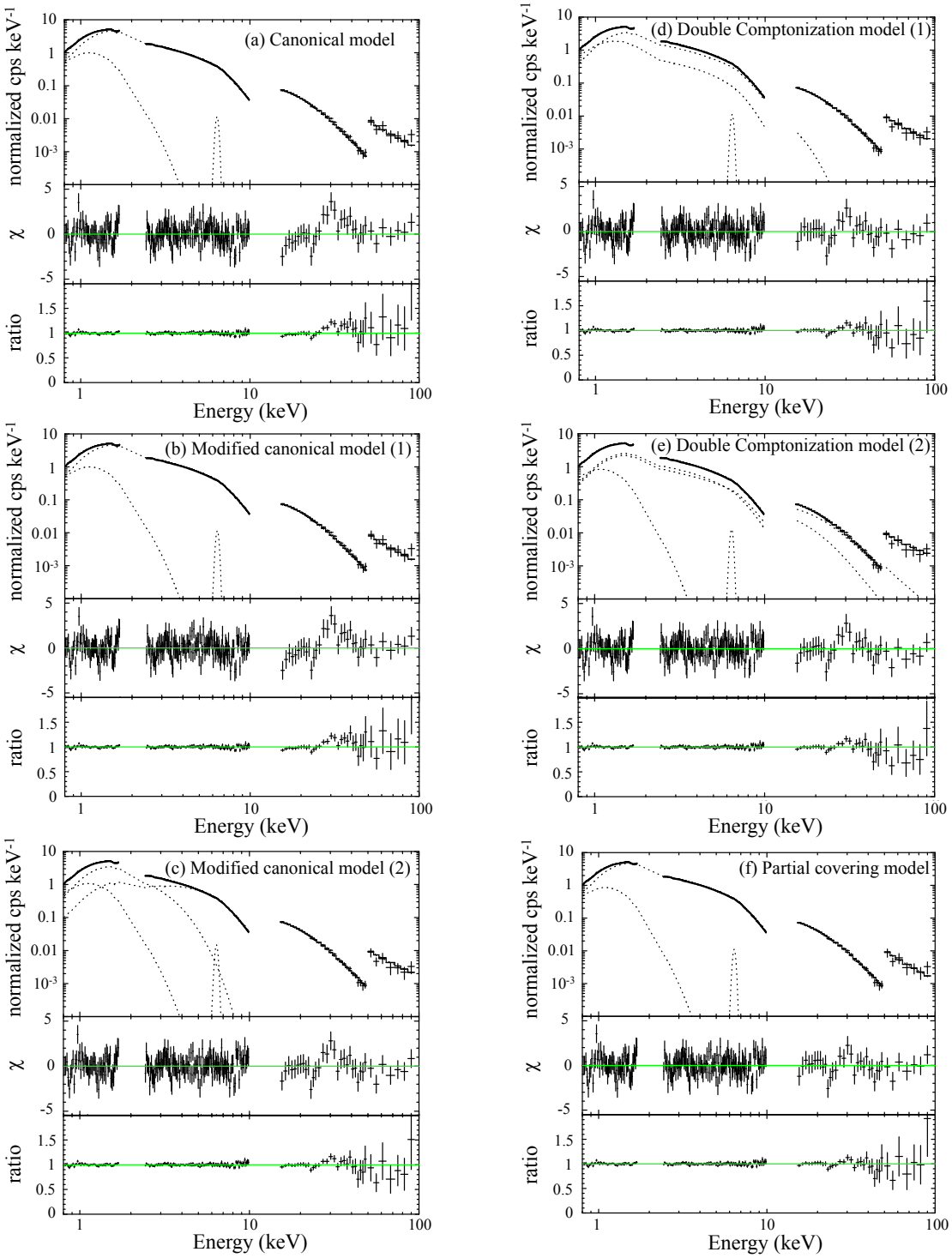

Figure 6.5: Simultaneous fittings to the same spectrum in as Figure 6.1. (a) When the canonical model (two components model) is employed (b) Result with the first modified canonical model (three components model) (c) The same as panel (b) but using the second modified model (see text) (d) A fit with the double Comptonization model of the first condition (e) The same as (d), but with the second form of double Comptonization model (f) When the partial covering model is employed

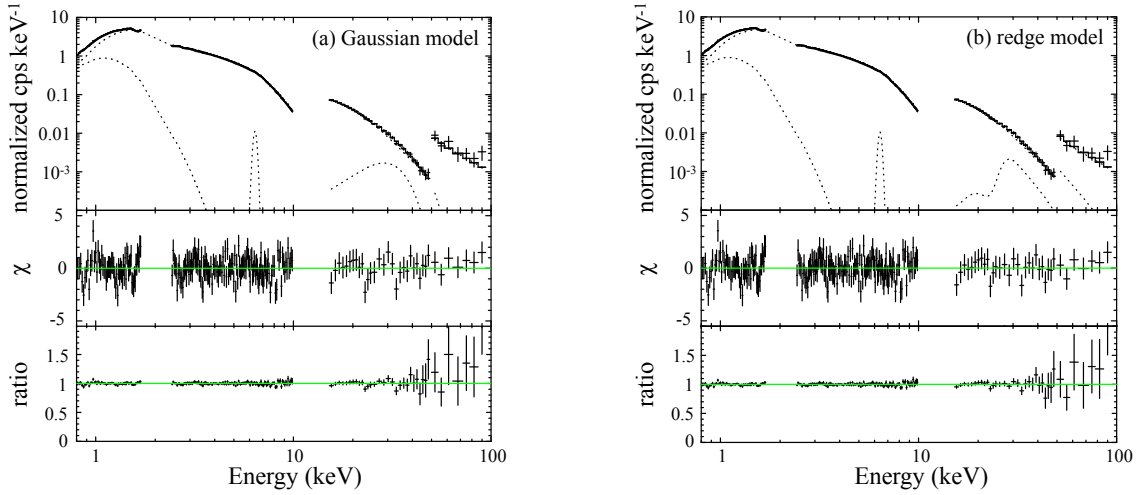

Figure 6.6: Simultaneous fittings to the same spectrum as in Figure 6.5, considering the local feature at $\sim$ 30 keV. Although the two panels are based on the same data, the final deconvolved spectra appear somewhat different due to the so-called obliging effect; the results of spectral deconvolution depend on the particular models being used in the deconvolution procedure. (a) The case of applying the Gaussian component (b) When the `redge` component is employed.

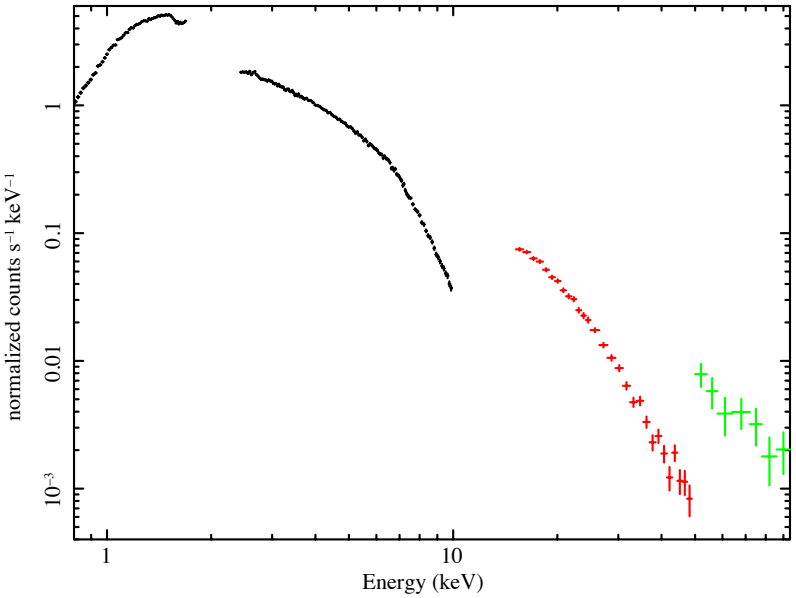

Figure 6.7: Example of the Monte-Carlo-simulated spectrum based on the canonical model. Black, red, and green show the XIS, PIN, and GSO spectra, respectively.

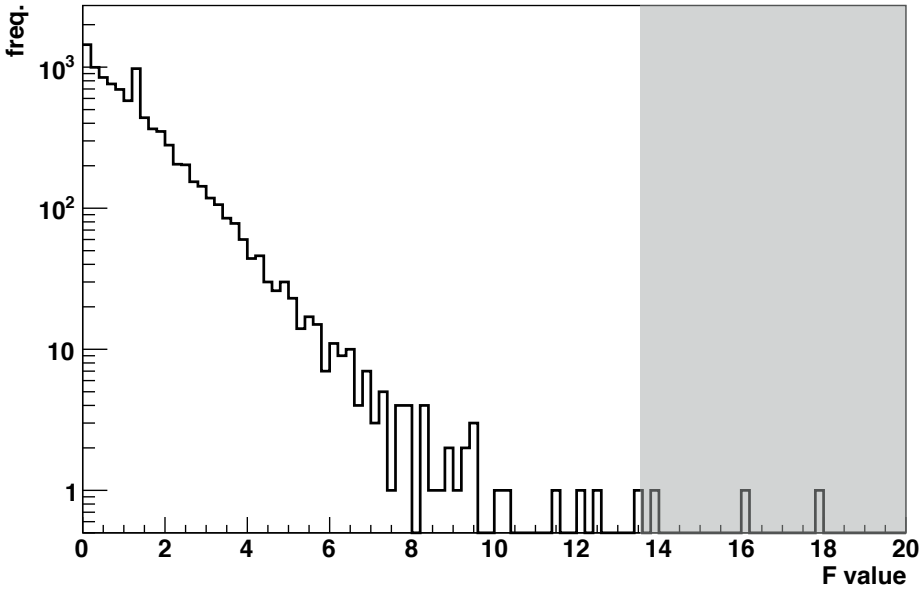

Figure 6.8: Histograms of the $F-$value derived from the 9,687 Monte-Carlo trials. Gray region indicates $F > 13.6$.

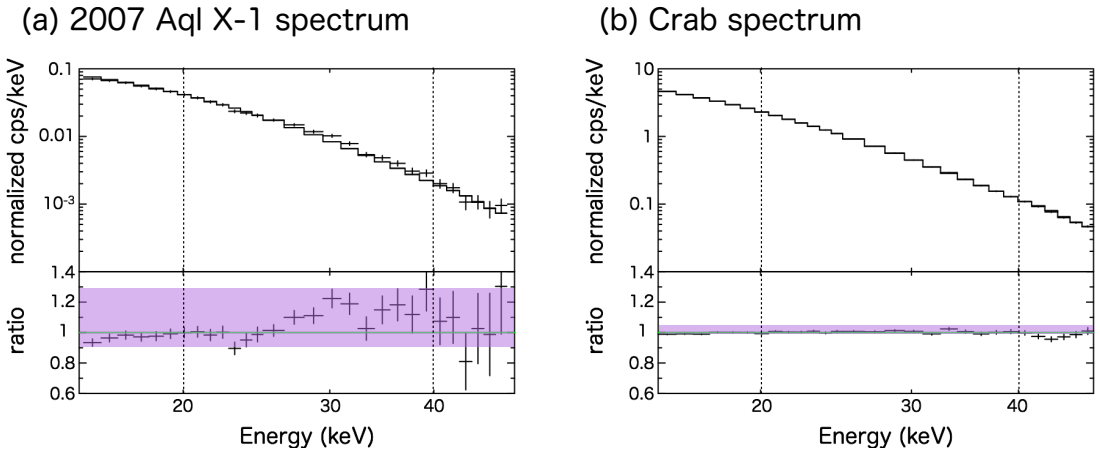

Figure 6.9: (a) Close up spectrum of Aql X-1 fitted with the Canonical emission model, for reference. (b) A Crab spectrum fit with a single power-law model. Bottom panels show the model-to-data ratio, where the purple bands indicate a scatter in the ratio (peak-to-peak) below 40 keV.

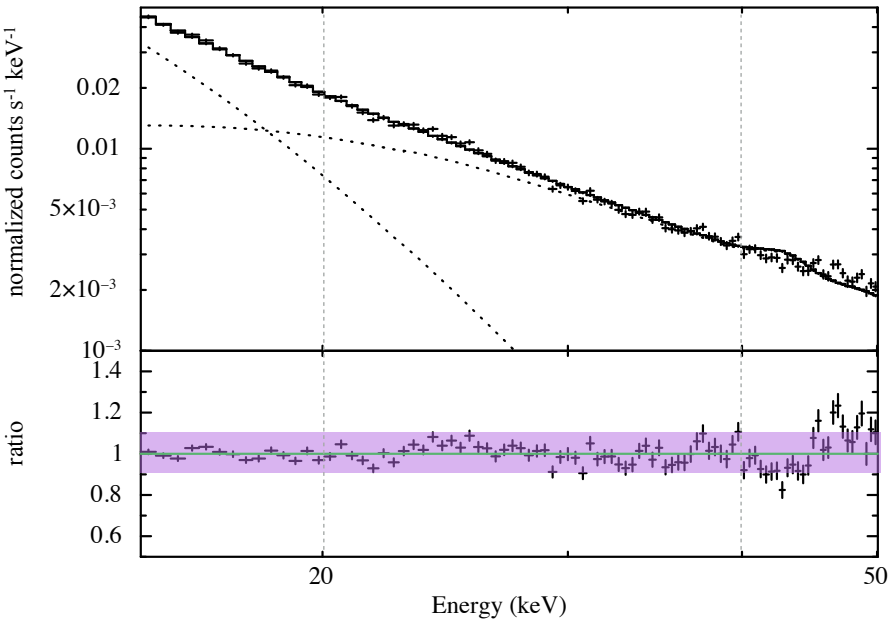

Figure 6.10: Background spectrum of HXD-PIN fitted with an empirical double power-law model. Purple band shows the scatter in the signal-to-model ratio.

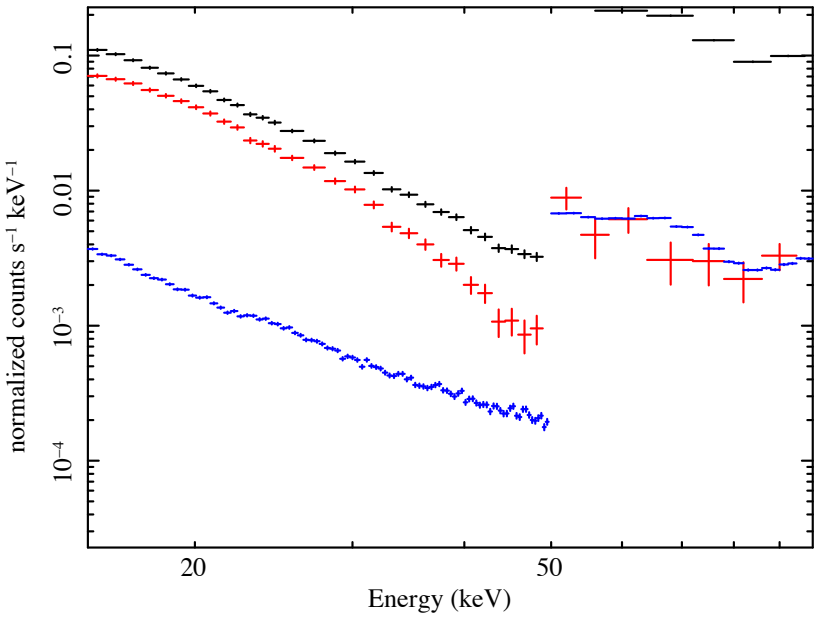

Figure 6.11: Comparison of the HXD-PIN and GSO spectra with 3σ NXB spectra (blue). Black shows the total spectra from the three observations summed up (including background signals) and red represents those after subtracting the NXB and CXB.

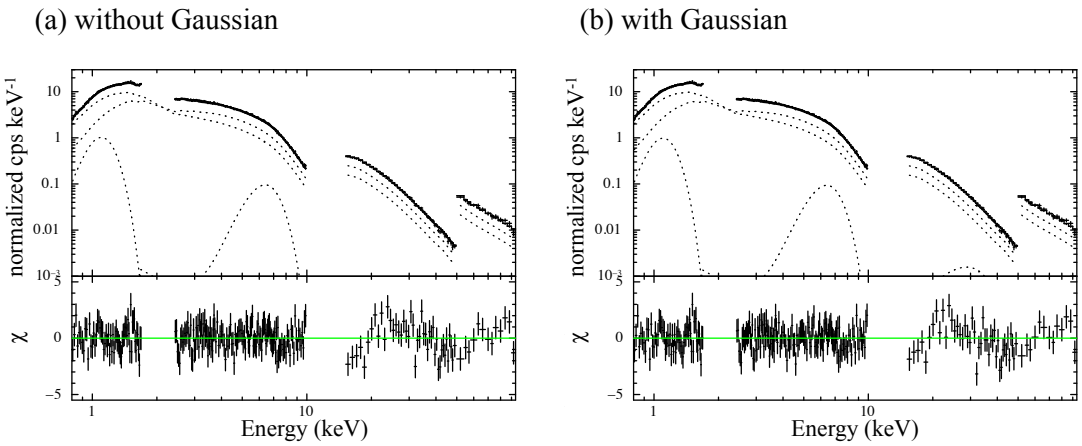

Figure 6.12: Simultaneous fitting to the XIS 0, HXD-PIN, and HXD-GSO spectra presented in Figure 6.2. (a) A fit with the `tbabs*{nthcomp(bbody) + nthcomp(disk) + Gauss(1keV) + Gauss(6.6keV)}` model. (b) The model is basically the same as (a) but a Gaussian model was added at 32 keV. See text for details.

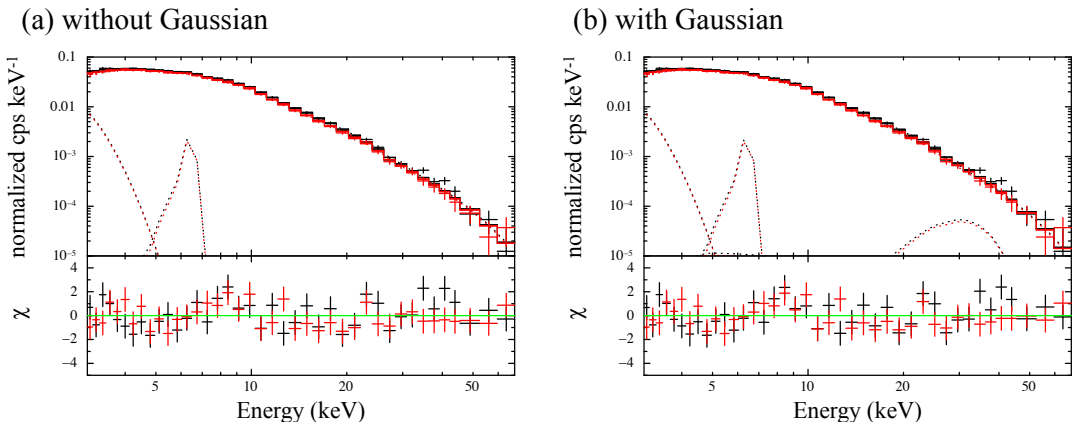

Figure 6.13: Fitting of the NuSTAR data taken in 2016. (a) A fit with the `tbabs*{diskbb + nthcomp(bbody) + Gauss(FeK)}` model. (b) The model is the same as (a) but a Gaussian model was added at 32 keV.

Chapter 7

DISCUSSIONS

7.1 General Considerations

7.1.1 Summary of the results

We analyzed three `Suzaku` spectra of Aql X-1 acquired during the decay phase of the outburst between September and October, 2007. During this interval, the object was in a typical hard state, with a luminosity of $\sim 10^{36}$ erg s^{-1} in a broad energy band of 0.8–100 keV. Over the same energy range, the spectra were approximately represented by a canonical continuum model for the NS-LMXBs in a hard state, consisting of a multi-color disk component and a Comptonized component. In addition to this continuum, the spectra exhibit a significant hump structure at $\sim$30 keV, as previously suggested by Sakurai et al. (2012). This feature is statistically significant with a probability of false detection of $\sim 3 \times 10^{-4}$ (§6.4), and cannot be attributed to known instrumental or systematic uncertainties (§6.5). This feature was successfully represented by a Gaussian centered at $E_{\rm c} = 32^{+2}_{-3}$ keV, with σ =4–10 keV and an EW of $8.6^{+7.2}_{-3.2}$ keV. Alternatively, the feature can also be explained by the `redge` model, with $E_{\rm e} = 27 \pm 1$ keV, $kT_{\rm e}$ =6–21 keV, and an EW of $6.3^{+3.3}_{-2.2}$ keV. Over the three observations during the 12 days, the 30-keV feature did not vary in the EW values within errors; however, a possible decay on a time scale of $\sim$10 days cannot be excluded (see §7.2.3). Interestingly, the 30keV feature was absent (or it was significantly weaker) in the 2011 *Suzaku* data of the Aql X-1 (§6.6) and those from *NuSTAR* in 2016 (§6.7). In the next section, the implications of these results are discussed.

7.1.2 Other observations

In §6.5, it is confirmed that the 30-keV feature is neither due to a background feature, nor to an artifact related to the HXD response. Nevertheless, it can still be attributed to certain unknown instrumental artifact specific to *Suzaku*. To eliminate this possibility, the literature was reviewed for similar phenomena. It was found, that a 3–120 keV spectrum of Aql X-1, acquired by the PCA+HEXTE onboard *RXTE* in the hard state during a small outburst in February, 2004 (Lin et al., 2007), exhibits a similar excess structure localized at 30–34 keV, as shown in Figure 7.1a. Apparently, this effect motivated the authors of this study to fit the hard X-ray section of their spectrum with a broken power-law with a break at ∼30 keV. Furthermore, as shown in Figure 7.1b, a similar, but weaker feature at 30–40 keV can be present in a joint *INTEGRAL+BeppoSAX* spectrum of the NS-LMXB 4U 1812−12 (Tarana et al., 2006).

Apparently, in contrast to the above cases, such a spectral structure at ∼30 keV is absent in several other published spectra of LMXBs in the hard state, including those from Aql X-1 itself (Rodriguez et al., 2006) and other LMXBs, such as 4U 1705−44 (Lin et al., 2010) and 4U 1608−52 (Armas Padilla et al., 2017). Therefore two important conclusions can be drawn about this feature: (i) it is neither a *Suzaku* artifact nor specific to Aql X-1 and (ii) it is likely to be visible only under certain limited conditions of NS-LMXBs. As already mentioned briefly in §6.3, these conclusions motivated us to regard this phenomenon as atomic features of certain heavy elements, because they can be occasionally produced in Type I bursts near the surface of the neutron star, and due to their radioactive decay, they can become invisible on a certain timescale, or buried beneath the fresh metal-poor accreting materials.

7.1.3 Interpretation as atomic features

From the analysis in Chapter 6 and the argument in §7.1.2, the 30 keV hump can be interpreted as a K-shell feature of certain heavy ions. In this chapter, we attempt to identify the corresponding elements, and examine if the interpretation is physically reasonable.

First, let us recall the Moseley's law (see e.g., Hohenemser & Asher 1968), which approximates the K-edge energy of ions of atomic number Z as

$$E_{\rm K} \approx (1+g)^{-1} E_0 (Z-\delta)^2 \ = 33\,[(Z-\delta)/55]^2 \ \ ({\rm keV})\ . \tag{7.1}$$

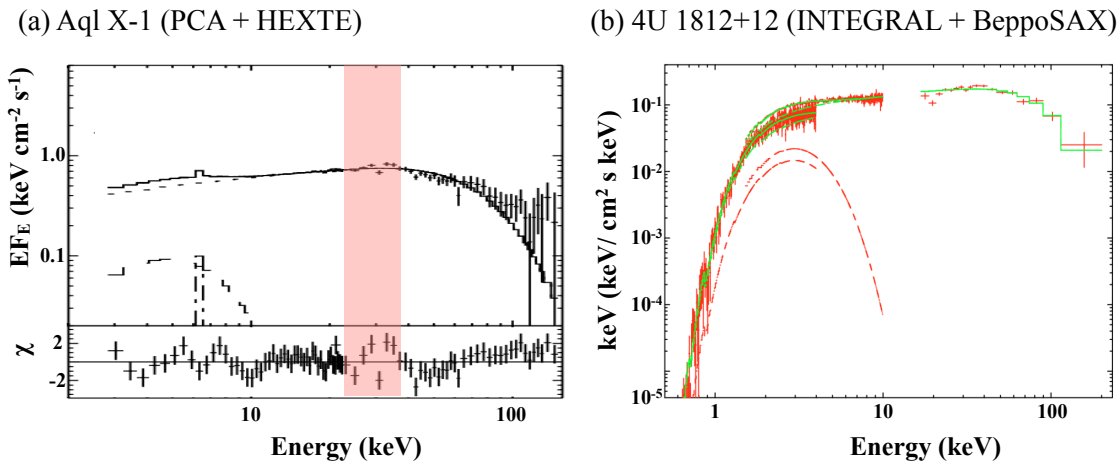

Figure 7.1: (a) *RXTE* spectrum of Aql X-1 (Lin et al., 2007), exhibiting a break at 30 keV. (b) Joint *INTEGRAL* (> 15 keV) and *BeppoSAX* (< 10 keV) spectrum of the LMXB 4U 1812-12 (Tarana et al., 2006). In both panels, the red stripe was added in the present thesis.

Here, $E_0 = 0.0136$ keV is the ionization potential of hydrogen atoms, g is the gravitational redshift on the surface of the neutron star, assumed to be $g = 0.23$ (assuming a mass of 1.4 $M_\odot$ and a radius of 12 km), and δ is a correction factor representing the ionization state: for hydrogen-like ions $\delta = 0$ and for neutral atoms $\delta \simeq 1$. The K_α line energy is approximately $0.75E_K$. From this scaling, the elements with K-edge energies and/or K_α lines at $\sim$30 keV are estimated to have atomic numbers in the range of $Z \simeq$50-60.

Considering solar abundances, the number of heavy elements with such high Z values is extremely low, $\lesssim 2\times10^{-10}$ relative to hydrogen or $\lesssim 5\times10^{-6}$ relative to iron. Therefore, atomic features from such elements normally cannot be observed, because even the Fe–K line (Figure 6.3) has a photon flux of 2.5×10^{-5} ph s^{-1} cm^{-2} (Table 6.7), which is $\sim$60% of the 30-keV structure. Furthermore, the contribution to the Fe–K line in the Aql X-1 spectrum is greater from the fluorescence from the accretion disk, than that from the stellar surface. However, as mentioned in §2.5, a high number of elements with Z of up to $\sim$50 can be synthesized via Type I bursts involving the rp-process, which includes the

conversion of more than 3×10^{-3} (by number) nuclei of the hydrogen-rich accreting matter to elements with an atomic number of $Z \simeq 50$ (Schatz et al., 2001).

These heavy elements, produced slightly below the surface of the neutron star, can be dredged into the atmosphere, possibly via convection or other processes. When the source is in a hard state (§2.2.2), these heavy element atoms are subject to two ionization/excitation processes (Rybicki & Lightman 1985). One process is the bombardment by protons and electrons in the corona that are falling into the atmosphere at a speed which is a fraction of the free-fall velocity. The other process is the irradiation by hard X-ray photons, which are produced when the outgoing blackbody soft X-rays are Compton-scattered back by the coronal electrons. Further details of these processes are given in §7.3.4.

As a consequence of the above processes, the heavy element atoms in the atmosphere can achieve a relatively high ionization state, and produce two types of characteristic X-rays. One type is the emission of K-line (particularly K_α) photons, which occurs when a remaining K-shell electron is collisionally excited into a higher bound energy level. The Gaussian model described in § 6.3.1 can be applied to this condition, and it is further discussed in §7.2. The other type is the production of a recombination quasi-continuum above E_K. As already mentioned in §6.3.2, in our `redge` model this process mostly occurs when a large fraction of the heavy ions are highly photo-ionized by hard X-ray photons, and they recombine with ambient electrons with temperature significantly lower than that of the ionizing photons. Such free electrons can be abundant in the atmosphere, because hydrogen and helium are expected to be nearly completely ionized there by the irradiation by blackbody photons with sub-keV temperature arising from the surface of the neutron star. Furthermore, as confirmed by the `redge` fit (§6.3.2), the ambient electrons are cooler ($kT'_e \simeq 11$ keV; Table 6.7) than the coronal hard X-rays ($kT_e \simeq 55$ keV; Table 6.7). Thus, as already mentioned in §6.3.2, the `redge` model is self-consistent. This scenario is developed in §7.3.

7.1.4 Observable conditions of the 30 keV feature

Assuming that the origin 30 keV feature is atomic, in this section we investigate the condition under which it is detectable. Let us focus on the *Suzaku* data of Aql X-1, and consider the remaining four datasets from the 2007 outburst. However, no suitable constraint is available from Obs. D1, because the object was in a soft state during the observation; thus the intensity at ∼30 keV was an order of magnitude lower than in the

three observations analyzed in Chapter 6 (Figure 3.3 in §3.2.1). This is similar to the case of Obs. D5, when the source was in a hard state, but it was approximately an order of magnitude dimmer than those in the three observations mentioned above. Finally, using the HXD, the signal was undetectable in Obs. D6 and Obs. D7 when the source was the faintest. Thus, no suitable information is available from these four additional *Suzaku* data sets covering the 2007 outburst.

The fact, that the 30-keV feature was present in the 2007 *Suzaku* data of Aql X-1 and those of the same source using *RXTE* (§7.1.2), while it was not detected in the 2011 *Suzaku* data (§6.6) and those acquired in 2016 using *NuSTAR* (§6.7) still needs to be explained. The simplest possibility is that the source was burst active in 2007, and inactive in 2011. However, this is not supported by the seven observations in 2007, which recorded no Type I bursts (Sakurai et al., 2014), whereas the 2011 pointing observation recorded at least nine Type I bursts in a net exposure of ∼30 ks. An alternative possible explanation is as follows. In the merged 2007 spectrum, the Comptonizing corona was relatively thin, with $\tau \simeq 1$ (Table 6.4), but in 2011, when the object was more luminous, the corona was rather thick optically, with $\tau = 3.67 \pm 0.02$ (§6.6), as shown in Figure 6.2. Moreover, in the *NuSTAR* data, the coronal optical depth was obtained as ∼4 (Table 6.8). Thus, in the 2011 *Suzaku* and the *NuSTAR* data, any local spectral feature arising from a vicinity of the surface of the neutron star is possibly smeared to be undetectable, as the photons transferred through the in-falling corona and experience repeated Compton scattering. This interpretation, if correct, supports the view that the 30 keV feature is actually produced at or near the surface of the neutron star.

7.2 Gaussian Modeling

As demonstrated in §6.3.1, the Gaussian model successfully explained the 30 keV feature. In this section, we consider a physical scenario based on this model.

7.2.1 Estimation of the corresponding elements

In Figure 7.2, the solid line and the open squares show the K_α line energies of heavy elements, respectively, as functions of Z, calculated more accurately than that with equation (7.1), assuming $g = 0.23$. Only the neutral (open squares) and H-like (solid line) conditions are shown, because the other ionization states fall between them. The neutral

K_α energies refer to the weighted average of those of $K_{\alpha1}$ and $K_{\alpha2}$, obtained from the X-ray Booklet (Thompson et al., 2009). In the case of H-like ionization state, the $K_{\alpha1}$ and $K_{\alpha2}$ energies were obtained from the AtomDB database (version 3.0.8), and the same intensity ratio as that of neutral atoms was assumed. As the AtomDB database provides the data up to Kr ($Z = 36$) only, the data from $Z = 2$ to $Z = 36$ were fitted by equation

$$E_{\mathrm{K}\alpha}(Z) = a\,(Z - \delta)^c \ \mathrm{eV}, \tag{7.2}$$

which is essentially the same as equation (7.1), but parameters a, δ, and c were not fixed. From this fit we obtained $a = 7.51 \pm 0.03$ which is 3/4 times the value given by equation (7.1), $\delta = -0.033 \pm 0.005$, and $c = 2.015 \pm 0.001$. The results were then extrapolated to $Z > 37$.

The mean value and its error of the Gaussian model, 32^{+2}_{-3} keV (Table 6.7), were considered to represent the K_α emission line energies, and the contributing elements were identified in Figure 7.2 as $Z = 59$–63 or Pr to Eu, regardless of the assumed ionization states. According to the calculation by Schatz et al. (2001), the endpoint of the rp-process is at $Z = 52$ (^{107,108}Te), where further nucleosynthesis is prohibited due to the start of α-decay process. Then, the suggested elements cannot be interpreted as rp-process products; thus the Gaussian model becomes unphysical. However, recent nuclear experiments by Xing et al. (2018) at the RIKEN RI Beam Factory successfully refined the masses of $^{84}_{40}$Zr and $^{84}_{41}$Nb, and updated the structure of the nuclei involved in the rp-process. As a result, the synthesis can proceed beyond the $Z = 52$ endpoint. Thus, the validity of the Gaussian interpretation needs to be verified by the future advances in theoretical and experimental nuclear physics.

7.2.2 Possible origin of the Gaussian width

The intrinsic width of the Gaussian was obtained as 6.0^{+4}_{-2} keV, by considering the HXD-PIN energy resolution ($\sim$3 keV in FWHM; Table 4.1). First, we consider the thermal Doppler effect as the origin of this width, which arises when heavy elements move thermally in the atmosphere of the neutron star. To broaden the 30-keV line by $\sim$6 keV, the element needs to move with a line-of-sight velocity of 20% of the speed of light. The thermal line-of-sight velocity is given by

$$kT = \frac{3}{2}mv^2 \qquad \text{i.e.} \qquad v = \sqrt{\frac{2kT}{3m}}, \tag{7.3}$$

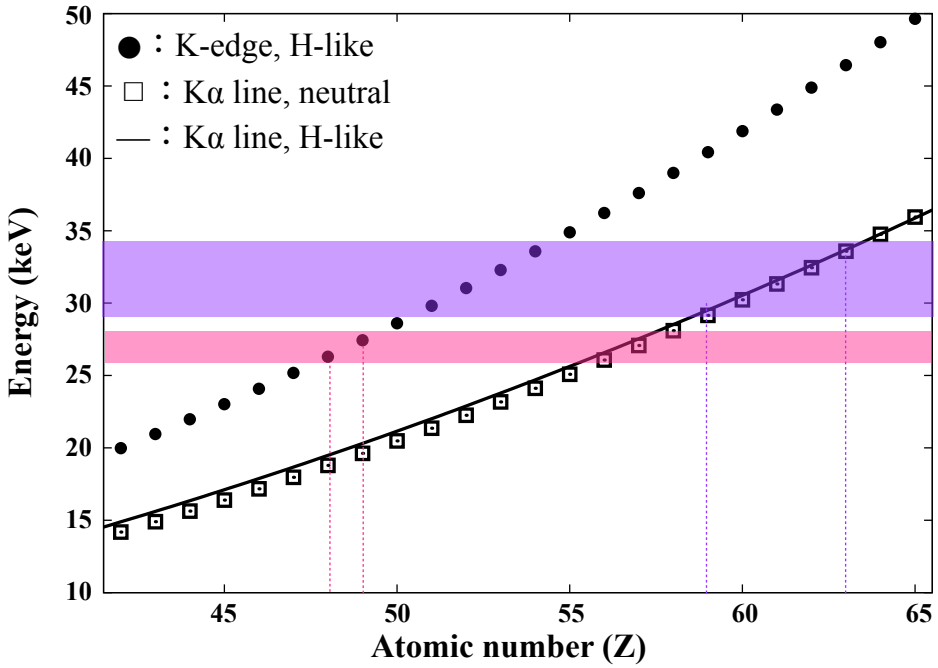

Figure 7.2: Energies of the Kα lines and K-edges of the elements with atomic numbers in the range of Z =40–65, assuming that their production is on the surface of the neutron star, at different ionization states. The constraints from the Gaussian model are indicated by a horizontal purple band and those from the `redge` model are indicated by a horizontal pink stripe.

where m is the mass of the heavy element and T is the temperature of the atmosphere of the neutron star. However, using the approximation of $m \simeq 2Zm_{\rm p}$ and assuming $T \simeq 1$ keV, $v/c = 2.7 \times 10^{-4}(Z/50)^{1/2}$ can be obtained, which is extremely small; therefore, this idea was rejected.

An alternative possibility is line blending because a range of heavy elements can be generated by nucleosynthesis in Type I bursts. For example, the $\rm K_\alpha$ energies of $Z = 61$, $Z = 62$, and $Z = 63$ are 31.3 keV, 32.4 keV, and 33.6 keV, respectively. As the energy difference of these adjacent emission lines of $\sim$1 keV is too narrow to be resolved by the HXD-PIN, which has an energy resolution of $\sim$3 keV, these lines can produce a broad hump as observed. Therefore, line blending can possibly occur.

7.2.3 Possible decay of the 30-keV feature

Assuming that the 30 keV feature results from certain synthesized heavy elements (§7.1.3, §7.1.4) it can become weaker over time due to radioactive decay and/or dilution by the accreting matters. We have examined the possible decay of the feature, using the individual spectra from Obs. D2–D4 presented in §6.1. The EW of the structure for these observations, determined using the Gaussian model and previously presented in Table 6.1, are shown in Figure 7.3 as a function of time (days) following Obs. D2. It is assumed that the EW decreases exponentially with time as

$$EW(t) = EW_0 \exp(-t/\tau_{\rm d}), \tag{7.4}$$

where EW_0 is the initial intensity and $\tau_{\rm d}$ is a decay time constant of the feature. Thus, as previously mentioned in §6.1, the feature is consistently constant. However, decay is also allowed by the data as indicated by the dotted red line in Figure 7.3. Thus, $\tau_{\rm d} > 10$ days can be obtained at 90% confidence interval.

7.3 `redge` modeling

In §6.3.2, the 30keV feature was successfully explained by the `redge` (recombination edge) model as well. In this section, we construct a scenario based on this result.

7.3.1 Estimation of the corresponding elements

In Figure 7.2, the filled circles indicate the K-edge energies of H-like ions as a function of Z, obtained from the NIST web page. Although the edge energy decreases considerably for ions in a low ionization state, we do not consider such case, because K-shell ionization in a low-ionization atom can predominantly result in a K_α line emission, rather than in a recombination with a free electron.

From the K-edge energy and its error (27 ± 1 keV), obtained using the `redge` model (Table 6.7), and assuming a H-like condition, according to Figure 7.2, the corresponding elements can be identified as $Z = 48$ (Cd) and $Z = 49$ (In). As these are lower than the $Z = 52$ endpoint by Schatz et al. (2001), this identification is supported by our current understanding of the rp-process nucleosynthesis in Type I bursts. The rp-process can produce heavy elements around $A \simeq 100$, as reported by Elomaa et al. (2009); thus, our identification is also consistent with their study. Considering the limited energy resolution

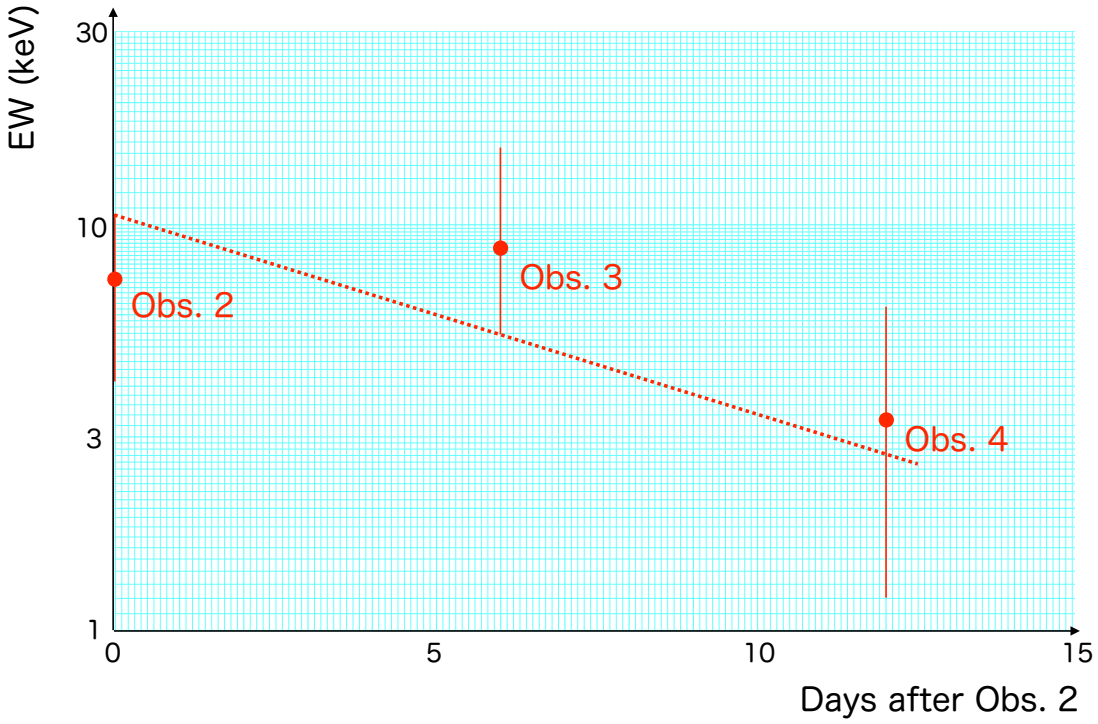

Figure 7.3: EW values of the 30-keV feature (Table 6.1) measured at the three occasions with the Gaussian fitting, plotted as a function of time (days) after Obs. 2. The dashed red line indicates the allowed fastest exponential decay, with $\tau_{\rm d} = 10$ days.

of the HXD-PIN, the 30 keV feature can be possibly attributed to multiple elements near these atomic numbers, rather than to single species. In addition, the obtained free-electron temperature of $kT'_{\rm e} = 11^{+10}_{-5}$ keV (Table 6.7) is a reasonable value in the atmosphere, in the sense that it is between those of the blackbody radiation ($kT_{\rm bb} \simeq 0.23$ keV) and the Comptonizing corona ($kT_{\rm e} \simeq 55$ keV). Therefore, this interpretation is physically more reasonable as the alternative considered in §7.2.

It should be noted, that another possible recombination process is the dielectronic recombination (DR). In the DR process, the energy that becomes available during the capture process is transferred by the excitation of a bound electron to another bound orbit. Then, a photon is emitted that is characteristic to the deexcitation. As there is no bound electron in the fully ionized condition, the DR is negligible. Even under a H-like

condition, the effect of DR is low, because in our case, the electron energy ($\sim$ 11 keV) is significantly smaller than the first excitation energy of 26 keV. Therefore, the contribution of DR is negligible when assuming H-like or fully ionized elements.

7.3.2 Possible presence of a cascade K_α line

In reality, the recombination emission is always accompanied by cascade line. Particularly, the cascade K_α line is expected to appear at an energy of $\simeq (3/4)E_K$ or, in the present case, at $\simeq$ 20 keV, because we obtained $E_K = 27$ keV (Table 6.7). The ratio between the cascade K_α line intensity, and that of the recombination emission, needs to be equal to the ratio between the free-bound transition coefficients to the 2p levels, and that to of the ground state. (Under the assumption of a fully ionized condition, the excitation from the ground state can be neglected.) We calculated these coefficients, assuming that the plasma, dominated by recombination, had a temperature of 10 keV (Table 6.7), and Cd ions were fully ionized. Then, the coefficient to the 2p level was obtained as 4.33×10^{-15} s^{-1}, and that to the ground level was 1.76×10^{-14} s^{-1} (Gu, 2008). Therefore, we expected to observe a cascade K_α line with an intensity of $\sim$1/4 of that of the recombination photons.

To examine the above expectation, we fitted the merged spectrum again, by adding a Gaussian at $\simeq$ 20 keV, to the successful model (the canonical continuum and the `redge` and Gaussian Fe–K line) described previously (§6.3.2). Then, as shown in Figure 7.4, a reasonable fit was obtained. Although the quality of the fit slightly improved from χ^2/dof = 220.56/216 to 216.89/214, the continuum and `redge` parameters did not change significantly compared with the result in §6.3.2. The Gaussian energy was obtained at 20^{+1}_{-2} keV as expected, with a marginally positive flux of $(8.3^{+7.3}_{-7.0})\times10^{-5}$ photons cm^{-2} s^{-1}. Compared with the `redge` flux of $(6.0^{+2.7}_{-2.0}) \times 10^{-4}$ photons cm^{-2} s^{-1}, this implies an intensity ratio of $0.14^{+0.24}_{-0.02}$,which is consistent with the expected value of 1 : 4. Therefore, the data are consistent with the expected presence of the cascade K_α line.

7.3.3 Possible geometry of the emission region

Figure 7.5 shows a possible geometry around the neutron star in Aql X-1. The surface of the neutron star can be regarded as an emitter of primary X-rays, specifically, blackbody radiation with a temperature of $kT_{\rm bb} \simeq 0.5$ keV. We assume that the surface of the neutron star is surrounded by an atmosphere, which is sustained in the hydrostatic equilibrium

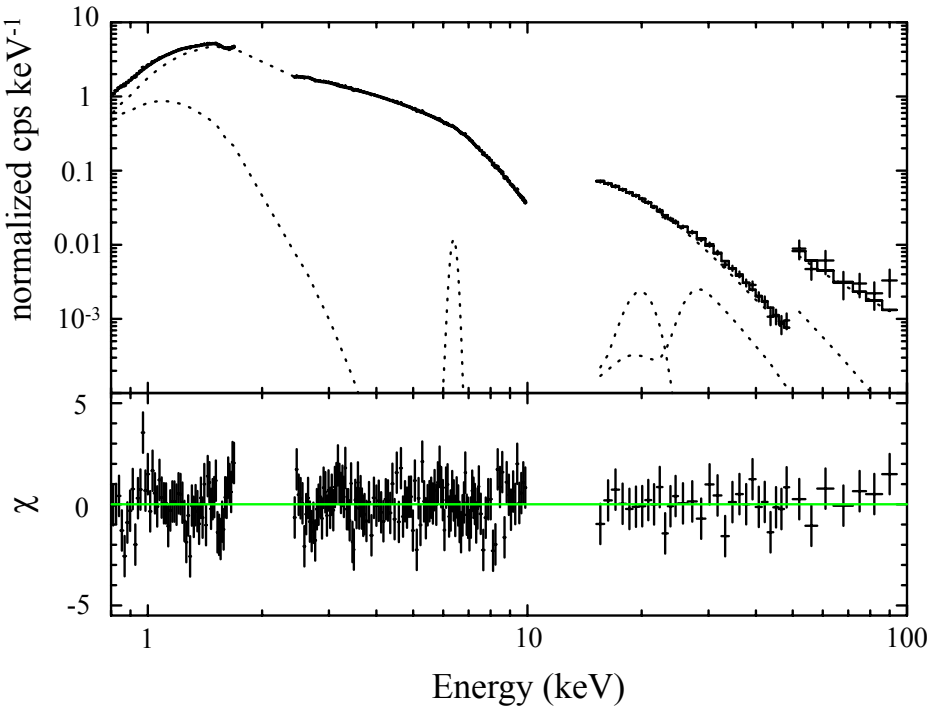

Figure 7.4: Merged spectrum and fitting, similar to that shown in Figure 6.6(b), but an additional Gaussian was introduced at $\simeq$ 20 keV to represent the cascade K_{alpha} line. Its intensity and central energy were not fixed (see text).

with a temperature of $kT'_{\rm e} \simeq 11$ keV. The surface of the neutron star is partially (or spherically) covered by the coronal accretion flow ($kT_{\rm e} \simeq 55$ keV and $\tau \simeq 1$ obtained from Table 6.7). The blackbody photons from the surface of the neutron star are Comptonized by the coronal electrons, and converted into a hard X-ray continuum of up to $\sim$100 keV. Although some Comptonized photons are directly detected by the observer, part of the photons illuminate the neutron star atmosphere. Thus, the atmosphere, which consists of accreted hydrogen and synthesized heavy elements, is expected to be highly ionized (see §7.3.4 for details). Then, the heavy ions capture the free electron, and emit the recombination photons, which form spectral hump above $E_{\rm K} \simeq 27$ keV.

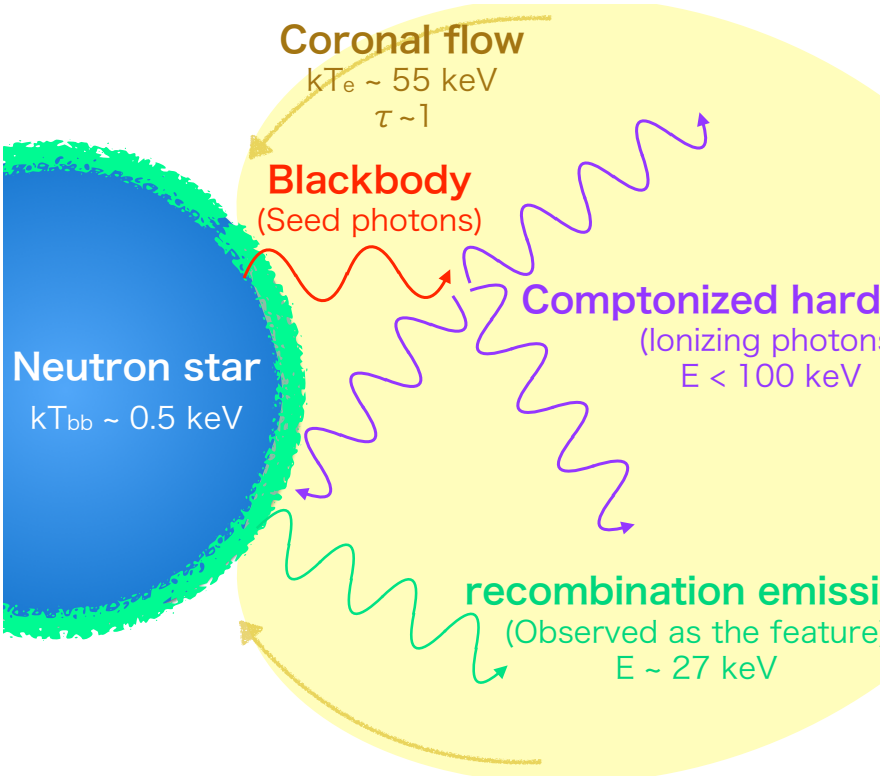

Figure 7.5: Possible geometry around the neutron star. The blue and yellow regions indicate the neutron star and the corona, respectively. The light green circle around the neutron star represents the atmosphere. The red and green waves indicate the blackbody emission (seed photons for Comptonization) and the recombination emission, respectively. The purple waves represent the Comptonized X-rays (ionizing photons).

7.3.4 Amount of heavy elements

In § 7.3.1, the 30 keV feature was tentatively identified with a recombination quasi-continuum, produced in the atmosphere of the neutron star by highly-ionized Cd or In ions. A possible presence of the accompanying K_α cascade line was also confirmed. Furthermore, the geometry of the emission region is defined in Figure 7.5. However, to observe an atomic feature of such rare elements at all, they need to be condensed by several orders of magnitude with respect to their solar abundances (§ 7.1.3). In the following, we examine this important issue from various aspects. For simplicity, it is assumed that the element is Cd ($Z = 48$).

Assumptions for the analysis

Figure 7.6 shows various conditions on a plane of $(n_{\rm H}, n_{\rm x})$, where $n_{\rm H}$ and $n_{\rm x}$ denotes the number densities of protons and Cd ions in the atmosphere, respectively. The Cd abundances of 10^5 and 10^7 times the solar value ($\sim 10^{-10}$ with respect to the number of hydrogens) are indicated by gray lines. Furthermore, for simplicity, we employ the following assumptions.

1. The atmosphere of the neutron star consists of only electrons, protons, and Cd ions. The average ion mass is given by

$$m_{\rm i} = m_{\rm p} \left(\frac{104 n_{\rm x} + n_{\rm H}}{n_{\rm x} + n_{\rm H}} \right), \tag{7.5}$$

   where 104 is most abundant mass number reported in Schatz et al. (2001).

2. The ions are fully ionized; thus, the number density of the electrons can be described as

$$n_{\rm e} = 48 n_{\rm x} + n_{\rm H} \ . \tag{7.6}$$

   In Figure 7.6, the condition of $n_{\rm H} = 48 n_{\rm x}$ is indicated by the green line.

3. The atmosphere of the neutron star is isothermal, with a temperature of $kT'_{\rm e} \simeq 11$ keV as indicated by the `redge` fit (Table 6.7), and has an exponential density distribution with a scale height of

$$H = \frac{kT'_{\rm e}}{m_{\rm i} g} \sim \frac{m_{\rm p}}{m_{\rm i}} \times 80 \ \ {\rm cm} \sim \frac{n_{\rm x} + n_{\rm H}}{104 n_{\rm x} + n_{\rm H}} \times 80 \ \ {\rm cm}. \tag{7.7}$$

   Here, $g \equiv G M_{\rm NS} / R_{\rm NS}^2$ is the gravitational acceleration on the surface and $m_{\rm i}/m_{\rm p}$ was substituted by equation (7.5). If $n_{\rm H} \gg 104 n_{\rm x}$ then $H \simeq 80$ cm, while $n_{\rm H} \ll 112 n_{\rm x}$ gives $H \simeq 0.8$ cm.

4. The recombination feature arise in a region above a certain height in the atmosphere, with $n_{\rm H}$, $n_{\rm x}$, and $n_{\rm e}$ refer to the densities at that height.

Required volume emission measure

The number of recombination photons, emitted in all energies, E, above the ionization potential I, per unit time per unit energy, from a recombining plasma with a volume V, can be expressed as

$$\Phi_{\rm rec} = n_{\rm x} n_{\rm e} V \int_I^{+\infty} S(E) dE \ . \tag{7.8}$$

Here, the quantity $n_{\rm x} n_{\rm e} V$ is known as the volume emission measure (VEM), and the factor S (photon/volume/time/energy), which is the spectral emissivity divided by the VEM, is given by (Mewe, 1994)

$$S(E) = \frac{\sqrt{2} E^2 g_{\rm n} \sigma_{\rm bf}}{\sqrt{\pi} (m_{\rm e} kT)^{3/2} c^2} \exp\left(\frac{I-E}{kT}\right), \tag{7.9}$$

where $g_{\rm n} = 2$ is the statistical weight of the recombining level (1s level), $kT \simeq 11$ keV is the electron temperature, and $I \simeq 27$ keV (= K-edge energy). The recombination cross section $\sigma_{\rm bf}$ can be written as (Mewe, 1994)

$$\sigma_{\rm bf} = 1.1 \times 10^5 \frac{I^2 g_{\rm bf}}{n E^3} \times 10^{-24} \ {\rm cm}^2 \sim 0.8 \times 10^{-21} \ {\rm cm}^{-2}, \tag{7.10}$$

where n is the principal quantum number ($n = 1$ in the present case), $g_{\rm n} = 0.2$ is the Gaunt factor (Karzas & Latter, 1961), E and I are in units of keV, and $E = I$ was assumed. From these values, equation (7.9) can be written in units of cm^3 s^{-1} keV^{-1} as

$$S(E) = 6.6 \times 10^{-14} \exp\left(\frac{I-E}{kT}\right), \tag{7.11}$$

where the approximation $E \sim I$ is assumed again. As integrating the exponential factor is equivalent to a simple multiplication by $kT \simeq 11$ keV, equation (7.8) finally becomes

$$\Phi_{\rm rec} = n_{\rm x} n_{\rm e} V \times 7 \times 10^{-13} \ {\rm ph \ cm^3 \ sec^{-1}} \ . \tag{7.12}$$

A more rigorous calculation by Badnell (2006) gives a slightly lager value of

$$\Phi_{\rm rec} = n_{\rm x} n_{\rm e} V \times 5 \times 10^{-12} \ {\rm ph \ cm^3 \ sec^{-1}}, \tag{7.13}$$

which is adopted hereafter.

In our observations, the recombination flux $F(E)$ was measured at the Earth as

$$\Phi / 4\pi D^2 = F(E) = 5.0 \times 10^{-4} \ {\rm ph \ cm^{-2} s^{-1}}, \tag{7.14}$$

where $D = 5.2$ kpc is the distance to the source. Therefore, the following observational constraint can be obtained:

$$\Phi = 4\pi F(E) D^2 = 1.6 \times 10^{42} \ {\rm ph \ s^{-1}} \ . \tag{7.15}$$

By combining equation (7.13) and equation (7.15), the required VEM can be obtained as

$$n_{\rm x} n_{\rm e} V \sim 3 \times 10^{53} \ {\rm cm^{-3}} \ . \tag{7.16}$$

Assuming that half the atmosphere is occulted by the neutron star, the emitting volume in the atmosphere can be expressed as $V = 2\pi R_{\rm NS}^2 H = 9 \times 10^{12} H$ cm^3. Finally, the following condition can be obtained:

$$n_{\rm x} n_{\rm e} H \sim 5 \times 10^{40} \text{ cm}^{-5} . \tag{7.17}$$

Using equation (7.6) and equation (7.7), the constraint in equation (7.17) can be rewritten as

$$\frac{n_{\rm x}(n_{\rm H} + n_{\rm x})(n_{\rm H} + 48 n_{\rm x})}{n_{\rm H} + 104 n_{\rm x}} = 7 \times 10^{38} \text{ cm}^{-6}. \tag{7.18}$$

In Figure 7.6, the constraint in equation (7.17) with a rather complex behavior, is indicated by the red stripe. Nevertheless, its asymptotic forms can be easily understood. When $48 n_{\rm x} \ll n_{\rm H}$, specifically, the electrons are dominated by those from hydrogen, then

$$n_{\rm H} n_{\rm x} = 7 \times 10^{38} \text{ cm}^{-6}, \tag{7.19}$$

which is represented by the straight section of the red stripe toward the larger $n_{\rm H}$ and smaller $n_{\rm x}$. In contrast, when $48 n_{\rm x} \gg n_{\rm H}$, then

$$n_{\rm x} = 4 \times 10^{19} \text{ cm}^{-3} . \tag{7.20}$$

This corresponds to the flat section of the red stripe toward the smaller $n_{\rm H}$.

Ionization of cadmium

In the `redge` model, the heavy elements are required to be highly ionized. Therefore, the ionization parameter ξ required to satisfy the condition

$$\xi \equiv L_{\rm ill}/n_{\rm e} r^2 > 10^3, \tag{7.21}$$

where $L_{\rm ill} \simeq 1 \times 10^{36}$ erg s^{-1} is the illuminating luminosity above the K-edge energy of 27 keV (Table 6.7) and r is the distance from the illuminating source, which is assumed to be $r \simeq R_{\rm NS} = 10^6$ cm. (Under real conditions, r can be greater, but the corona and the stellar surface are more parallel to each other than the spherical configuration assumed in equation (7.21), suggesting that r can be effectively smaller than $R_{\rm NS}$.) Therefore, this condition reduces to

$$n_{\rm e} < 1 \times 10^{21} \text{ cm}^{-3} . \tag{7.22}$$

When combined with equation (7.6), the region allowed by this constraint is indicated by the blue shaded rectangle in Figure 7.6, which completely intersects with the red stripe.

Thomson optical depth

To observe the photons emitted from the heavy ions, the atmosphere above that optical depth needs to be optically thin against Thomson (Compton) scattering. Using the Thomson cross section in equation (2.20), specifically, $\sigma_{\rm T} = 6.65 \times 10^{-25}$ cm^2, this condition can be expressed as

$$\sigma_{\rm T}\, n_{\rm e}\, H < 1 \quad \rightarrow \quad n_{\rm e} H < 1.5 \times 10^{24}\ {\rm cm}^{-2}\ . \tag{7.23}$$

By combination equation (7.23) with equations (7.6) and (7.7), this condition can be rewritten as

$$(48 n_{\rm x} + n_{\rm H})(n_{\rm x} + n_{\rm H})/(104 n_{\rm x} + n_{\rm H}) < 2 \times 10^{22}\ {\rm cm}^{-3}\ . \tag{7.24}$$

As shown in Figure 7.6, in the purple area, the region that satisfies this condition includes that for the Cadmium ionization. For reference, its boundaries are given as $n_{\rm H} < 2 \times 10^{22}$ cm^{-3} and $n_{\rm x} < 5 \times 10^{22}$ cm^{-3}.

Self-absorption

Even when equation (7.22) is satisfied, a certain fraction of the Cd ions can remain in a H-like state instead of complete ionization, and their remaining K-shell electrons can absorb the recombination photons. To prevent this self-absorption, $n_{\rm x}$ needs to satisfy the condition of

$$\tau_{\rm pe} = n_{\rm x} \sigma_{\rm pe} H < 1, \tag{7.25}$$

where $\sigma_{\rm pe} = 3 \times 10^{-21}$ cm^2 is the photoelectric absorption coefficient for $Z = 48$ (Noguchi, 1987). Using equation (7.7), equation (7.25) can be rewritten as

$$\frac{n_{\rm x}(n_{\rm x} + n_{\rm H})}{104 n_{\rm x} + n_{\rm H}} < 4 \times 10^{18}\ {\rm cm}^{-3}\ . \tag{7.26}$$

When $48 n_{\rm x} \ll n_{\rm H}$, this condition reduces to $n_{\rm x} < 4 \times 10^{18}$ cm^{-3}. In contrast, if $48 n_{\rm x} \gg n_{\rm H}$, equation (7.26) becomes $n_{\rm x} < 4 \times 10^{20}$ cm^{-3}. This condition is illustrated in Figure 7.6 represented by the gray region.

Summay

As shown in Figure 7.6, so far four requirements have been considered; the VEM required to explain the observed recombination signal intensity, the condition for high ionization, and the requirement for a low Thomson optical depth and that for a negligible

self-absorption. Although it is relatively narrow, a common region can be found among them, at $n_{\rm H} \sim 3 \times 10^{20}$ cm^{-2} and $n_{\rm x} \sim 1 \times 10^{18}$ cm^{-2}. This condition can be expressed in the following mutually equivalent forms.

1. Cd has an approximately seven orders of magnitude higher abundance than the solar value.
2. The total mass of Cd in the atmosphere is 30% of that of H.
3. In terms of number densities, protons are still three orders of magnitude more abundant, than Cd ions.
4. The atmospheric electrons are still dominated by those from hydrogen.

If this set of conditions is satisfied in the atmosphere of the neutron star, the 30 keV structure can be consistently explained as K-shell features of the products of the rp-process. Although the condition shown in Figure 7.6 appear to be extreme, a single Type-I burst can convert nearly $\sim 10^{20}$ g of hydrogen-rich accreting matter into heavier elements, which corresponds to an accumulation time of accreting matter of $\sim 10^5$ s. Furthermore, as shown in Figure 7.7, nearly 30% of the accreting mass ($\sim 0.3\%$ in the number of elements) is converted to the heavy elements via Type-I bursts with $A \simeq 100$ ($Z \simeq 48$). Therefore, the surface of the neutron star of a burst-active LMXB can be covered by a thick matter of these heavy elements, and the in-falling matter can wind them up into the atmosphere. Therefore, the assumption that the atmosphere consists of hydrogen and cadmium is not unrealistic. As indicated by the dotted yellow line in Figure 7.6, the composition of burst products, as calculated by Schatz et al. (2001), is in the region of consistency as identified above.

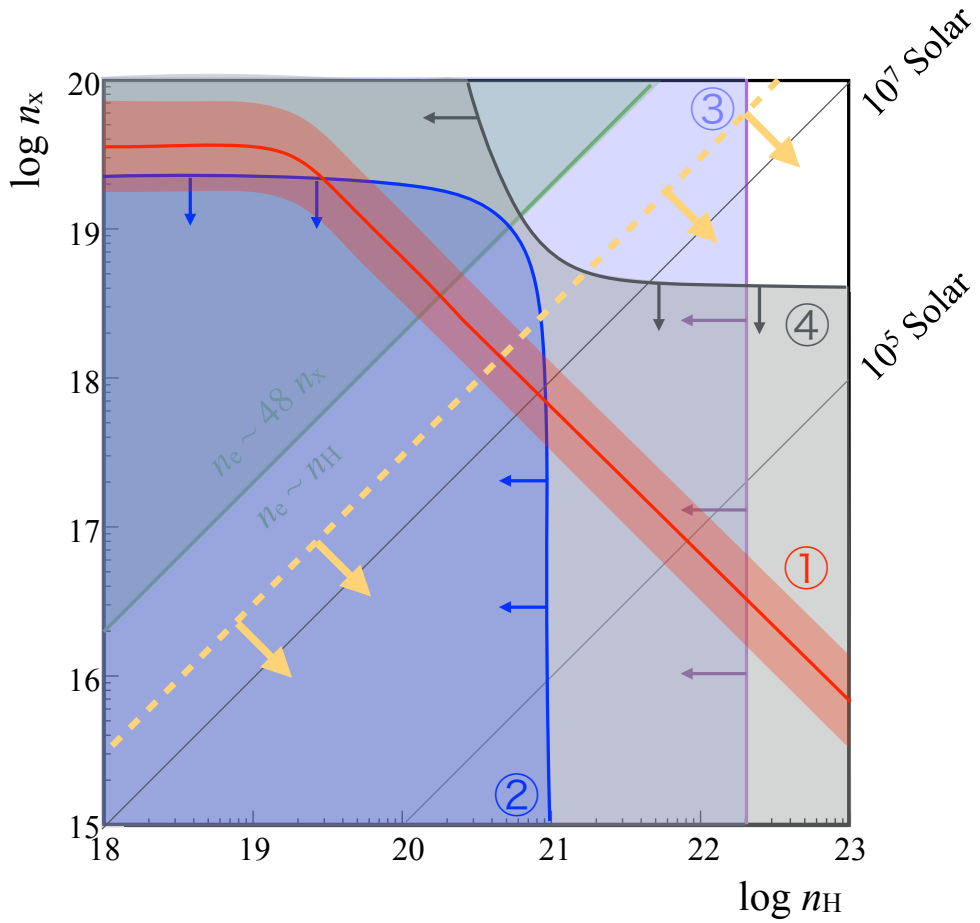

Figure 7.6: Diagram of hydrogen number density, $n_{\rm H}$, as a function that of Cd, $n_{\rm x}$, in the atmosphere of the neutron star. The pair of gray lines represent 10^7 and 10^5 times the solar abundance of Cd. On the green line, the same number of electrons is supplied by H and Cd. The red stripe [denoted by (1)] indicates the VEM of equation (7.17), required to explain the observed flux of the recombination photons. In the blue [denoted by (2)] and purple hatched [denoted by (3)] regions, the conditions for high ionization [equation (7.22)] and low Thomson optical depth [equation (7.24)] are satisfied, respectively. In the gray shaded regions [denoted by (4)], the condition for low self-absorption, equation (7.26), is satisfied. The dashed yellow line indicates the final composition of the Type I bursts, as the calculated result from Schatz et al. (2001) and as shown in Figure 7.5.

7.3.5 Radioactive decays of possible nuclear species

So far, the relevant elements have been identified as Cd and In (§7.3.1), which can be synthesized via the rp-process, and the necessary abundance of these elements has been quantified (§7.3.4). However, such nuclear species are typically unstable because they are proton-enriched. Thus, we need to investigate if any Cd or In isotopes have sufficiently long lifetimes to enable their detection even a few days after the latest Type-I burst.

First, we examine this issue based on the theoretical work by Schatz et al. (2001). As shown in Figure 7.7, their calculation demonstrates that the long-lived isotope ^{104}Sn ($\tau_{\rm d} = 20.8$ sec) is the most abundant element created via the rp-process in X-ray bursts. The decay path from ^{104}Sn is shown in Figure 7.8. Thus, under typical conditions, this isotope decays to the stable nuclide of ^{104}Pd via successive electron capture (EC) processes in a few hours. In an EC capture process, a proton-rich nucleus mainly captures its K-shell electron, and one proton in the nucleus replaces a neutron; thus, the atomic number decreases as $Z \rightarrow Z-1$. However, if the Cd and/or In atoms are highly ionized, such that most of them have no K-shell electrons, the EC decay needs to be delayed considerably (see e.g., Mochizuki, 2001). Considering such an extreme condition, nuclear species of Cd and In could have possibly survived the decay until the *Suzaku* observations.

Alternatively, we may put aside the current theoretical calculation by Schatz et al. (2001), and examine other possible nuclides. The possible stable or long-lived nuclides are ^{113}In (stable with natural abundance of 4.3%), ^{109}Cd ($\tau_{\rm d}$ =462.6 days), ^{110}Cd (stable with natural abundance of 12.49%), and ^{111}Cd (stable with natural abundance of 12.80%). These species, shown in Figure 7.9 with red frames, can be produced as a result of EC decay of those nuclear species, indicated by the shaded cyan region in Figure 7.9. Therefore, if the rp-process proceeds up to atomic numbers of $A \simeq 110$ instead of the currently suggested $A = 104$, the EC sequence can proceed through the blue dashed regions, to reach the possible stable/long-lived nuclides. The validity of this scenario needs to be verified by future theoretical and experimental studies in nuclear physics.

7.4 Problems to be solved

The present study is strongly support our initial conjecture, that the 30 keV feature, observed in the *Suzaku* spectra of Aql X-1, is a radiative recombination feature of heavy elements (most likely Cd or In) synthesized via the rp-process. However, there are still

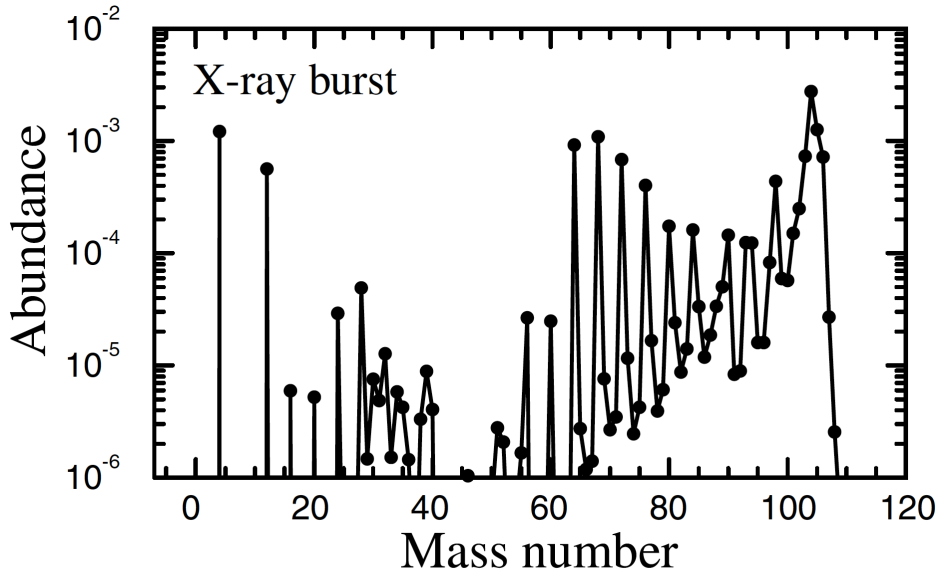

Figure 7.7: Final abundance distribution in fractional ionic number from Type I bursts, theoretically calculated considering the rp-process and shown as a function of the mass number (obtained from Schatz et al. 2001).

several open problems, which need to be addressed in future studies to achieve a more convincing scenario.

1. One open problem, if a Type I burst can really produce a sufficient number of contributing elements to satisfy the condition shown in Figure 7.6, as calculated by Schatz et al. (2001).

2. A further question is the mechanism that sustain the synthesized ions for a sufficiently long time (e.g., days to weeks), against dilution by the accreting hydrogen-rich materials and radioactive decay.

3. In addition, although their actual height above the surface of the neutron star is not known, the effect lifting up the elements up to the upper layer of the atmosphere against the strong gravity, where the condition of Figure 7.6 is satisfied, have still not understood. We can consider such effect as strong turbulence in the atmosphere resulting from the accretion stream and convection due to the Type-I bursts. Furthermore, these heavy ions can be lifted up by strong radial electric fields, which can

be produced in the atmosphere when the electrons in the in-falling accretion stream are decelerated more strongly (due to Coulomb scattering and radiation force) than protons.

Based on observations, the above problems could be addressed by a suitable NS-LMXB measurement for a relatively long ($\sim$ 1 week) period, and by establishing a correlation between its Type-I burst frequency and the strength of the 30-keV feature.

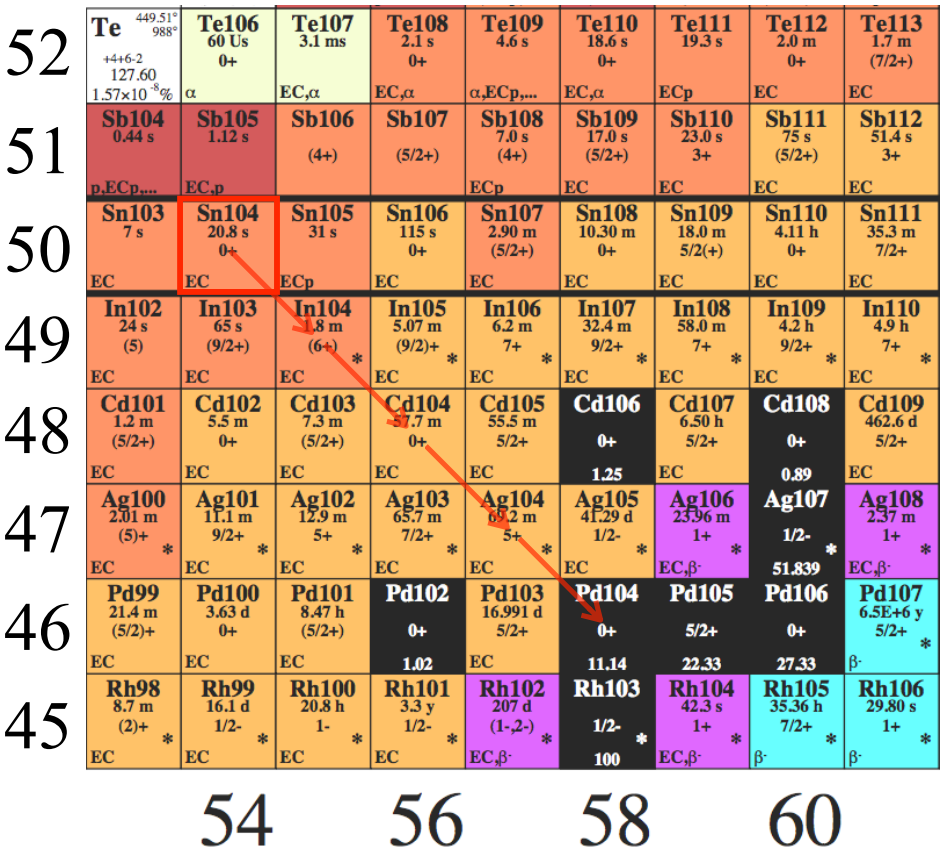

Figure 7.8: Decay path of ^{104}Sn on the nuclear chart, consisting of a chain of EC reactions indicated by red arrows. The abscissa shows the number of neutrons, and the ordinate shows the number of protons. The red arrows indicate individual EC decays. The nuclides in black are stable, those in orange decay via EC, those in purple via EC or β^+ decay, and those in cyan via β^- decay.

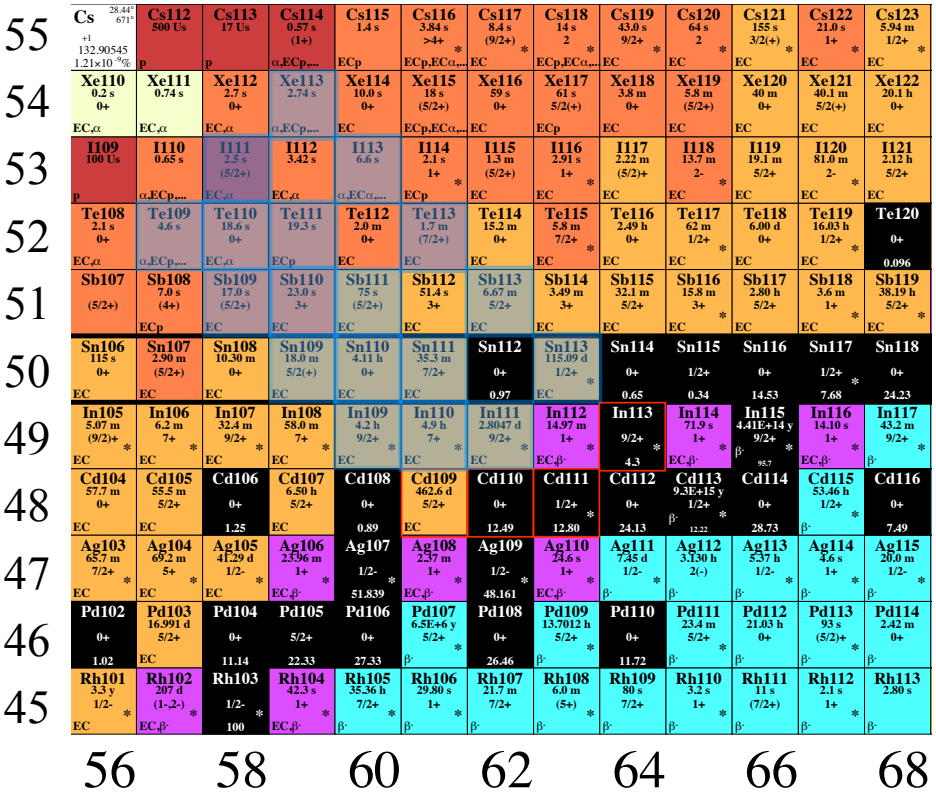

Figure 7.9: Possible nuclear species indicated by the blue meshed regions. Nuclear species with red outlines are stable or long lived Cd and In isotopes, which can explain the sustained 30 keV feature. Isotopes with blue shades indicate possible EC-decay sequences toward the stable/long-lived nuclear species. The horizontal and vertical axes are the same as in Figure 7.8.

Chapter 8

Summary and Conclusions

In the present thesis, we analyzed the archival *Suzaku* spectra of Aql X-1 obtained from September to October, 2007, to confirm and assess the spectral feature around 30 keV described in Sakurai et al. (2012). In this chapter, the results of our analysis are summarized.

The 30-keV feature was detected positively in three spectra, obtained with an interval of $\sim$6 days. The center energy and EW were consistent among them, and any intensity decay was constrained to time constants of > 10 days. Using the merged spectrum, we confirmed that the feature was statistically significant with a false probability of 3×10^{-4}, and it was also significant against various systematic effects, including instrumental uncertainties and tolerance in the continuum modeling. Thus, we have successfully confirmed the suggestion put forth by Sakurai et al. (2012).

Combined with the canonical continuum model, the feature was successfully represented by a Gaussian component centered at $\sim$32 keV, with an EW of $\sim$9 keV. Alternatively, the feature was also represented by the `redge` (recombination-edge) model, with a K-edge energy of $\sim$27 keV and an electron temperature of $\sim$11 keV. In the former and latter interpretations, the elements were extimated as Z =59–64 (Pr–Eu), and Z =48 (Cd) and Z =49 (In), respectively, when assuming a gravitational redshift of $g = 0.23$.

As heavy elements, such as $Z \simeq$48–64, are extremely rare in ordinary materials of solar abundances, we concluded that these elements have been synthesized in Aql X-1 via the rp-process during the Type-I bursts. According to the theoretical calculations by Schatz et al. 2001, Fisker et al. 2008, and Elomaa et al. 2009, the rp-process can produce heavy elements around $Z \simeq 50$ or lower. Therefore, the `redge` interpretation is consistent with the current theoretical approaches; however, the Gaussian interpretation is rather difficult,

unless the rp-process reaction chain is significantly updated.

The 30 keV feature has been identified with a recombination emission, produced in the atmosphere of the neutron star by highly-ionized Cd or In ions. To examine the required amount of the relevant elements, we considered four requirements: the VEM required to explain the observed intensity of the feature, the condition for high ionization, and the requirement of a low Thomson optical depth and that of a low self-absorption. From the above conditions, the required amount of Cd is approximately seven orders of magnitude higher than the solar abundance value. The composition of the burst products calculated by Schatz et al. (2001) is consistent with our prediction. Therefore, the present results provide the first insight of the rp-process in the atmosphere of a neutron star.

Bibliography

Armas Padilla, M., Ueda, Y., Hori, T., Shidatsu, M., & Muñoz-Darias, T. 2017, MNRAS, 467, 290

Baade, W., & Zwicky, F. 1934, Contributions from the Mount Wilson Observatory, vol. 3, pp.73-78, 3, 73

Badnell, N. R. 2006, ApJS, 167, 334

Boella, G., Butler, R. C., Perola, G. C., et al. 1997, A&AS, 122, 299

Boldt, E. 1987, in IAU Symposium, Vol. 124, Observational Cosmology, ed. A. Hewitt, G. Burbidge, & L. Z. Fang, 611–615

Cannizzo, J. K. 1993, ApJ, 419, 318

Cannizzo, J. K. 1998, in Astronomical Society of the Pacific Conference Series, Vol. 137, Wild Stars in the Old West, ed. S. Howell, E. Kuulkers, & C. Woodward, 308

Casella, P., Altamirano, D., Patruno, A., Wijnands, R., & van der Klis, M. 2008, ApJL, 674, L41

Chen, C. M. H., Boggs, S. E., Bolotnikov, A. E., et al. 2002, IEEE Transactions on Nuclear Science, 49, 270

Chen, Y.-P., Zhang, S., Zhang, S.-N., et al. 2013, ApJL, 777, L9

Chevalier, C., Ilovaisky, S. A., Leisy, P., & Patat, F. 1999, A&A, 347, L51

Czerny, M., Czerny, B., & Grindlay, J. E. 1987, ApJ, 312, 122

Demorest, P. B., Pennucci, T., Ransom, S. M., Roberts, M. S. E., & Hessels, J. W. T. 2010, Nature, 467, 1081

Done, C., & Kubota, A. 2006, MNRAS, 371, 1216

Elomaa, V.-V., Vorobjev, G. K., Kankainen, A., et al. 2009, Physical Review Letters, 102, 252501

Fisker, J. L., Schatz, H., & Thielemann, F.-K. 2008, ApJS, 174, 261

Forman, W., Jones, C., Cominsky, L., et al. 1978, ApJS, 38, 357

Fujimoto, M. Y., Hanawa, T., Iben, Jr., I., & Richardson, M. B. 1987, ApJ, 315, 198

Fujimoto, M. Y., Hanawa, T., & Miyaji, S. 1981, ApJ, 247, 267

Fukazawa, Y., Mizuno, T., Watanabe, S., et al. 2009, PASJ, 61, S17

García, J., Dauser, T., Lohfink, A., et al. 2014, ApJ, 782, 76

Giacconi, R., Gursky, H., Kellogg, E., Schreier, E., & Tananbaum, H. 1971, ApJL, 167, L67

Giacconi, R., Gursky, H., Paolini, F. R., & Rossi, B. B. 1962, Physical Review Letters, 9, 439

Glendenning, N. K., & Schaffner-Bielich, J. 1998, Physical Review Letters, 81, 4564

Grindlay, J., Gursky, H., Schnopper, H., et al. 1976, ApJL, 205, L127

Gu, M. F. 2008, Canadian Journal of Physics, 86, 675

Hailey, C. J., An, H., Blaedel, K. L., et al. 2010, in Proc. SPIE, Vol. 7732, Space Telescopes and Instrumentation 2010: Ultraviolet to Gamma Ray, 77320T

Hanawa, T., Sugimoto, D., & Hashimoto, M.-A. 1983, PASJ, 35, 491

Hanke, M. 2011, PhD thesis, Dr. Karl Remeis-Sternwarte, Astronomisches Institut der Universität Erlangen-Nürnberg, Sternwartstr. 7, 96049 Bamberg, Germany

Harrison, F. A., Boggs, S., Christensen, F., et al. 2010, ArXiv e-prints, arXiv:1008.1362

Harrison, F. A., Craig, W. W., Christensen, F. E., et al. 2013, ApJ, 770, 103

Hohenemser, C., & Asher, I. M. 1968, American Journal of Physics, 36, 882

Iaria, R., Di Salvo, T., D'Aì, A., et al. 2013, A&A, 549, A33

Inoue, H., Koyama, K., Makishima, K., et al. 1981, ApJL, 250, L71

in't Zand, J. J. M., & Weinberg, N. N. 2010, A&A, 520, A81

Iwakiri, W. B., Terada, Y., Mihara, T., et al. 2012, ApJ, 751, 35

Jonker, P. G., & Nelemans, G. 2004, MNRAS, 354, 355

José, J., Moreno, F., Parikh, A., & Iliadis, C. 2010, ApJS, 189, 204

Kajava, J. J. E., Nättilä, J., Poutanen, J., et al. 2017, MNRAS, 464, L6

Keek, L., Ballantyne, D. R., Kuulkers, E., & Strohmayer, T. E. 2014, ApJL, 797, L23

Keek, L., in't Zand, J. J. M., Kuulkers, E., et al. 2008, A&A, 479, 177

Kelley, R. L., Mitsuda, K., Allen, C. A., et al. 2007, PASJ, 59, 77

Kerr, F. J., & Lynden-Bell, D. 1986, MNRAS, 221, 1023

Kitaguchi, T. 2009, Phd thesis, University of Tokyo

Kitaguchi, T., Grefenstette, B. W., Harrison, F. A., et al. 2011, in Proc. SPIE, Vol. 8145, Society of Photo-Optical Instrumentation Engineers (SPIE) Conference Series, 814507

Kitamoto, S., Tsunemi, H., Miyamoto, S., & Roussel-Dupre, D. 1993, ApJ, 403, 315

Kokubun, M., Makishima, K., Takahashi, T., et al. 2007, PASJ, 59, 53

Kondo, I., Inoue, H., Koyama, K., et al. 1981, Space Science Instrumentation, 5, 211

Koyama, K., Inoue, H., Makishima, K., et al. 1981, ApJL, 247, L27

Koyama, K., Tsunemi, H., Dotani, T., et al. 2007, PASJ, 59, 23

Kubota, A., & Makishima, K. 2004, ApJ, 601, 428

Kunte, P. K., Durgaprasad, N., Gokhale, G. S., et al. 1973, Nature Physical Science, 245, 37

Lattimer, J. M., & Prakash, M. 2001, ApJ, 550, 426

Lightman, A. P., & Zdziarski, A. A. 1987, ApJ, 319, 643

Lin, D., Remillard, R. A., & Homan, J. 2007, The Astrophysical Journal, 667, 1073. http://stacks.iop.org/0004-637X/667/i=2/a=1073

Lin, D., Remillard, R. A., & Homan, J. 2010, ApJ, 719, 1350

Magdziarz, P., & Zdziarski, A. A. 1995, MNRAS, 273, 837

Makino, F., & ASTRO-C Team. 1987, Astrophys. Lett., 25, 223

Makishima, K., Maejima, Y., Mitsuda, K., et al. 1986, ApJ, 308, 635

Mata Sánchez, D., Muñoz-Darias, T., Casares, J., & Jiménez-Ibarra, F. 2017, MNRAS, 464, L41

Mewe, R., K. J. S. 1994, Continuum Radiation Process, Tech. rep., SRON, August

Mitsuda, K., Inoue, H., Koyama, K., et al. 1984, PASJ, 36, 741

Mitsuda, K., Bautz, M., Inoue, H., et al. 2007, PASJ, 59, 1

Noguchi, M. 1987, RADIOISOTOPES, 36, 49

Ono, K., Makishima, K., Sakurai, S., et al. 2017, PASJ, 69, 23

Ono, K., Sakurai, S., Zhang, Z., Nakazawa, K., & Makishima, K. 2016, PASJ, 68, S14

Osaki, Y. 1974, PASJ, 26, 429

—. 1996, PASP, 108, 39

Poutanen, J., & Svensson, R. 1996, ApJ, 470, 249

Protassov, R., van Dyk, D. A., Connors, A., Kashyap, V. L., & Siemiginowska, A. 2002, ApJ, 571, 545

Rodriguez, J., Shaw, S. E., & Corbel, S. 2006, A&A, 451, 1045

Sakurai, S. 2015, Phd thesis, University of Tokyo

Sakurai, S., Yamada, S., Torii, S., et al. 2012, PASJ, 64, 72

Sakurai, S., Torii, S., Noda, H., et al. 2014, PASJ, 66, 10

Schatz, H., Aprahamian, A., Barnard, V., et al. 2001, Physical Review Letters, 86, 3471

Serino, M., & Iwakiri, W. 2017, in 7 years of MAXI: monitoring X-ray Transients, held 5-7 December 2016 at RIKEN., ed. M. Serino, M. Shidatsu, W. Iwakiri, & T. Mihara, 129

Serino, M., Iwakiri, W., Tamagawa, T., et al. 2016, PASJ, 68, 95

Serlemitsos, P. J., Soong, Y., Chan, K.-W., et al. 2007, PASJ, 59, 9

Shakura, N. I., & Sunyaev, R. A. 1973, A&A, 24, 337

Strohmayer, T. E., Swank, J. H., & Zhang, W. 1999, Nuclear Physics B Proceedings Supplements, 69, 129

Strüder, L., Briel, U., Dennerl, K., et al. 2001, A&A, 365, L18

Sugizaki, M., Yamaoka, K., Matsuoka, M., et al. 2013, PASJ, 65, 58

Takahashi, T., Gunji, S., Hirayama, M., et al. 1993, IEEE Transactions on Nuclear Science, 40, 890

Takahashi, T., Abe, K., Endo, M., et al. 2007, PASJ, 59, 35

Tanaka, Y., Inoue, H., & Holt, S. S. 1994, PASJ, 46, L37

Tanaka, Y., Fujii, M., Inoue, H., et al. 1984, PASJ, 36, 641

Tarana, A., Bazzano, A., Ubertini, P., et al. 2006, A&A, 448, 335

Tauris, T. M., & van den Heuvel, E. P. J. 2006, Formation and evolution of compact stellar X-ray sources, ed. W. H. G. Lewin & M. van der Klis, 623–665

Thompson, A. C., Kirz, J., Attwood, D. T., et al. 2009, X-RAY DATA BOOKLET, Lawrence Berkeley National Laboratory University of California Berkeley, California 94720

Turner, M. J. L., Abbey, A., Arnaud, M., et al. 2001, A&A, 365, L27

Uchiyama, Y., Maeda, Y., Ebara, M., et al. 2008, PASJ, 60, S35

Šimon, V. 2002, A&A, 381, 151

Waki, I., Inoue, H., Koyama, K., et al. 1984, PASJ, 36, 819

Wallace, R. K., & Woosley, S. E. 1981, ApJS, 45, 389

White, N. E., & Peacock, A. 1988, MmSAI, 59, 7

Wilms, J., Allen, A., & McCray, R. 2000, ApJ, 542, 914

Xing, Y. M., Li, K. A., Zhang, Y. H., et al. 2018, Physics Letters B, 781, 358

Yamada, S., Uchiyama, H., Dotani, T., et al. 2012, PASJ, 64, 53

Zdziarski, A. A., Johnson, W. N., & Magdziarz, P. 1996, MNRAS, 283, 193

Acknowledgements

The present thesis was written as part of the doctor's course of the Department of Physics, Graduate School of Tokyo University of Science. I could not have completed this thesis without the support from my collaborators and laboratory members.

First of all, I would like to show my greatest appreciation to Prof. Toru Tamagawa who is my supervisor. I am very grateful for his guidance since I became a member of his labolarory. I would like to huge thanks for his trelance support.

I especially would like to express my deepest appreciation to Dr. Kazuo Makishima for his elaborated guidance and considerable encouragement that make my research of great achievement. Without his persistent support this thesis would not have been possible.

I would like to huge thank Dr. Liyi Gu who is an expert of the atomic physics for giving a helpful advice.

I would like to show my appreciation to Dr. Takao Kitaguchi who guided more strictly and kindly than anybody else since I was an under graduate school student.

I would like to thank all the member of Tamagawa High Energy Astro physics Labolatory at RIKEN for their valuable advice from different point of views. Particularly I appreciate to the student members, Ms. Sonoe Oda, Mr. Yuanhul Zhou, and Ms. Miho Okubo. I could spend greatest laboratory life with them.

Finally, this work was financially supported by Japan Society for the Promotion of Science through a Research Fellowship for Young Scientists.